

University of Louisville

ThinkIR: The University of Louisville's Institutional Repository

Electronic Theses and Dissertations

5-2017

Development and degradation analysis of novel micro and nanostructured transition metal oxide (TMO) anodes for aqueous sodium ion batteries.

Santanu Mukherjee
University of Louisville

Follow this and additional works at: <https://ir.library.louisville.edu/etd>



Part of the [Nanoscience and Nanotechnology Commons](#), and the [Other Materials Science and Engineering Commons](#)

Recommended Citation

Mukherjee, Santanu, "Development and degradation analysis of novel micro and nanostructured transition metal oxide (TMO) anodes for aqueous sodium ion batteries." (2017). *Electronic Theses and Dissertations*. Paper 2626.
<https://doi.org/10.18297/etd/2626>

This Doctoral Dissertation is brought to you for free and open access by ThinkIR: The University of Louisville's Institutional Repository. It has been accepted for inclusion in Electronic Theses and Dissertations by an authorized administrator of ThinkIR: The University of Louisville's Institutional Repository. This title appears here courtesy of the author, who has retained all other copyrights. For more information, please contact thinkir@louisville.edu.

DEVELOPMENT AND DEGRADATION ANALYSIS OF NOVEL MICRO AND
NANOSTRUCTURED TRANSITION METAL OXIDE (TMO) ANODES FOR
AQUEOUS SODIUM ION BATTERIES

By

Santanu Mukherjee

B.E., Bangalore Institute of Technology, India 2006

M.S., University of Nebraska-Lincoln, USA, 2012

A Dissertation

Submitted to the faculty of the

J. B. Speed School of Engineering of the University of Louisville

In Partial Fulfillment of the Requirements

For the Degree of

Doctor of Philosophy

In Mechanical Engineering

Department of Mechanical Engineering

University of Louisville

Louisville, Kentucky

May 2017

Copyright 2016 by Santanu Mukherjee

All rights reserved

DEVELOPMENT AND DEGRADATION ANALYSIS OF NOVEL MICRO AND
NANOSTRUCTURED TRANSITION METAL OXIDE (TMO) ANODES FOR
AQUEOUS SODIUM ION BATTERIES

By

Santanu Mukherjee

B.E., Bangalore Institute of Technology, India 2006

M.S., University of Nebraska-Lincoln, USA, 2012

A Dissertation Approved On

April 7, 2017

By the following Dissertation Committee:

Dr. Sam Park (Dissertation director)

Dr. Thomas Berfield (Committee member)

Dr. Ellen Brehob (Committee member)

Dr. Gamini Sumanasekera (Committee member)

DEDICATION

This thesis is dedicated to my parents

Late Mr. Swapan Mukherjee

And

Mrs. Ratna Mukherjee

I would not have been here today without their constant encouragement and sacrifices.

ACKNOWLEDGEMENTS

I would like to take this opportunity to thank my academic advisor, Dr. Sam Park, for his constant guidance, patience, encouragement and belief in my abilities. He had faith in me even when sometime I did not. I would also like to thank my committee members, Dr. Thomas Berfield, Dr. Ellen Brehob and Dr. Gamini Sumanasekera for their invaluable advice and numerous tips which have helped to greatly improve my dissertation. Mention must be made of the Conn Center which has provided extraordinary research facilities and highly talented staff members, especially Dr. Jacek Jasinski, Dr. Mahendra Sunkara, Dr. Bijandra Kumar and Dr. Arjun Thapa, to help me carry out my research. Dr. Julia Aebersold at the Micro and Nanotechnology center has been a very knowledgeable friend. The Louisville community in general and that of U of L in particular have been extraordinary hosts and have greatly facilitated my success during this five year journey. The entire faculty and staff of the Mechanical Engineering Department at U of L have been the best I could have ever asked for and I have the deepest regards and the highest respect for them. I have sincere gratitude to my parents and other family members who have pushed me forward continuously and have endured my long hours away from home. Lastly, I'd like to express deep appreciation for my colleagues, Nicholas Schuppert and Alex Bates, with whom I have shared the same lab for about 5 years, learnt a lot and have had many an interesting and enlightening discussion.

ABSTRACT

DEVELOPMENT AND DEGRADATION ANALYSIS OF NOVEL MICRO AND NANOSTRUCTURED TRANSITION METAL OXIDE (TMO) ANODES FOR AQUEOUS SODIUM ION BATTERIES

Santanu Mukherjee

April 7, 2017

One of the primary motivations driving battery technology research is the need to develop cleaner and more efficient energy storage systems. The portable electronics industry has developed exponentially, especially over the last couple of decades and therefore the importance of efficient electrochemical energy storage systems cannot be overstated. Li-ion batteries have been the predominant rechargeable energy in use, however, they have their own particular drawbacks viz. flammability of the electrolyte, expensive mining of the Li metal etc. This is where the importance of Na-ion batteries lie. This research focuses on using existing transition metal oxides (TMOs) and tuning their crystal structure as well as morphology for application as anodes in the Na-ion battery systems. The three TMOs used in this thesis are copper (II) oxide (CuO), iron (III) oxide (Fe₂O₃) and titanium (IV) oxide (TiO₂). They are chosen based on their easy availability, affordability and structural flexibility. Aqueous environment has been chosen as it tends to involve simpler and easier fabrication, lower overhead costs and reduce the complexities of glovebox based assembly techniques. Improvement of kinetics and understanding as well as improving structural stability have been the main goals of this

dissertation. The analysis is performed by a two-way approach. Multiple morphologies of CuO are used to study the effect of surface area and porosity on kinetics. Similarly, the effect of doping different types of atoms in the hematite (α -Fe₂O₃) structure is studied in detail and the influence it has on the electrochemical performance. Finally, both the techniques are coupled to study the effects on the TiO₂ anode system.

It is expected that this dissertation will provide a comprehensive framework for the degradation analysis of simple TMO anodes in aqueous Na-ion battery systems, something which will add significant intellectual merit to the burgeoning field of aqueous rechargeable batteries in general.

TABLE OF CONTENTS

DEDICATION	iii
ACKNOWLEDGEMENTS	iv
ABSTRACT	v
CHAPTER 1	1
1.1 Background	1
1.2 The concept of energy	1
1.3 A brief history of human energy production and consumption	2
1.4 Energy consumption and its economics	4
1.5 Current outlook of energy storage systems	5
CHAPTER 2	7
2.1 Rationale for electrochemical energy storage	7
2.2. Types of electrochemical energy storage devices	8
2.3 Rechargeable (secondary) battery; Components and working principles	11
2.3.1 Components	11
2.3.2. Working principles	12
CHAPTER 3	17
3.1 Current status of Li-ion batteries and their drawbacks	17
3.2 Background and rationale behind Na-ion battery research	19
3.3 Material Selection	22
3.3.1 Cathodes	22
3.3.2 Anode.....	24
3.4 Objectives and intellectual merits	26
3.5 Instrumentation.....	28
3.5.1 Structural and particle property characterization techniques and instruments .	28
3.5.2 Instruments for measuring electrochemical performance	34

CHAPTER 4	37
4.1 Background of CuO systems.....	37
4.2 Rationale and outline.....	40
4.3 Fabrication.....	40
4.3.1 Cathode.....	40
4.3.2 Anode.....	41
4.4. Structural characterization.....	42
4.4.1 Cathode.....	42
4.4.2 Anode.....	44
4.5 Cell assembly	48
4.6 Electrochemical analysis	49
4.6.1 Cell cycling and stability	49
4.6.2 C rate analysis.....	51
4.6.3 Impedance spectra	52
4.6.4 Post cycled XRD analysis of mechanism of electrode degradation	54
4.7 Conclusion.....	56
CHAPTER 5	57
5.1. Background of Fe ₂ O ₃ anodes.....	57
5.2. Project rationale and outline.....	59
5.3 Anode fabrication.....	60
5.4 Structural characterization.....	60
5.4.1 XRD spectra analysis.....	61
5.4.2 XPS analysis	65
5.4.3 Raman spectra analysis.....	68
5.4.4 SEM imaging.....	69
5.4.5 Particle size and BET analysis.....	72
5.5. Cell assembly	73
5.6. Electrochemical analysis	73
5.6.1 Cell cycling and stability	73
5.6.2. Capacity loss analysis.....	76
5.7 Post cycling analysis	77

5.7.1 XRD spectra analysis.....	77
5.7.2 Impedance analysis.....	79
5.7.3. Cyclic voltammetry analysis	80
5.8 Conclusion.....	81
CHAPTER 6	82
6.1 Background of TiO ₂ anode systems	82
6.2 Rationale and objectives.....	83
6.3 Materials.....	83
6.3.1. Anode.....	83
6.4. Structural Characterization.....	84
6.4.1. XRD.....	84
6.4.2. TEM analysis.....	85
6.4.3. SEM.....	86
6.4.4. Raman spectra.....	88
6.5 Cell assembly	89
6.6 Battery performance analysis	89
6.6.1 Cell cycling and stability analysis	89
6.7 Thermal imaging analysis:	92
6.8 Conclusion:.....	94
CHAPTER 7	95
REFERENCES	97
CURRICULUM VITAE	105

LIST OF FIGURES

FIGURE NUMBER AND DESCRIPTION	PAGE NUMBER
1. A schematic diagram illustrating the relationship between resources, labor, capital and energy produced.	4
2. Pie chart representation of the non-pumped hydro based energy storage systems currently used in the U.S.	6
3. Schematic representation of the different types of electrochemical storage devices.	11
4. Schematic representation of intercalation in a hypothetical Na-ion battery.	13
5. Scanning electron microscopy (SEM) images of (a) pristine electrode (b) electrode after 2 cycles of operation and (c) same electrode after 5 cycles of operation.	19
6. Representative charge-discharge curves for the 1 st , 2 nd and 10 th cycle of Na ₃ V ₂ (PO ₄) ₃ cathode.	21
7. Schematic representation of the structure of a typical Prussian blue crystal.	23
8. Schematic ball and stick representation of (a) tetragonal CrO ₂ (b) simple cubic CoO and (c) orthorhombic V ₂ O ₅ .	25
9. Bruker D8 TM diffractometer for performing XRD of crystalline samples	29
10. InVia Renishaw TM Raman microscope for performing Raman spectra analysis	30
11. (a) TESCAN TM SEM and (b) FEI Nova NanoSEM TM 600	31
12. G2 F30 TECNAI TM TEM used for imaging and analysis purposes	32
13. Thermo VG MultiLab XPS system for surface characterization	33
14. (a) Brookhaven TM Particle size analyzer and (b) Micrometrics Tristar TM Surface Area and Porosity Analyzer	34
15. Arbin BT2043 TM instrument used for galvanostatic cell cycling	35
16. Biologic SP-200 TM potentiostat for CV and impedance spectra measurements	36
17. (a) XRD spectra of P.B. sample (b) Characteristic Raman spectra of the P.B. sample (c) SEM images of the characteristic P.B. cubes and (d) particle size distribution of the P.B. samples.	44

18. (a) Representation of the full spectrum XRD data with the important peaks labeled and impurity peaks starred and (b) is the (002) peak in greater detail.	45
19. SEM images of (a) CuO as obtained sample (b) CuO ribbons (c) CuO platelets and (d) CuO spheres.	46
20. (a) Trend of BET (in black, left y-axis) and particle size (in blue, right y-axis) for the different CuO samples. (b) Representative BET adsorption-desorption curve of the CuO_platelets sample.	47
21. (a) Illustrates the first cycle discharge capacities of the different CuO microstructures and (b) represents the stability plots of the different CuO anodes.	49
22. C Rate analysis of the various CuO samples.	51
23. (a) Impedance spectra of the CuO_as obtained samples for the pristine, 50 th and 100 th cycle of operation. (b) Impedance spectra of the CuO_spheres for the pristine, 50 th and 100 th cycles.	52
24. Comparative impedance spectra of pristine and post cycled CuO_spheres and CuO_platelets.	54
25. Comparative post cycled XRD spectra of (a) CuO platelet and (b) sphere samples	55
26. XRD spectra stack of pure Fe ₂ O ₃ along with all the Zn doped samples (a) demonstrates the entire spectra and (b) a more detailed look at the (024) peak	61
27. XRD spectra stack of pure Fe ₂ O ₃ along with all the Al doped samples (a) demonstrates the entire spectra and (b) a more detailed look at the (024) peak.	63
28. “Full survey” XPS of the Fe ₂ O ₃ (in green), Fe _{1.92} Al _{0.08} O ₃ (in blue) and Fe _{1.92} Zn _{0.08} O ₃ (in red).	66
29. (a), (b), (c) and (d) represent the individual XPS peaks demonstrating the Zn, O, Fe and Al characteristic peaks.	67
30. Raman spectra stack of pure Fe ₂ O ₃ along with all the Zn and Al doped samples. (a) demonstrates the Raman spectra of Fe _{2-x} Zn _x O ₃ samples and (b) Raman spectra of the Fe _{2-x} Zn _x O ₃ samples.	68
31. SEM images of pure Fe ₂ O ₃ sample at (a) 5 μm and (b) 2μm resolution.	69
32. SEM images of (a) Fe _{1.98} Zn _{0.02} O ₃ (b) Fe _{1.96} Zn _{0.04} O ₃ (c) Fe _{1.92} Zn _{0.08} O ₃ and (d) Fe _{1.88} Zn _{0.12} O ₃ samples.	70
33. SEM images of (a) Fe _{1.98} Al _{0.02} O ₃ (b) Fe _{1.96} Al _{0.04} O ₃ (c) Fe _{1.92} Al _{0.08} O ₃ and (d) Fe _{1.88} Al _{0.12} O ₃ samples.	71
34. (a) BET surface area trends of the Zn and Al doped samples. (b) Average	72

particle size trends of the Zn and Al doped samples.	
35. (a) Representation of the first cycle discharge curves for the Fe_2O_3 (in red), $\text{Fe}_{1.96}\text{Zn}_{0.04}\text{O}_3$ (in orange) and $\text{Fe}_{1.88}\text{Zn}_{0.12}\text{O}_3$ (in blue) samples and (b) are the specific capacity retention plots of all the Zn doped samples.	74
36. (a) Representation of the first cycle discharge curves for the Fe_2O_3 (in red), $\text{Fe}_{1.96}\text{Al}_{0.04}\text{O}_3$ (in orange) and $\text{Fe}_{1.88}\text{Al}_{0.12}\text{O}_3$ (in blue) samples and (b) are the specific capacity retention plots of all the Al doped samples.	75
37. Indicating the capacity loss trend in greater detail for the (a) non-doped and the 8 % and 12 % Al doped samples respectively and (b) for the non-doped and the 8 % and 12 % Zn doped samples respectively.	76
38. Post cycled XRD comparison of the (012) peak for the (a) 12 % Zn doped sample and (b) 12 % Al doped sample.	78
39. Pristine and post cycled impedance spectra analysis for the non-doped and 12 % Al and Zn doped samples respectively.	79
40. CV analysis of (a) pristine and post cycled 12 % Zn doped sample and (b) pristine and post cycled 12 % Al doped sample respectively.	80
41. (a) XRD spectra of the pristine TiO_2 , TiO_2 -HT and $\text{Na}_2\text{Ti}_3\text{O}_7$. (b) XRD spectra of pristine and TiO_2 -HT.	84
42. (a) TEM image of $\text{Na}_2\text{Ti}_3\text{O}_7$ at 0.5 μm resolution showing rod like morphology (b) HRTEM image taken at 5 nm (c) SAED pattern demonstrating characteristic d-spacing values for the (110) and (001) (d) similar SAED pattern exhibiting the d-spacing values for the (013) and (101) planes	86
43. (a) is the images of the amorphous TiO_2 system (b) pristine TiO_2 (c) TiO_2 -HT (d) $\text{Na}_2\text{Ti}_3\text{O}_7$	87
44. (a) Raman spectra of the different anode systems (b) Raman spectra peaks in greater detail to show peak broadening and shift.	88
45. 1 st and 20 th cycle discharge capacities for (a) amorphous TiO_2 sample (b) pristine TiO_2 sample (c) TiO_2 -HT sample and (d) $\text{Na}_2\text{Ti}_3\text{O}_7$ sample in aq. Media	90
46. Charge (dashed line) and discharge (solid line) capacities of the 1 st and 100 th cycle for (a) TiO_2 sample and (b) $\text{Na}_2\text{Ti}_3\text{O}_7$ sample in organic media.	91
47. Stability analysis of the various anode systems in aqueous media.	92
48. Figures (a) and (b) represent the thermal images profiles for the TiO_2 anodes and P.B. cathode during the cell cycling. Similarly (c) and (d) are the thermal image profiles for the $\text{Na}_2\text{Ti}_3\text{O}_7$ anode and the P.B. cathodes during cycling.	93

LIST OF TABLES

TABLE	PAGE NUMBER
1. Comparative analysis of Na and Li systems	20
2. Comparison of lattice parameters of the $\text{Fe}_{2-x}\text{Zn}_x\text{O}_3$ systems and of the ZnFe_2O_4 spinel structure	62
3. Comparison of lattice parameters of the $\text{Fe}_{2-x}\text{Al}_x\text{O}_3$ systems	65

CHAPTER 1

A BRIEF INTRODUCTION TO ENERGY SYSTEMS: BASIC ASPECTS, HISTORY, ECONOMICS & CURRENT OUTLOOK

1.1 Background

Efficient, environmentally sustainable and economically prudent energy consumption and storage is one of the primary technological challenges of the 21st century. With growing awareness about climate change caused by fossil fuel usage, the current global trend has been to transition away from these “unclean” energy sources to potentially “cleaner” and “smarter” energy sources as well as grid storage techniques^{1,2}. The next sections in this chapter will try to provide a perspective about the scientific concept of energy itself, as well as historical and socio-economic aspects of energy generation, storage, and consumption.

1.2 The concept of energy

Energy is often conceived of and even studied as a mathematical construct; a value that can be obtained by solving a set of equations³. However energy can be considered to be something more fundamental, a necessary driving force behind almost all chemical transformations and physical phenomena³. One of the most salient facts about energy is its ubiquity and yet it is “invisible”; unlike matter which is tangible and visible in daily life^{3,4}. It was postulated by Mayer as early as 1842 that energy exists in different forms and that work and heat, something hitherto thought to be mutually exclusive, were in fact related⁵. Since then extensive research has shown that energy, as a physical quantity, is

considered to be “*a property of matter that can be converted into work, heat or radiation*”⁶.

Therefore, energy, even though not a tangible entity, plays an immensely important role in the environment. It is unique in that it can “flow” between systems and it is interconvertible with matter⁶. The different types of energy that are commonly encountered are solar, nuclear, gravitational, chemical, sound and electrical⁷. The net amount of energy that the universe holds is essentially a constant and it is the transformations of energy between its various forms that evokes interest and is studied and researched extensively^{7,8}.

1.3 A brief history of human energy production and consumption

Energy has been one of the most common and necessary requirements of human civilization from its infancy. It is easily considered to be the fundamental driving force behind human progress and development. Even though the need and utilization of natural resources for energy purposes have been prevalent since antiquity, the concept of “energy” was first put forward by the Greek philosopher Aristotle⁶. The sun has served as a continuous and perennial source of energy for the earth and its inhabitants, even before any energy storage system was invented. In fact life on earth as we know it would probably not have existed without the sun’s presence. It has been estimated that the total energy received is about $1366 \text{ Wm}^{-2}\text{s}^{-1}$ ⁶. This tremendous amount of energy drives photosynthesis and is utilized by other living beings in their vital metabolic pathways as well as applied in other secondary human technological applications e.g. solar heating systems. One of the earliest instances of utilization of natural resources for energy consumption was the discovery of fire and consequently the burning of wood for cooking

and heating; the first evidence of the controlled usage of fire being around 50,000 years ago⁹. The next watershed moment in human civilization's energy consumption was the development of agriculture¹⁰. The conquest of wind and water for energy production was another important event in this saga. Considerable growth of the human population and improvement in quality of life continued, even though there were no further dramatic enhancements in energy storage or consumption techniques¹¹.

One of the most dramatic and consequential events in human civilization and development was the Industrial Revolution, which as the name suggests, "revolutionized" the way energy was produced and consumed¹². Starting in Britain in the mid-18th century, it spread throughout the world at a rapid pace^{12,13}. It was also a period of almost unparalleled growth in economic activity and prosperity and during which the dominance of fossil fuels started to become prevalent¹³. The period marked an exponential rise in industries, especially manufacturing and coal, which became the predominant energy source¹⁴. With the development of the internal combustion engine that spurred on growth, the usage of oil started to take a prominent role. The mid-20th century denotes the time where oil became the primary energy producing source in the US¹⁵. The period after WWII also witnessed the growing emergence of nuclear power¹⁶. However, global oil shocks of the 70s (especially the 1973 oil crisis) led to growth of natural gas as an energy source¹⁷. It is only since the 1980s that the application of renewable energy sources has slowly come into the mainstream with the development of technology for the utilization of biomass, wind, solar, etc¹⁸. These trends demonstrate that technological innovation has almost always led to diversification of energy producing sources, resulting in an effort

towards overcoming the energy production and consumption drawbacks of the previous era.

1.4 Energy consumption and its economics

The economics of any system always plays a vital role in determining its feasibility. Energy is manifested in practice as “useful work” and the utilization of productive human labor is absolutely essential in performing this work¹⁹. The flowchart in the figure below illustrates how the different components in the entire system are related.

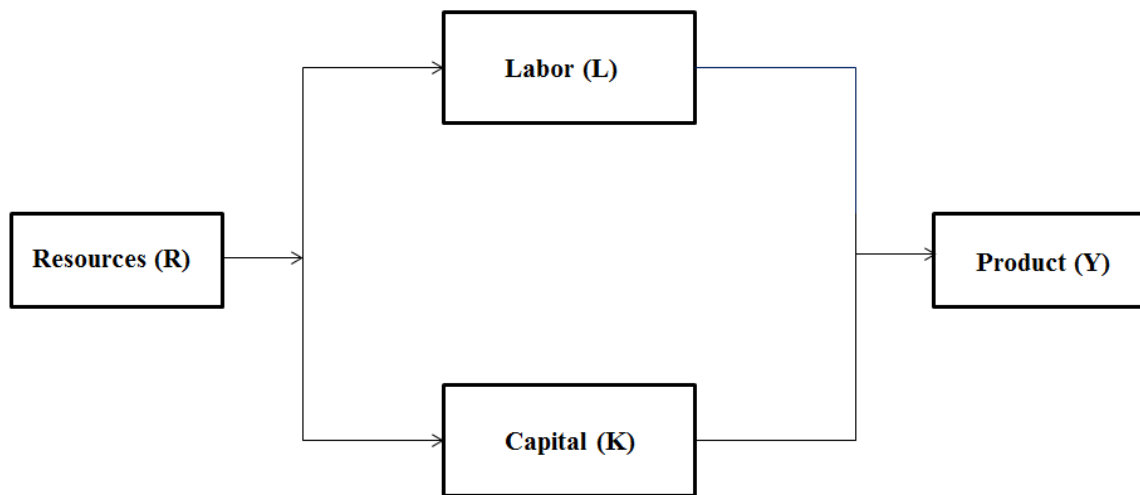


Figure 1. A schematic diagram illustrating the relationship between resources, labor, capital and energy produced (product)¹⁹.

The cost of energy generation and its effect on the labor market is an important consideration because that plays an important role in developing public policy for energy issues^{19,20}. Greater deregulation of energy markets, especially in Europe, has played an important role in influencing energy costs²⁰. According to current estimates, the net global energy consumption annually is about 12.3 trillion Watts and is expected to be 17 trillion Watts by 2030^{19,21}. It is interesting to note that, even with the current focus on

energy generation from renewable sources, approximately 80 % of the estimated energy consumption was from traditional or fossil fuel sources (mainly coal, oil and natural gas). It has also been forecast by the Energy Information Administration (EIA) that global energy consumption is to grow by about 50 % by the end of the current century^{20,22}. It is here that renewable energy systems play a central role. As an example, the current levelized energy generation cost from coal fired power plants in the OECD countries range between \$54/MWh in Australia to \$120/MWh in the Slovak Republic²². According to estimates, the net investment cost represents 28 % of the expenditure, whereas the carbon capture technology accounts for approximately 30 % of the cost^{21,22}. Currently about 9 % of energy consumption comes from renewable sources (i.e. hydroelectric, solar, wind, biofuel, etc.) and these numbers have remained steady for some time²²⁻²⁴. It should be noted that the infrastructure needed to generate energy from renewable techniques is still in its nascent stage in various parts of the world and, as such, is expensive. Therefore it is imperative that good energy and grid storage systems are developed to offset the heightened cost that might accompany energy generated from renewable systems.

1.5 Current outlook of energy storage systems

Energy storage systems have an important role to play with the development of new, varied and technologically advanced energy production systems, especially from renewable sources. Economic arguments also play a leading role in using grid storage systems vis-à-vis more conventional systems of load distribution²⁵. A modern energy storage system can serve several important purposes: reduce the need for major and expensive system updates, play a role in emergency preparedness and assist in integrating the transportation sector as and when it gets fully electrified²⁵. According to the latest

DOE reports, the net storage capacity of all the storage systems in the US amount to approximately 24.6 GW^{25,26}. The storage systems in use currently comprise of pumped hydro, flywheels and electrochemical systems (different types of batteries). It should be noted that out of these pumped hydro alone account for about 95 % of the total^{25,26}. The figure below illustrates the percentage breakdown of the non-pumped hydro based (5 %) energy storage systems.

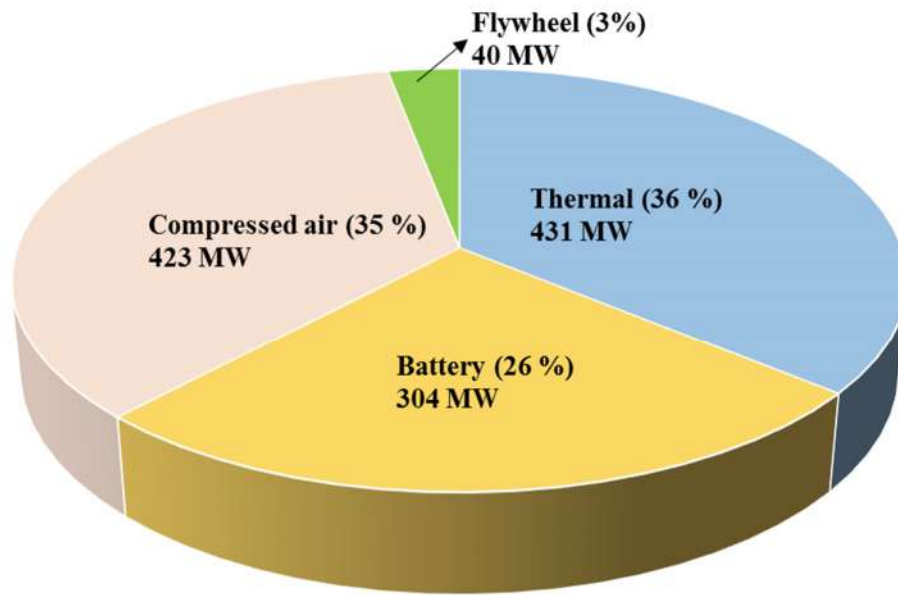


Figure 2. Non-pumped hydro based energy storage systems currently used in the U.S.²⁵.

These facts underscore the importance of robust, flexible and diverse grid storage systems so that over-reliance on any particular type can be avoided. It is believed that electrochemical energy storage systems will play a pivotal role in the near future.

CHAPTER 2

ELECTROCHEMICAL ENERGY STORAGE AND BATTERIES

2.1 Rationale for electrochemical energy storage

Electricity is the most important form of energy in today's world and about 20 TW of electrical energy is generated globally^{27,28}. It has been forecast that this global demand for power will only increase and be tripled by the end of the 21st century^{27,28}. However, as mentioned in the previous chapter, most of the energy produced currently is from fossil fuels which have extensive environmental hazards. Reports indicate that approximately 1 kg of CO₂ is emitted for every kilowatt-hour (kWh) of electricity produced from coal^{27,29,30}. It is here that renewable energy sources are supposed to play a key role; however, they also have their respective pitfalls. Wind energy and solar power are both intermittent and dependent on location and geography; as a result, they do not fare well when persistent peak demands need to be satisfied²⁷.

An ideal energy storage system should essentially share some attributes of the generation system its coupled with and provide economic benefits and environmental advantages. Some of the important aspects of a robust electrochemical energy storage system is a low carbon (greenhouse) footprint, good efficiency, operational longevity, large capacity, and small size, all with a reasonable budget²⁷. Existing energy storage systems, like pumped hydro, have their own drawbacks; e.g. its performance goes down in a region where there's lack of water²⁴. The compressed air energy storage (CAES) system, as the name

suggests, uses compressed air to store power; however, its usage is primarily for off-peak energy storage and there are some concerns of NO_x emissions^{24,31}.

Electrochemical energy storage systems have elicited great interest in recent years with the motivation of overcoming some of the above-mentioned drawbacks³². Batteries are the most commonly used types of electrochemical storage devices; fuel cells, flow batteries, supercapacitors, etc. being other types of electrochemical energy storage^{27,33,34}. Some of the advantages provided by an electrochemical energy storage system include a smooth and seamless integration into the grids of the future (“smart grids”), smoothing out renewable energy generation wherever it is unreliable, provide energy during emergency demands, provide longevity, be able to perform at high as well as low temperatures, and help broadly in load balancing^{27,35}. Nevertheless, economics is always an important driving factor behind any new technology and the expenditure behind the establishment of electrochemical energy storage devices still need to be solved³⁶.

2.2. Types of electrochemical energy storage devices

Electrochemical energy storage devices are attracting widespread research and attention because of their inherent advantages, some of which have been mentioned in the preceding sections. The different types of electrochemical storage devices can be broadly classified as fuel cells, flow batteries, (super) capacitors and batteries^{24,37}. All of these have a common feature in that they provide electrical energy when the need arises, from the chemical energy which they store³⁷.

Fuel cells may have a continuous supply of fuel from external sources; including a continuous oxidant (atmospheric air) supply^{24,38}. There is no direct combustion, rather hydrogen oxidizes electrochemically to produce the energy required. Fuel cells vary in

the amount of energy they produce and operational temperatures³⁸. Due to the type of reaction occurring, water management is a significant concern in fuel cell technology currently³⁸.

Supercapacitors store energy in the form of electrical charge and have very high efficiencies ($\approx 100\%$); but, usually suffer from low energy density²⁷. A preferentially permeable (to the ions) membrane saturated with electrolyte segregates two different electrodes in a compartment. Power is provided in response to an external potential. Supercapacitors have been incorporated in grid power applications^{24,27,39}.

Batteries are very similar in design to supercapacitors and work along the same principles. They also have the advantage of being relatively lightweight and portable, have high operational longevities, and generally good storage efficiencies. The two electrodes of the battery are called the anode and the cathode^{37,40}. Different types of battery technologies are in application today; primary and secondary batteries are a broad and useful classification. Primary batteries are non-rechargeable and have to be disposed of once they are depleted⁴⁰. However, they cheaply provide high energy density. Some of the commonly used primary batteries are silver oxide, lithium, zinc-air, and alkaline^{24,41}. Sometimes they do not contain a liquid electrolyte and are therefore called “dry cells”⁴¹. On the other hand secondary batteries (or “cells” as they are interchangeably called) are those that can be recharged once they have been depleted²⁴. Recharging is usually achieved by applying a potential in the opposite direction to that when the battery is being discharged or “used”. Based on the specific power and energy, batteries are usually placed somewhere between supercapacitors and fuel cells⁴². Examples of secondary batteries include the widely used lead acid (Pb acid), nickel cadmium (Ni-Cd),

nickel-metal hydride (Ni-MH), lithium ion (Li-ion), and sodium ion (Na-ion) batteries^{24,43}. Significant improvement in rechargeable battery technology has been achieved; however, a lot of work still lies ahead with regards to optimizing cell chemistries to obtain maximum energy output while keeping cost constraints in mind⁴².

Flow batteries are another type of electrochemical storage device which store two distinct electrolytes (or “catholytes” and “anolytes” as they are called) in separate reservoirs³⁷. Each electrolyte contains a redox couple (hence they are sometimes called “redox” flow batteries) and these local reactions produce the electrical energy⁴⁴. Vanadium-vanadium and zinc-bromine are some redox couples used. Flow batteries typically have energy densities on the lower side ($\approx 40 \text{ Wh kg}^{-1}$); however, their longevity (approximately 25-35 years) is an advantage³⁷.

A simple schematic diagram of the different types of electrochemical energy storage devices is given in the figure below:

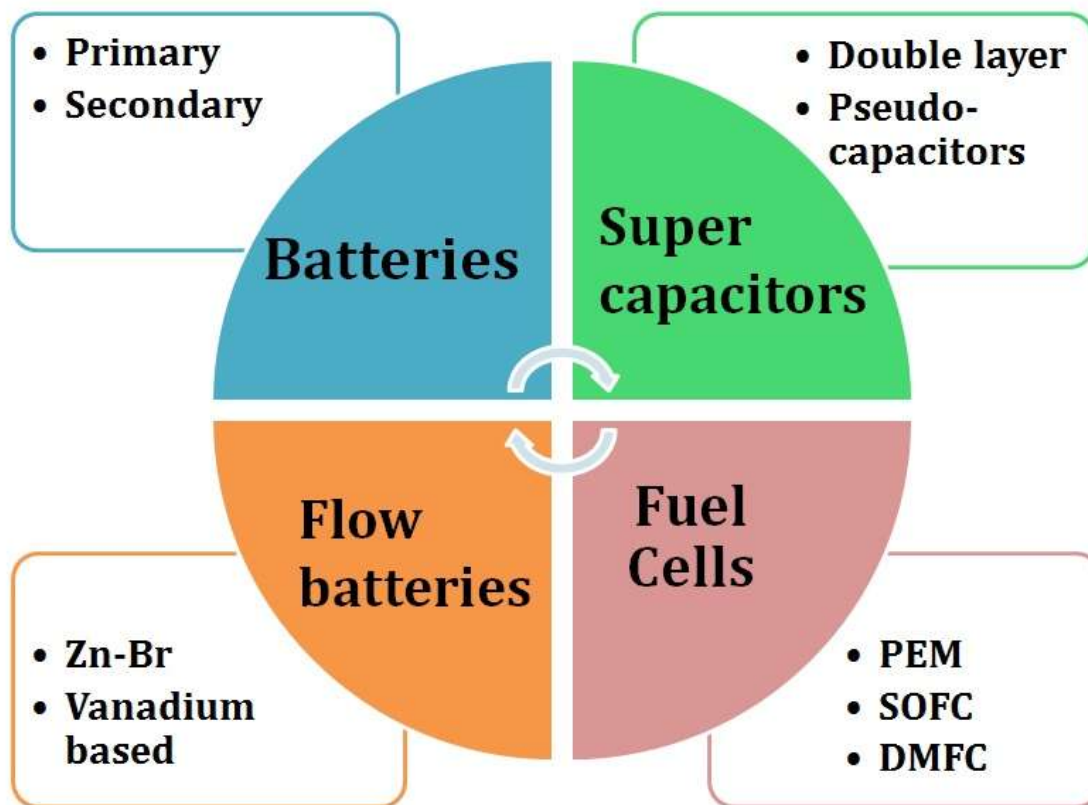


Figure 3. Schematic of the different types of electrochemical storage devices.

2.3 Rechargeable (secondary) battery; Components and working principles

As mentioned above, secondary batteries usually comprise two different electrodes, a membrane which allows the ion of interest to be transported through it, and an electrolyte housed together in an enclosed casing. These aspects will be discussed in greater detail in the following sections:

2.3.1 Components

The most important components of a rechargeable battery are its electrodes (the anode and the cathode), the electrolyte, and the preferentially permeable membrane that allows the ions to go through. Usual conventions designate the cathode and the anode as the positive and negative electrodes, respectively^{41,45}. Oxidation, i.e. loss of electrons, takes

place at the anode and reduction, i.e. a gain of electrons, occurs at the cathode during the discharging process; this is reversed during charging^{41,45}. This back and forth motion of the electrons across the external circuit is complemented by ionic movement through the membrane which maintains the overall electrical neutrality of the cell.

2.3.2. Working principles

As has been described in the preceding section, a rechargeable battery essentially has the ions shuttling between the electrodes through the electrolyte. For example, during the discharging process in a Na-ion battery, the Na⁺ ions move from the Na metal anode to the cathode. During this process, the ions traverse through the electrolyte and the flow of ions through the liquid electrolyte is usually modeled using Fick's second law of diffusion⁴⁶. Fick's second law of diffusion can be written as follows:

$$\frac{\partial c}{\partial t} = -D \cdot \frac{\partial \varphi}{\partial x} = \frac{D \partial^2 c}{\partial x^2} - \frac{F}{RT} \cdot D \left(\frac{\partial E}{\partial x} \right) \quad (1)$$

where D is the diffusion coefficient, T is the temperature, R is the gas constant and F is Faraday's constant. One of the primary assumptions in this process is to consider that concentration gradient is the main driving force behind the ionic movement and migration terms can be neglected⁴⁶. Subsequently, the Na⁺ ions are hosted by the cathode lattice through a process called *intercalation*⁴⁷. Therefore, sometimes these batteries are called "rocking chair" batteries because of this back and forth ionic motion^{47,48}. Consequently, from a *structural perspective*, crystallography and crystal geometry are important deciding factors that help to accommodate migrating ions in the host lattice. Therefore, the host electrodes must be chosen so that their crystal structures are amenable to hosting the intercalated ions. Figure 4, below, shows a schematic diagram of the intercalation process during the charging and discharging of a hypothetical Na-ion battery.

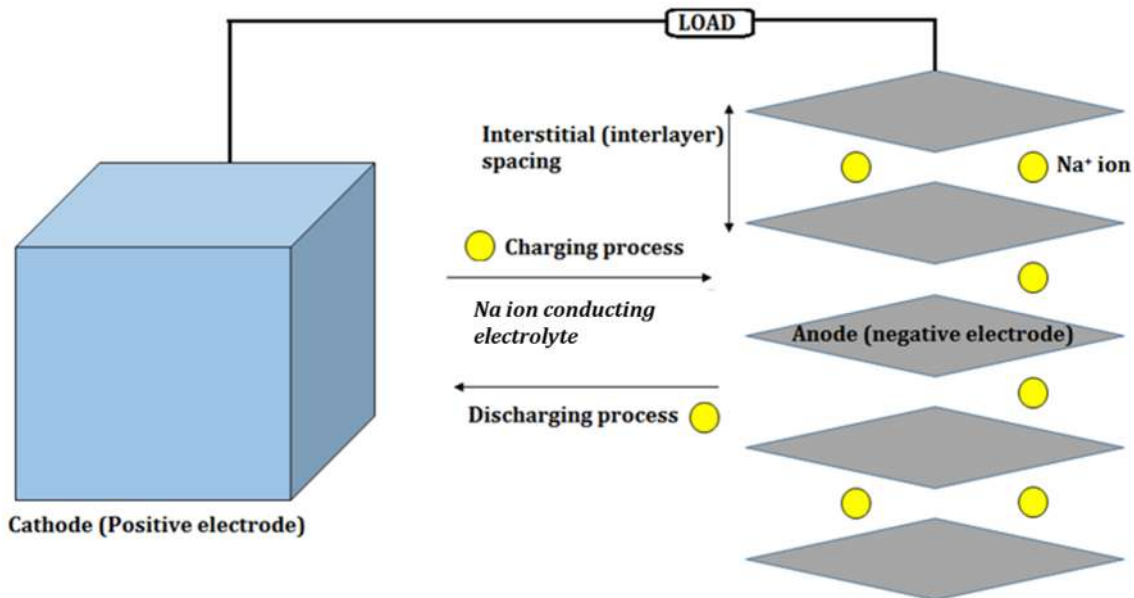


Figure 4. Schematic of intercalation in a hypothetical Na-ion battery.

The figure demonstrates the ions (in solid yellow) shuttling back and forth across the electrolyte between the cathode and the anode. The charging process consists of the ionic movement from the cathode to the anode and vice versa during the discharging process. As the ions move through the electrolyte, the electrons flow in the opposite direction through the external circuit to maintain the charge neutrality.

Thermodynamics is another important factor that acts as the prime mover for successful electrochemical reaction. A reversible electrochemical reaction is guided by the thermodynamic relation as given in equation (2) below

$$\Delta G = \Delta H - T\Delta S \quad (2)$$

where ΔG is the change in free energy, T is the temperature, ΔS is the change in entropy, and ΔH is the change in enthalpy⁴⁹. The net free energy change is important because its sign is an indicator of the thermodynamic possibility of a reaction. The free energy

change is also considered equivalent to the molar free energy of the reaction, which is equated to the electrical work obtained, and this is then demonstrated by equation (3) as given below^{38,49}.

$$\Delta G = -nFE \quad (3)$$

where n is the number of moles of ions or electrons being transported, F is Faraday's constant, and E is the cell voltage^{38,48}. Therefore, ΔG in this case estimates the total electrical work output that can be obtained from the cell^{38,49}. A fundamental thermodynamic relation can be written as follows^{38,50}.

$$\Delta G = \Delta G^\circ + RT \ln Q \quad (4)$$

where ΔG° is the standard free energy change, R is the universal gas constant, and Q is the reaction quotient^{38,49}. Considering equation (3), equation (4) can be rewritten as follows^{49,50}.

$$-nFE = -nFE^\circ + RT \ln Q \quad (5)$$

This reaction when simplified comes down to the one as shown below:

$$E = E^\circ - \left(\frac{RT}{nF}\right) \ln Q \quad (6)$$

Equation (5) is the basic form of the celebrated Nernst equation and it relates the half-cell potential E to the reaction conditions (temperature and activity of the reactants)^{49,51}. Therefore, it is seen that thermodynamics not only assumes an important role in being the force behind electrochemical reactions, it is also a major factor that determines cell potential and net energy output.

Favorable crystal geometry and the electrochemical reaction proceeding in the forward direction are two of the most vital aspects of the rechargeable battery for its successful functioning. Slow reaction rates, i.e. sluggish kinetics, are detrimental to developing a

successful battery and therefore understanding the reaction kinetics is essential. It is understood that electrochemical reactions mostly take place at the electrode-electrolyte interface⁵². Consequently, when the ion (e.g. Li^+ , Na^+) transits from the electrolyte to the electrode, it encounters an energy barrier at the interface^{51,52}. This energy barrier, or rather its “height” determines the reaction rate. The steeper the energy barrier, i.e. the greater the energy that has to be expended to overcome it, the slower the reaction rate will be, rendering the battery inefficient⁵¹. Considering an equilibrium condition, the current produced at an electrode is given by equation (7)

$$i = n F j \quad (7)$$

where i is the localized electrode current, n is the number of moles of electron transported, F is faraday’s constant and j is the current density^{48,50}. The localized electrode current results in local potential deviating from equilibrium. This discrepancy between the theoretical electrode potential and what it actually is, is designated as “overpotential”^{38,49}. For all practical purposes, the overpotential at an electrode can be mathematically represented as follows:

$$\eta = \Phi - \Phi^0 \quad (8)$$

where η denotes the overpotential, Φ denotes the potential due to local current i , and Φ^0 is the equilibrium electrode potential. When the electrochemical reaction takes place at the interface, the metal ions that have been transported through the electrolyte lose their positive charge and tend to recombine with an electron in order to maintain the overall electrical neutrality of the electrode, according to chemical reaction given in equation (9)⁴⁹.



If the above reaction is in equilibrium, then the forward as well as the backward reaction take place at the same rate. However, such an ideal scenario is seldom the case and usually one proceeds over the other. If the forward reaction takes place at a higher rate, the electrode is stripped of electrons and acquires a positive charge localized at the interface^{49,51}. This localized positive charge region subsequently attracts negatively charged ions to its vicinity and therefore a “double layer” of charge is built up^{49,53,54}. This localized charge buildup causes what is known as “polarization,” resulting in the electrode having a different potential than its equilibrium value⁵³. Previous experimental results have indicated that the electrical double layer (EDL) is usually about 1 nm thick and produces a large electric field of approximately 10^9 V m^{-1} in the neighborhood^{49,51}. Therefore, it can be seen that the performance of a cell depends on several electrochemical factors and the choice of the electrode materials and battery design has to be done judiciously so as to obtain optimum results.

CHAPTER 3

SODIUM ION BATTERIES: BACKGROUND, RATIONALE, MATERIALS SELECTION, INTELLECTUAL MERITS AND INSTRUMENTATION

3.1 Current status of Li-ion batteries and their drawbacks

The need for “clean” energy systems and sustainable grid storage is the driving force behind the development of novel rechargeable battery systems. Primary lithium batteries came into being in the 1970s and Li-ion and have exploded on to the scene since then⁵⁵. The first commercial rechargeable Li-ion battery was introduced by Sony in 1991^{43,48}. Currently, Li-ion batteries are the pre-eminent rechargeable energy storage devices in use. They provide several advantages; considerable energy densities (usually in the range of 100 Wh kg⁻¹ – 150 Wh kg⁻¹) high operating voltages (≈ 3.5 V)⁵⁶. Especially in the field of portable electronics e.g. laptops and mobile phones, Li-ion battery systems have found remarkable success⁵⁶. A basic Li-ion rechargeable battery essentially contains a graphite anode a LiCoO₂ (LCO) cathode and a Li⁺ ion conducting electrolyte e.g. LiPF₆⁵⁶. Both these electrode materials are layered and allows for the rather smooth Li⁺ intercalation/deintercalation. The reversible charging process involves the oxidation of the LCO cathode and the consequent lithiation of the graphite according to the following reaction⁵⁶:



Because of the nature of the reaction i.e. half a Li ion being stripped from the LCO cathode, only about half of the theoretical specific capacity of approximately 140 mAhg^{-1} is obtained^{57,58}.

Beyond this most fundamental arrangement, extensive research has been done to develop newer and more advanced Li-ion battery materials. Lithium titanium oxides (LTO) materials viz. $\text{Li}_4\text{Ti}_5\text{O}_{12}$ have been developed with the aim of being a zero strain material and has provided specific capacities of 150 mAhg^{-1} – 160 mAhg^{-1} at a voltage of 1.5 V vs Li⁵⁹. Olivines are another class of cathode materials having the general formula LiMPO_4 (where M is a transition metal) and they provide relative flat intercalation and stable discharges⁶⁰.

However, Li ion batteries also suffer from several drawbacks. Flammability, leakage and electrolytic stability of the toxic electrolyte, is a major issue^{56,61}. The high reactivity of Li metal results in the formation of dendrites which sometimes short the cell and this is a safety feature that needs to be taken care of, and increases the manufacturing cost⁶¹. Steady degradation of the electrode due to continuous insertion/deinsertion of the Li^+ ion is another important area of concern⁵⁶. The figure below demonstrates the progressive lattice degradation of the cathode material.

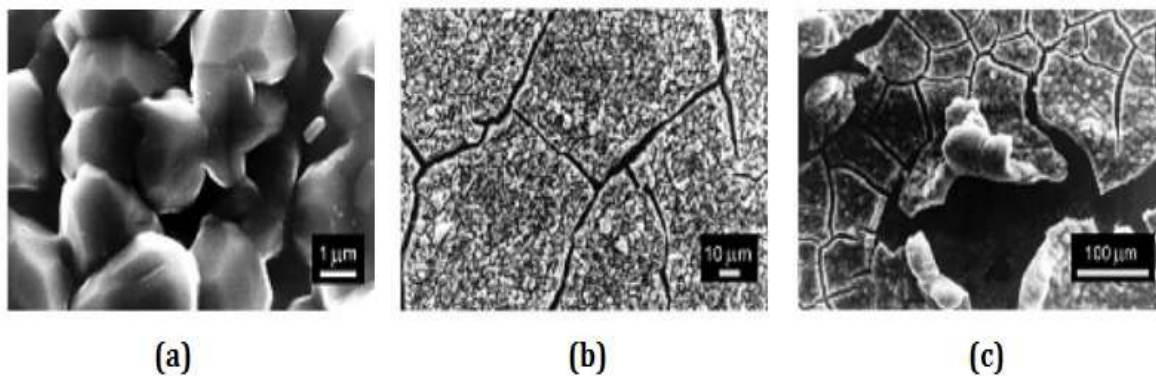


Figure 5. Scanning electron microscopy (SEM) images of (a) pristine electrode (b) electrode after 2 cycles of operation and (c) same electrode after 5 cycles of operation⁶².

As can be seen from the Figure 5, cracks start to appear in the material after just 2 cycles of operation and greatly magnify after 5 cycles. The volumetric expansion suffered by the electrode to accommodate the Li^+ ion is the reason behind this structural failure⁶². Apart from these drawbacks, economics and geopolitics also play a very important role. Li and its ores are expensive to mine and are found in parts of the world that do not have stable governance⁶³. Therefore it is imperative that alternative systems of rechargeable energy storage be studied and developed if the problems of Li-ion battery systems are to be overcome in particular and energy independence is to be achieved in general.

3.2 Background and rationale behind Na-ion battery research

The above-mentioned drawbacks of Li-ion systems provide an opening for other battery types viz. the Na-ion batteries. They are expected to play an important niche role in the rechargeable energy storage ecosystem. Metallic sodium has the advantage of being easily available in the earth's crust (ranked fourth in terms of the most abundant minerals in the earth) and subsequently, being rather cheap compared to lithium⁶⁴. Initially Li-ion

battery materials were used as templates for sodium ion battery study, this is because the principle of Li-ion and Na-ion batteries are analogous i.e. intercalation and hosting the Na⁺ ion in the host lattice. However it is this very principle that produces unique constraints for the Na-ion battery. The size of the Na⁺ ion is about 1.4 times larger than the Li⁺ ion and this requires rather larger interstitial/interlayer host spaces, and the host electrode also is prone to suffering more degradation to accommodate the continuous insertion/deinsertion of this large cation⁶⁵. A table of comparison between sodium and lithium-ion systems is provided below:

Table 1

Comparative analysis of Na and Li systems^{66,67}

	Na	Li
<i>Cation radius</i>	97 pm	68 pm
<i>E⁰ vs SHE</i>	-2.7 V	-3.04 V
<i>Abundance</i>	23.6*10 ³ mg kg ⁻¹	20 mg kg ⁻¹
<i>Price of carbonates</i>	\$ 0.29 per kg	\$ 5.82 per kg

The Na/S and the Na/NiCl₂ based systems were one of the earliest Na-ion battery systems that were studied, during the 1970s and the 1980s⁶⁴. These systems had low power densities, moderate energy densities and operated at rather high temperatures (300 °C – 350 °C)⁶⁴. Research in Na-ion systems has diversified much since then and the primary motivation of Na-ion battery research has been to engineer materials to allow for easy intercalation of Na ions into the electrodes. One of the earliest developments in this field

was work done by Whittingham and Hagenmuller on layered compounds such as dichalcogenides like MoS_2 , TaS_2 and oxides of the form Na_xMO_2 (where M is Co, Mn etc.) type metal oxides⁶⁸.

The rather large sized sodium cation also results in sluggish reaction kinetics. Therefore subsequent research on Na-ion batteries has focused on engineering and modifying electrode materials particularly to suit these demands. For e.g. the rhombohedral α - NaFeO_2 has elicited some interest due to its layered structure and rather non-toxic chemistry and has demonstrated a reversible intercalation voltage of 3.3 V⁶⁹. Similarly 3D open structures like Na Super Ionic Conductors (NASICON) have been developed. $\text{Na}_3\text{V}_2(\text{PO}_4)_3$ is a typical NASICON compound that has been studied and it has demonstrated operational voltage of 1.6 V and maximum specific capacity of 93 mAhg^{-1} but its reversibility has been undesirable⁷⁰. A representative charge-discharge curve for the $\text{Na}_3\text{V}_2(\text{PO}_4)_3$ is given in the figure 6 below:

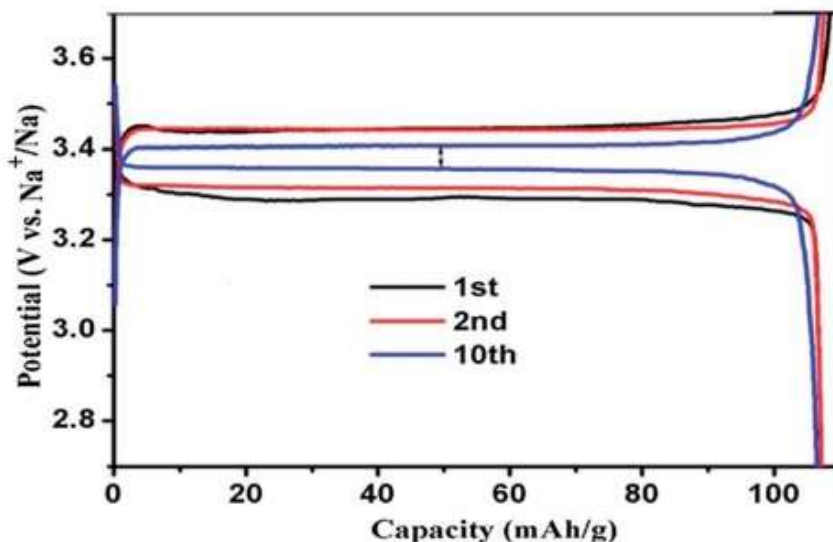


Figure 6. Representative charge-discharge curves for the 1st, 2nd and 10th cycle of $\text{Na}_3\text{V}_2(\text{PO}_4)_3$ cathode⁷¹.

The advantages of the Li-ion batteries i.e. their rather large energy density and operating voltages basically mean Na-ion batteries will have to occupy the niche market where the battery longevity and low cost are the main targets e.g. large scale grid storage^{64,72}. Therefore a compelling rationale exists behind further research and development into Na-ion battery systems and developing an understanding of its fundamental principles in even greater detail. Also the work in this dissertation deals with *aqueous* Na-ion batteries; this is because aqueous systems do away with complicated and expensive fabrication processes that are otherwise needed in cells that use organic electrolyte.

3.3 Material Selection

From the above discussion, it becomes clear that the choice of the positive and the negative electrode materials becomes very important so as to develop a successful and functional Na-ion battery. Some considerations and discussion regarding materials selection is given the following sections.

3.3.1 Cathodes

Exhaustive research has been done in developing novel, long lasting and stable cathode materials for Na-ion batteries. Layered oxide compounds of the type Na_xMO_2 , analogous to LiMO_2 for Li-ion batteries, have been experimented with^{73,74}. Delmas et al. have studied Na_xCoO_2 and an energy density as high as 260 Wh kg^{-1} has been obtained⁷⁵. Dichalcogenide compounds i.e. those having the general formula MS_2 (where M is a transition metal) have been tried by several groups, however their overall electrochemical properties have not been satisfactory^{76,77}.

The material of choice as cathode in this dissertation is *Prussian blue (P.B.)*. P.B. is essentially hexacyanoferrate with $\text{Fe}_4[\text{Fe}(\text{CN})_6]_3 \cdot x\text{H}_2\text{O}$ being its most typical form, though other analogues exist with a general formula $\text{A}_x\text{M}[\text{Fe}(\text{CN})_6]_y$ where A is an alkali metal (e.g. Na, K etc.) and M is a transition metal (e.g. Ni, Zn etc.)^{78,79}. The first study of the chemical and crystal structure of Prussian blue was performed by Keggin and Miles using powder diffraction data⁸⁰. It has been conclusively shown that Prussian blue has a cubic crystal structure in which Fe^{2+} and Fe^{3+} ions are located alternatively on a Face Centered Cubic (FCC) lattice^{81,82}. It has also been demonstrated that the P.B.s exhibit rather large interstitial spaces and these spaces can be useful for hosting alkaline metal ions (e.g. Na^+ , K^+ etc.) during the intercalation process⁸¹. It is because of these properties that they usually do not undergo much lattice deformation and provide longevity, which is a very desirable property. A schematic diagram of a typical P.B. crystal system is shown in the figure below.

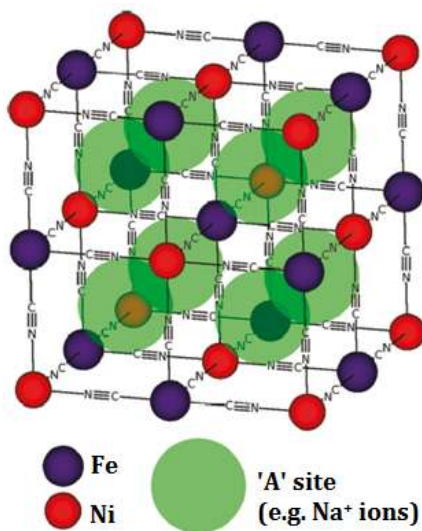


Figure 7. Schematic representation of the structure of a typical Prussian blue crystal⁸¹.

Several studies have been performed on the application of P.B.s as cathode materials in batteries. Okubo et al. have used core shell Cu and Fe based PB based nanoparticles in sodium batteries and have reported relatively stable performances; 60% capacity retention at a discharge rate 600 mA g^{-1} ⁸³. An Na-Zn based hexacyanoferrate based system has been used as a positive electrode in a sodium battery by Lee et al and they have demonstrated a maximum specific capacity of 56.4 mAh g^{-1} with a capacity retention of 85.2% up to 50 cycles⁸⁴. PB as a cathode in aqueous media have been studied by Wu and coworkers, using a $\text{NaTi}_2(\text{PO}_4)_3$ anode⁸⁵. An energy density of 42.5 Wh kg^{-1} have been obtained with a capacity retention of 88 % over 250 cycles⁸⁵.

3.3.2 Anode

Different classes of materials with varying crystallographic morphologies and microstructures have been examined for the anodes of Na-ion batteries. Hard carbon is one of the materials that has been extensively studied as an anode^{67,86}. Another important class of materials that has been useful as negative electrodes are intermetallics. However, in intermetallics, it is alloying that helps to bind the Na^+ ions together rather than intercalation. SnSb/C, is one such intermetallic composite that provided a maximum specific capacity of 544 mAhg^{-1} and a Coulombic efficiency of 98% during cycling⁸⁷. NASICON type materials e.g. $\text{Na}_3\text{Ti}_2(\text{PO}_4)_3$ with rhombohedral crystal structure are a novel class of compounds that have elicited interest and has been tried as an anode and have demonstrated reasonable stability in neutral as well as strongly basic (pH=11) environments⁸⁸.

Transition metal oxides (TMOs) have been chosen as anodes for the aqueous Na-ion batteries in this thesis. TMOs provide several advantages; firstly they have highly flexible

crystal structures which can modify themselves accordingly during the intercalation process⁸⁹. Secondly their relatively large interstitial spaces are expected to serve as good hosts for storage of large sized ions⁸⁹. Another important reason for using TMOs is because of the type of bonding necessary to host the Na^+ ions. These oxides usually have a large multi-ionic layered structure and this structure is beneficial in hosting and stabilizing the rather large sized Na^+ ion⁹⁰. Also this type of structure helps to form a 6-fold co-ordination bond which the Na^+ ion prefers most when it is hosted interstitially⁹⁰. The schematic diagram below demonstrates the variety of structures exhibited by some common TMOs.

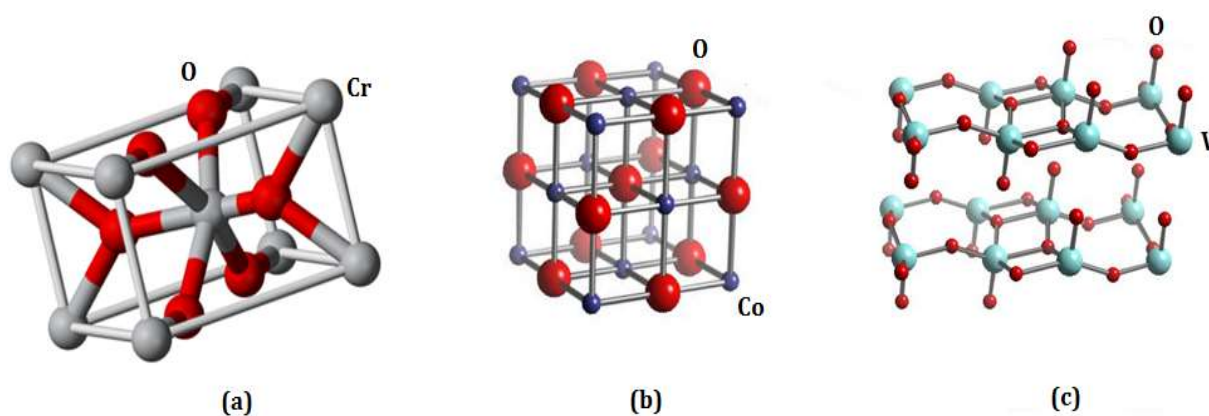


Figure 8. Schematic ball and stick representation of (a) tetragonal CrO_2 (b) simple cubic CoO and (c) orthorhombic V_2O_5 .

Other pertinent advantages of TMOs include their high electrical conductivities and relative insolubility in water which makes them relatively stable in aqueous environments⁹¹. There have been some notable work to further the application of TMOs in Na-ion batteries, in both organic and aqueous environments, a few of which are summarized below.

In organic media, Balaya et al. have been able to obtain a maximum specific capacity of 643 mAhg^{-1} with Fe_3O_4 anodes, however they encountered a 50 % capacity drop after subsequent cycling⁹². Nanostructured Fe_2O_3 have been reported to provide specific capacities of 250 mAhg^{-1} ⁹³. $\alpha\text{-MoO}_3$ has been reported to provide a maximum specific capacity of 771 mAhg^{-1} in its first cycle and has shown good capacity retention over 500 cycles of operation⁹⁴.

In aqueous media, NaV_3O_8 has been tried as an anode material and has proven to be stable for approximately 150 cycles⁹⁵. However, they suffer from rapid initial capacity fade and the maximum capacity that has been obtained is rather low ($\approx 30 \text{ mAhg}^{-1}$)⁹⁵. Wu et al have demonstrated MnCo_2O_4 to be a relative stable anode material in aqueous media, with discharge capacity being 244 mAhg^{-1} even after the 40 cycles at discharge rates as high as 50 mA g^{-1} ⁹⁶.

3.4 Objectives and intellectual merits

An important intellectual merit of studying the sodium ion battery is to probe into the different electrode structures that can be fabricated as well as how the microstructural tuning affects the electrochemical properties. Most of the electrode structures and materials chosen for Na-ion batteries are analogous to those which are used for Li ion batteries and there is great scope for a better understanding of the degradation mechanism involved in the charging-discharging process. As mentioned briefly in a previous section, the fundamental issues faced by current Na-ion batteries can be elucidated as follows:

- Host lattice deformation occurring due to significant volume expansion necessary to accommodate the large Na^+ ion.
- Sluggish kinetics of the Na^+ ion due its large size.

- Corrosion that takes place at the electrode-electrolyte interface.

It is well known the continuous lattice expansion and contraction that occurs to accommodate the large Na^+ ion produces significant stress on the electrode and thereby leads to its eventual degradation, loss in capacity and poor longevity. During this process, due to the continuous loss in structural integrity, the available reaction sites are also lost on the electrode surface thereby weakening its kinetics as well. Therefore the objectives can be summarized as follows.

(i) To develop a fundamental understanding of the structure-property relations of the electrode material – Structure property relations are important in as they strongly influence the electrochemical properties. The relation between structure, morphology and properties are studied in three different ways.

Studying the effect of variation of precursors and fabrication conditions (fabrication time, temperature etc.) is an important objective. These different fabrication conditions provide different morphologies and surface areas and studying these variations is an important objective. Apart from morphology change and surface property variations, another objective is to study the effect of doping on the changes in lattice parameters and how crystal lattices respond to dopant atoms of different sizes. Finally, doping is done in even more significant amounts with the objective of probing a structural change altogether.

(ii) Analyzing structural deformation and degradation by studying structural changes and kinetics as a result of electrochemical cell cycling - Another important aspect to study is the effect of these morphological/structural changes on the deformation in the electrodes due to the wear and tear imposed on the lattice structures by cell cycling. A successful understanding of the interfacial and degradation phenomena will help in understanding

ways to improve longevity of the battery and thereby assist in to furthering the evolution of sustainable energy storage and lessen the dependency on fossil fuels. An important part of this objective is to understand if there is an “optimum” or “best performing” morphology or lattice structure which delivers maximum capacity and longevity under all conditions.

Another important intellectual merit is the study of aqueous batteries. Aqueous batteries provide several advantages than their organic electrolyte counterparts; quick and easy fabrication, less energy intensive cell assembly, lower overheads and overall more affordability. However most of the research community’s focus has been on organic electrolyte based cells, and therefore a detailed study on aqueous rechargeable batteries especially Na-ion is essential.

3.5 Instrumentation

This section discusses as well as provides a brief idea about the instruments used for the purpose of performing the structural characterization as well as studying the electrochemical performance of the cell.

3.5.1 Structural and particle property characterization techniques and instruments

(i) X-Ray diffraction (XRD)

XRD is one of the most powerful experimental techniques that allow for the study of structural properties of crystalline materials. The principle of Bragg’s law utilizing diffraction of X-Rays from lattice planes provides important information regarding crystal structure, lattice parameters etc⁹⁷. XRD was performed by a Bruker D8™ diffractometer using Cu K- α radiation. The diffractometer is used in the θ -2 θ arrangement and the XRD diffractometer is shown in the figure below.



Figure 9. Bruker D8™ diffractometer used for performing XRD of crystalline samples.

(ii) Raman spectra

Raman spectroscopy is essentially a technique which relies on the inelastic scattering of a monochromatic irradiation source⁹⁸. The scattered photonic energies are either more or less than the incident radiation and this “shift” (denoted the Raman Effect or Raman shift), which occurs due to the interaction of the incident radiation with the vibrating molecules, contains important information about the bonding and molecular structure⁹⁸.

The Raman spectra were studied by using a red HeNe laser having wavelength 632.8 nm by an InVia Renishaw™ Raman microscope. The Raman microscope is shown in the figure below.



Figure 10. The InVia™ Renishaw Raman microscope used for performing Raman spectra.

(iii) Electron microscopy

Electron microscopy provides important information regarding the surface morphology, microstructure as well as its lattice structure. Scanning electron microscopy is used to study the surface properties of the material and provide an idea about its external morphology. The SEM works on the principle of a beam of electrons scanning the surface of the material, and thereby imaging the microstructure⁹⁹. The SEM is also used to perform Energy dispersive X-Ray spectroscopy (EDX) which provides information about the chemical composition of the sample under analysis. A TESCAN SEM and a FEI Nova NanoSEM 600 was used for this purpose and are shown in figure 11 below.



Figure 11. (a) TESCAN™ SEM and (b) FEI Nova NanoSEM™ 600.

A transmission electron microscope (TEM) on the other hand not only provides external morphological information, it is also used to study the lattice information of the sample in question. The incident energetic beam of electrons are “transmitted” through the sample and are scattered which are then recorded and provide important crystallographic information¹⁰⁰. A TECNAI™ G2 F30 TEM is used for imaging purposes and is shown in figure 12 below.

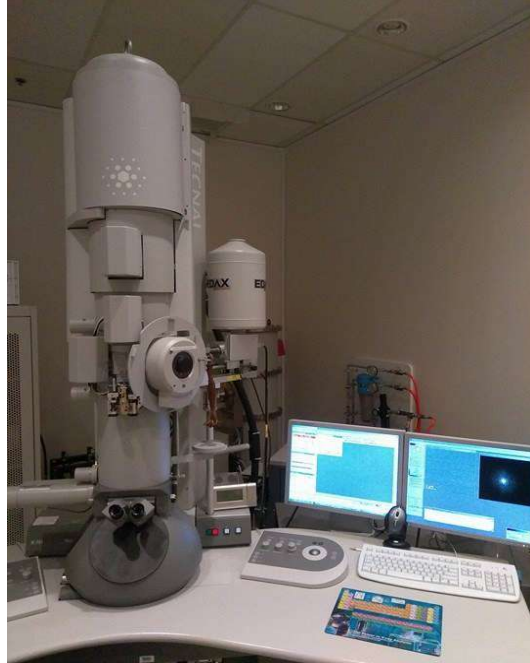


Figure 12. TECNAI™ G2 F30 TEM used for imaging and analysis purposes.

(iv) X-Ray Photoelectron Spectroscopy (XPS)

XPS is an important materials characterization technique which is used to provide important information regarding the surface properties of the sample. It works on the principle of photoelectric principle. When a sample is irradiated by an X-Ray beam of required wavelength, it results in an electron being ejected from the sample. Information regarding the elements and the nature of bonding, especially at the surface is obtained by the XPS spectra¹⁰¹. A Thermo VG Scientific MultiLab™ XPS system consisting of a CTX400 X-Ray source is used and shown in the figure below.

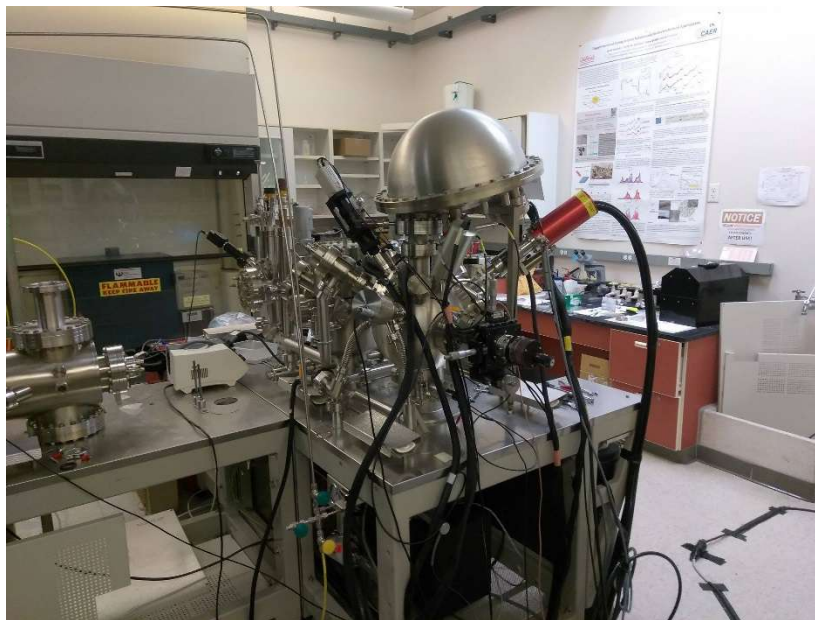


Figure 13. Thermo VG Scientific MultiLab™ XPS used for surface characterization.

(v) Particle size and BET measurements

The principle of particle size measurement involves scattering of laser light by sample particles dissolved in a solvent e.g. water. This scattered light is then used to correlate the particle size. A Brookhaven 90Plus™ Particle size analyzer was used for the purpose of measuring the particle size and is shown in figure 14(a).

Surface area and porosity are important properties that correlate to the electrochemical activity. The surface area measurement is performed by a technique proposed by scientists Brunauer, Emmett and Teller and hence the name BET technique. Experimentally, it essentially involves adsorbing N₂ gas on to the surface of the sample followed by desorption cycle under the assumption that the adsorption rate is essentially equal to desorption rate. The principle of BET is basically an extension of the Langmuir theory¹⁰². BET measurements are performed by a Micrometrics TriStar™ Surface Area and Porosity Analyzer and is shown in figure 14(b) below.



Figure 14. (a) Brookhaven 90Plus™ Particle size analyzer and (b) Micrometrics TriStar™ Surface Area and Porosity Analyzer

3.5.2 Instruments for measuring electrochemical performance

(i) Cell cycling

Galvanostatic cell cycling is essential to understand the performance of the cell to repeated cycles of charging and discharging. A constant charging and discharging current is applied and the capacity output of the cell is monitored. Cell cycling was performed by an Arbin BT2043™ instrument and is shown in figure 15.



Figure 15. Arbin BT2043™ instrument used for cell cycling.

(ii) Cyclic voltammetry (CV) and impedance spectra

CV is a technique which probes the oxidation and the reduction characteristics of the cell. A fixed potential scan rate is applied in the forward as well as the reverse direction within a designated voltage window and the oxidation and reduction peaks are observed which provide information about the electrode processes¹⁰³.

Electrochemical impedance spectroscopy (EIS) essentially measures the response of a cell to a small a.c. signal. The response in the high frequency region usually corresponds to the impedance due to charge transfer across the electrode-electrolyte interface, whereas that in the low frequency region corresponds to ionic diffusion in to the electrode¹⁰⁴. A Biologic SP-200™ potentiostat was used for CV and impedance spectra measurement.

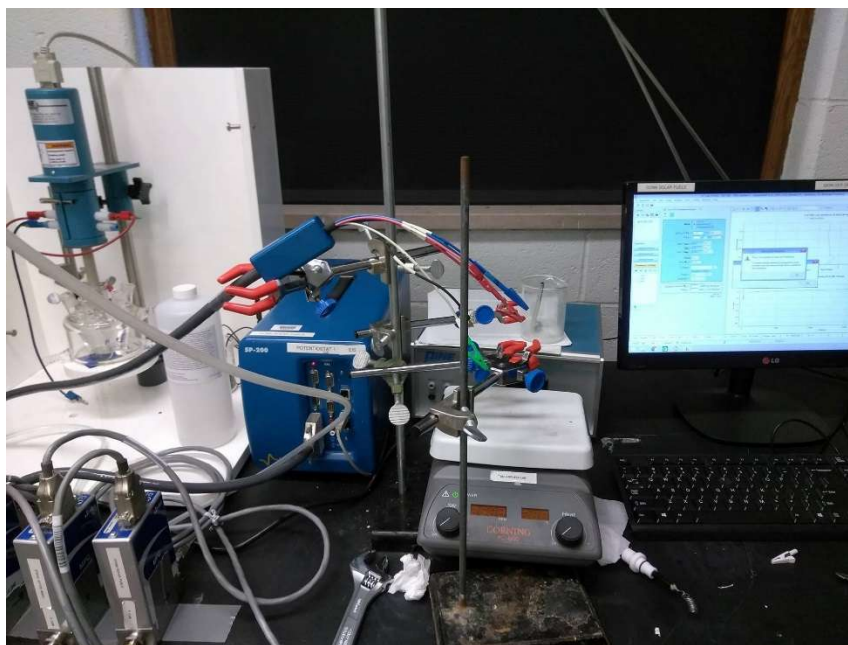


Figure 16. Biologic SP-200™ potentiostat for CV and impedance spectra measurement.

CHAPTER 4

THE CuO - PRUSSIAN BLUE SYSTEM

4.1 Background of CuO systems

Based on the fundamental premise of easy availability, affordability and stability, there has been growing interest in the application of CuO as anode materials^{105,106}. However most of the efforts of CuO anodes have been towards its application in Li-ion batteries. In Li-ion batteries, CuO systems have provided specific capacities as high as 664.1 mAh g⁻¹ and good stability^{106,107}. Apart from standalone CuO, focus has been more on improving/modifying the CuO microstructure so as to be able to improve its reaction kinetics as well as enhance capacity retention properties. A CuO/graphene composite has been studied by Mai et al. and a reversible capacity of 583.5 mAh g⁻¹ has been obtained with capacity retention of about 75.5 %¹⁰⁸. Nanostructured carbon coated CuO having hollow spherical morphology has been studied by Xu et al¹⁰⁹. The authors have reported a maximum specific capacity of 670 mAh g⁻¹ at a discharge rate of 1 C and have been able to maintain its capacity for approximately 300 cycles of operation. The superior morphological properties of these hollow nanospheres were responsible for the high capacity retention¹⁰⁹. Mesoporous CuO particles, as studied by Ko et al. have also been successful in providing elevated discharge capacities of 650 mAh g⁻¹ especially at low discharge capacities of 0.1 C¹¹⁰. Basically they had fabricated a nanocomposite consisting of mesoporous CuO “threaded” with carbon nanotubes and the excellent performance has

been attributed to this unique morphology¹¹⁰. Along similar lines, CuO/graphene based nanocomposites have been fabricated by Wang and coworkers as “high-performance anodes” in Li-ion batteries¹¹¹. According to the authors, the CuO nanoparticles are embedded in a 3D graphene network and they have been able to obtain a maximum discharge capacity of $\sim 600 \text{ mAh g}^{-1}$ at a current density of 65 mA g^{-1} . The authors have attributed this excellent performance to the 3D network which greatly improved the electrical conductivity and stability of the overall structure¹¹¹. CuO nanoparticles grown on Cu substrates for Li-ion batteries were tried by Wang and coworkers¹¹². They typically fabricated these nanostructures using a $\text{Cu}(\text{NO}_3)_2$ solution precursor into which a Cu foil was dipped and the reaction was allowed to proceed hydrothermally. The authors have reported a very large first cycle discharge capacity of 1500 mAh g^{-1} which dropped to 580 mAh g^{-1} in the second cycle, at a discharge current of 0.5 C ¹¹². This big drop has been ascribed to irreversible side reactions and the formation of a SEI layer which prevents smooth Li insertion¹¹². Lu and Wang have fabricated ‘sheet-like’ CuO nanostructures on graphene for applications as anodes in Li-ion batteries¹¹³. A microwave irradiation technique was used with $\text{Cu}(\text{CH}_3\text{COO})_2$ and graphene nanosheets as the precursor materials. The graphene based CuO nanostructures have demonstrated enhanced initial discharge capacities of 1092 mAh g^{-1} as against pristine CuO (non-graphene based) which demonstrated an initial discharge capacity of 657 mAh g^{-1} at 0.1 C discharge rates¹¹³. The authors have attributed this large improvement to improved porosity of the graphenated CuO nanostructures¹¹³. Metal organic framework (MOF) based precursors has been used as precursors for fabricating porous hollow CuO octahedra as anodes in Li-ion batteries by Wu et al¹¹⁴. The octahedra were prepared from

$\text{Cu}_3(\text{btc})_2$ precursors (where btc is benzene 1,3,5-tricarboxylate)¹¹⁴. Electrochemical results have demonstrated a rather large initial cycle discharge capacity of 1208 mAh g^{-1} (almost twice the theoretical capacity) which stabilized to 470 mAh g^{-1} after 100 cycles¹¹⁴. This significant drop in capacity has been attributed to irreversible side reactions and Li storage as well as the formation of SEI layer¹¹⁴.

However the application of CuO as anode materials in Na-ion batteries has been relatively sparse¹¹⁵. Electrochemical analysis of Na^+ ions in CuO have been studied by Wang et al. who have reported the formation of an intermediate $\text{Cu}_{1-x}\text{O}_2$ complex during cell cycling¹¹⁶. It has also been reported that CuO acts as a conversion anode w.r.t Na ions rather than the usual intercalation host material¹¹⁶. Yuan et al. have used Cu foil as a precursor to obtain porous CuO arrays as anodes in Na-ion batteries¹¹⁷. They have reported a stable specific capacity of 640 mAh g^{-1} and a maximum of 935 mAh g^{-1} at a relatively high current density of 200 mA g^{-1} . However they have reported low initial Coulombic efficiencies of 61 % which have been attributed to SEI layer formation¹¹⁷. An aerosol based spray pyrolysis technique was used by Lu et al. to develop carbon coated CuO (CuO/C) nanoparticles¹¹⁸. Electrochemical performance indicated that a stable discharge capacity of 402 mAh g^{-1} was still available after about 600 cycles of operation¹¹⁸.

However, there is no detailed analysis of application of CuO as anodes in aqueous sodium ion batteries and an investigation of the same is absolutely necessary if the advantages of CuO are to be reaped in aqueous media as well.

4.2 Rationale and outline

The aim of this project is to study the effect of microstructure on electrochemical kinetics. As noted earlier, kinetics and preserving the structural fidelity of the electrode are two of the primary concerns of a Na-ion battery system. Electrode morphology and microstructure can be considered to be one of the most important parameters which influence the kinetics. Therefore, fabricating and realizing the effect of optimum microstructure variation on cell performance is essential to provide improved electrochemical kinetics. Consequently, this project focuses on developing several CuO microstructures by facile, less energy-intensive but relatively novel techniques. Detailed electrochemical analysis is then performed to understand the role the respective morphologies play and determine the optimum microstructure which provides the most suitable results.

4.3 Fabrication

Fabrication methods for the cathode and anode are provided as below:

4.3.1 Cathode

Prussian blue (P.B.) was used as the cathode material. For its fabrication, 3 mmol of $\text{Na}_4\text{Fe}(\text{CN})_6 \cdot 10\text{H}_2\text{O}$ was dissolved in 40 ml of 0.1 M HCl. This solution was vigorously stirred at 500 rpm for 5 min. Once this was done, the resulting solution was dried at 80 °C in air for 20 hours. This resulted in sodium rich Prussian blue which was used as the cathode.

4.3.2 Anode

Four different types of CuO anodes are used in this project, with variations in their microstructure. The techniques used to fabricate these are described in detail below in the following sections:

(i) *CuO as obtained (CuO_{as ob.})* – This is the most basic type of the anode used. Basically, this is used in the same form as obtained from Sigma Aldrich.

(ii) *CuO ribbons (CuO_{ribbons})* – The CuO ribbons are prepared by a solution based wet chemistry technique. 4 mmol of CuCl₂·2H₂O is mixed with 0.71 mmol of citric acid and 60 ml of deionized (D.I.) water is added to prepare a solution with stirring. Subsequently, 100 mmol of NaOH is added to the previously formed solution and a blue precipitate of Cu(OH)₂ is immediately formed. This solution is stirred for about 10 – 15 minutes, and the precipitate is retrieved after several rounds of thorough centrifugation with ethanol and D.I. water. The precipitate was dried on a hot plate and finally heated at 400 °C in a muffle furnace to obtain the CuO ribbons. This technique has been used by Wang et al. to develop CuO nanowires¹¹⁶.

(iii) *CuO spherical platelets (CuO_{platelets})* - A similar solution based wet chemistry technique was used to fabricate the spherical platelets. The precursors used in this case were CuSO₄·5H₂O, KOH and commercial NH₃. Appropriate amounts of 0.4 M CuSO₄·5H₂O solution was mixed with 0.48 M KOH solution followed by the addition of 0.9 ml of NH₃ and 15 ml of D.I. water under stirring to form a uniform dark bluish solution. Once this dark blue solution was obtained, it was kept in a water bath and incubated at about 68 °C for about 45 minutes. Finally the dark greyish black precipitates were centrifuged with ethanol and water and dried on a hot plate at 50 °C overnight before use. Qin et al. have used this technique to fabricate porous CuO hollow spheres¹¹⁹.

(iv) *CuO spheres (CuO_spheres)* – Spheres were prepared by a process originally used by Wang et al. for fabricating controlled CuO spheres for organic Li-ion batteries¹⁰⁷. In this case, the precursor materials were $\text{Cu}(\text{NO}_3)_2$ and anhydrous sodium carbonate, 2.42 g and 1.06 g respectively of which were mixed in 50 ml of D.I. water under stirring. After this, this solution was incubated in a water bath at 70 °C for 2 hours and then the bluish green precipitates were retrieved by thorough centrifugation and filtration. They were dried overnight and finally calcined at 400 °C for 2 hours in a muffle furnace to obtain the CuO spheres.

4.4. Structural characterization

Structural characterization results and analysis of the cathode and anode are discussed in greater detail in the following sections.

4.4.1 Cathode

(i) XRD

Figure 17(a), demonstrates XRD data of the P.B. sample. The prominent peaks labeled here are the (220), (400), (420), (511) and (440) peaks, respectively, and all peaks can be matched and indexed from the standard ICDD database (01 – 073 – 0687). The absence of any impurity peaks indicates the phase purity of the sample.

(ii) Raman spectra

The characteristic Raman spectrum is demonstrated in figure 17(b). Once again, there are no impurity peaks and two of the important peaks have been labeled at 2151.69 cm^{-1} and 287.12 cm^{-1} .

(iii) SEM imaging

Figure 17(c) shows the SEM images of the Prussian blue cathode taken at a resolution of 2 μm . As evidently noticeable, the P.B. samples exhibit a highly cubic external morphology. These well defined cubes are prevalent throughout the sample and the results match very well with published literature¹²⁰.

(iv) Particle size analysis

Figure 17(d) shows the particle size for the P.B. based cathode system. As can be seen from the graph, the particles are in the range of 350 nm to 550 nm. The average effective size of the particles is approximately 450 nm.

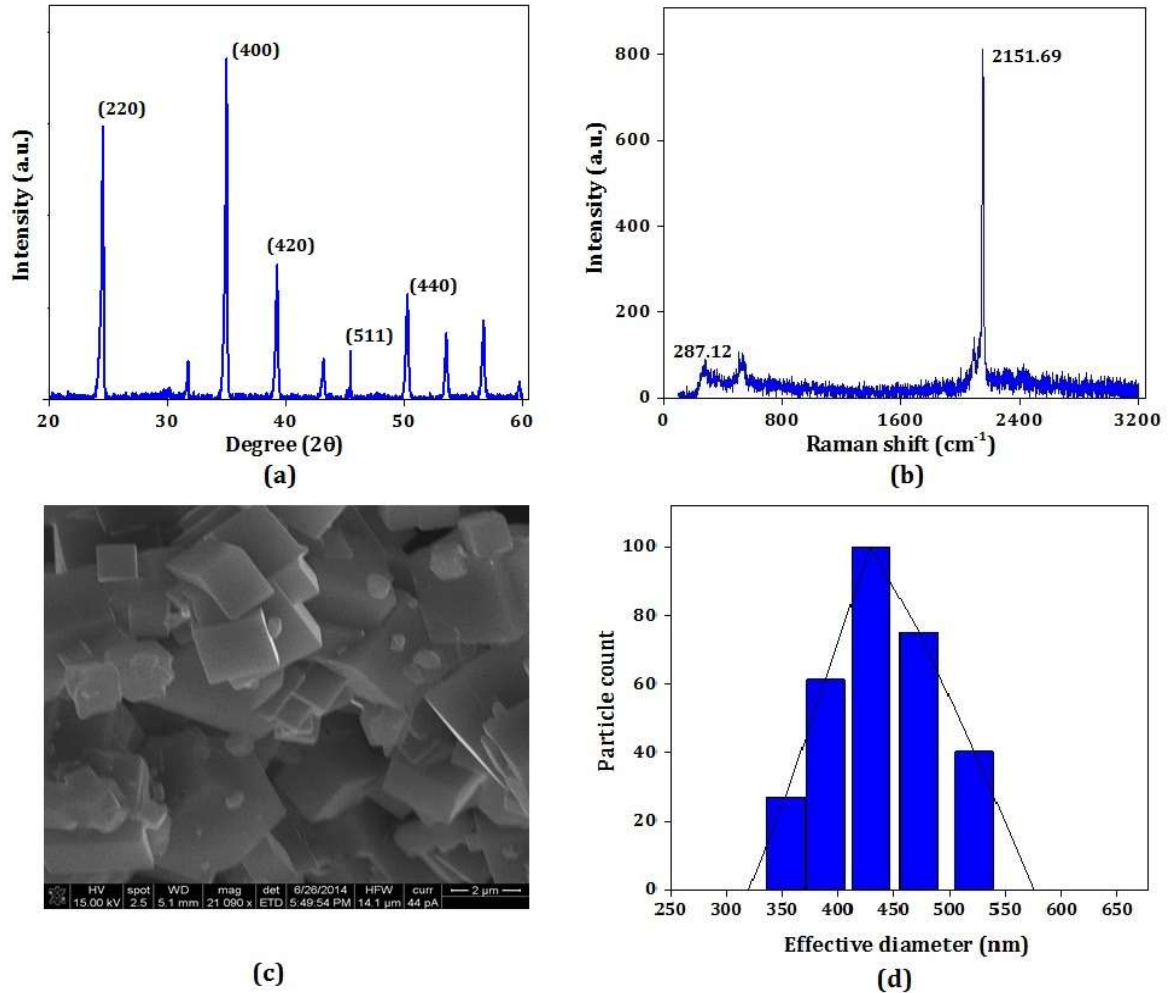


Figure 17. (a) XRD spectra of P.B. sample (b) Characteristic Raman spectra of the P.B. sample (c) SEM images showing the characteristics P.B. cubes (d) particle size distribution of the P.B. samples.

4.4.2 Anode

Structural characterization of the various CuO samples are performed and illustrated as below.

(i) XRD spectra

The XRD of the different CuO morphologies is as provided in the figure below:

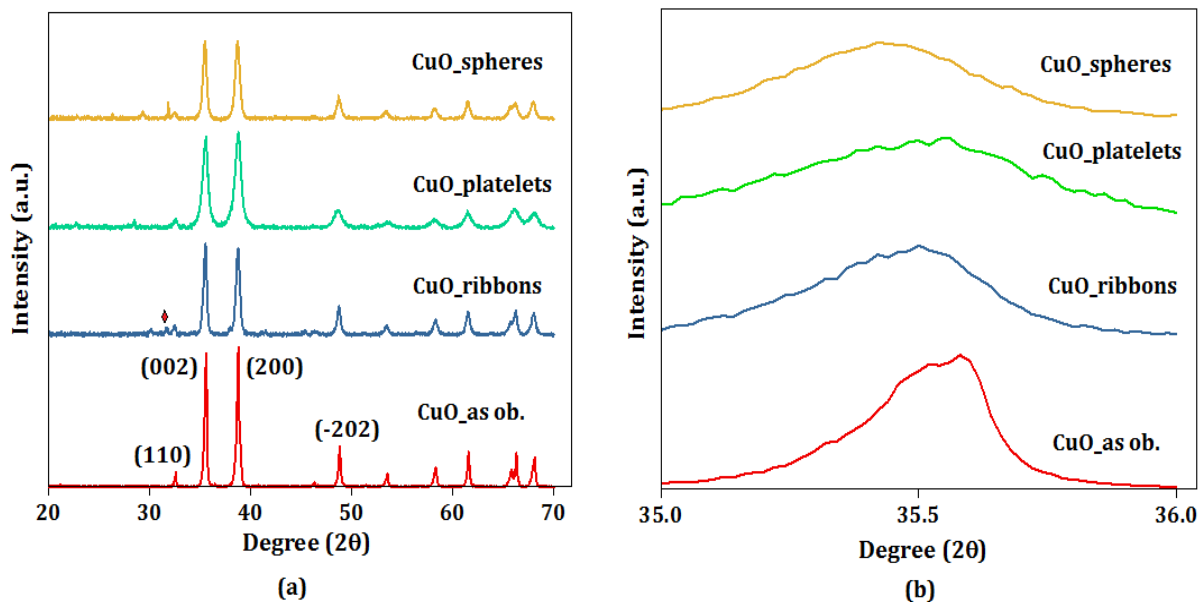


Figure 18. (a) Represents the full spectrum XRD data with the important peaks labeled and impurity peaks starred and (b) is the (002) peak in greater detail.

Figure 18(a) demonstrates the full XRD spectra of the different CuO morphologies. The important peaks i.e. the (110), (002), (200) and the (-202) peaks have been labeled indexed from the ICDD database (00-002-1041). As can be seen the three different morphologies essentially maintain the same general peak positions as the as obtained sample. The star marked peaks indicate the remnants of small amounts of $\text{Cu}(\text{OH})_2$ impurities (00-003-0310). Figure 18(b) is an exaggerated illustration of the (002) peak in greater detail. Some degree of peak broadening and loss of intensity is noticed indicating small amounts of crystallite size variation and loss of crystallinity; however no noticeable peak shift suggests consistent lattice parameters with the literature. Therefore they all exhibit a monoclinic structure with lattice parameters approximately being $a = 4.65 \text{ \AA}$, $b = 3.41 \text{ \AA}$ and $c = 5.11 \text{ \AA}$ with space group being $A2/a$ (00-002-1041).

(ii) SEM imaging

SEM imaging was performed with a TESCAN SEM. The images of the four different CuO samples taken at resolutions of 5 μm are shown in the figure below.

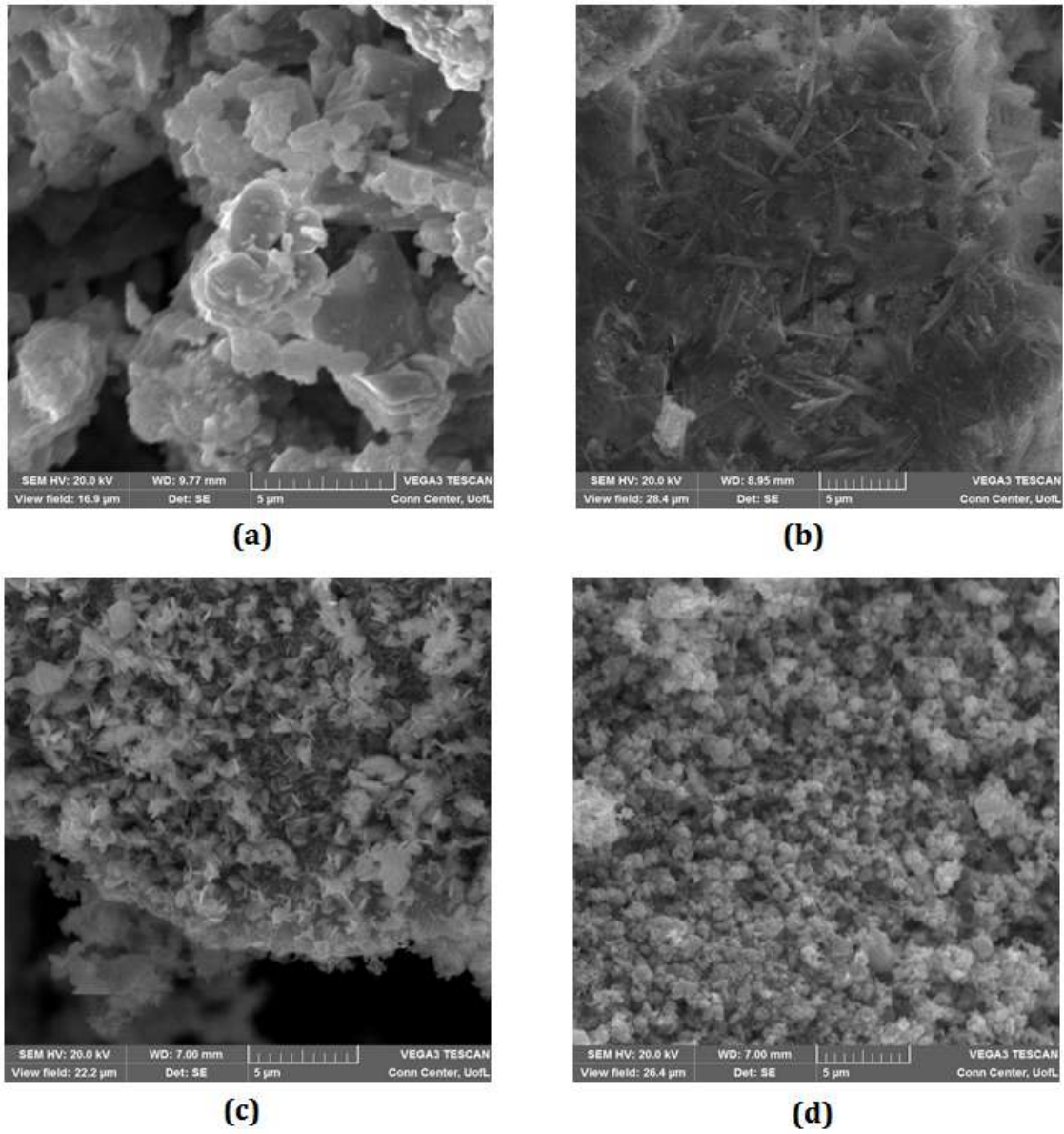


Figure 19. (a) CuO as obtained sample (b) CuO ribbons (c) CuO platelets and (d) CuO spheres.

Figure 19(a) demonstrates the CuO_{as} obtained samples. As can be seen, they are rather large sized with random shapes and exhibit no particular morphology. Figure 19(b) are the images of the ribbon sample and they demonstrate short elongated band like one dimensional morphology, hence the name. Figure 19(c) demonstrates the spherical platelets (or simply platelets). These samples exhibit small plate like protrusions closely bundled together. Overall the plates grouped together roughly resemble a sphere if joined together, but since the Ostwald ripening process was done for a short period of time, the plates remained as is and is as seen in the figure. The CuO spheres are seen in figure 19(d) and demonstrate a well-rounded microstructure. Also the figure indicates a large number of these spheres are closely packed together.

(iii) Particle properties

Particle properties can be distinguished into particle size and porosity analysis. They are explained in detail as follows:

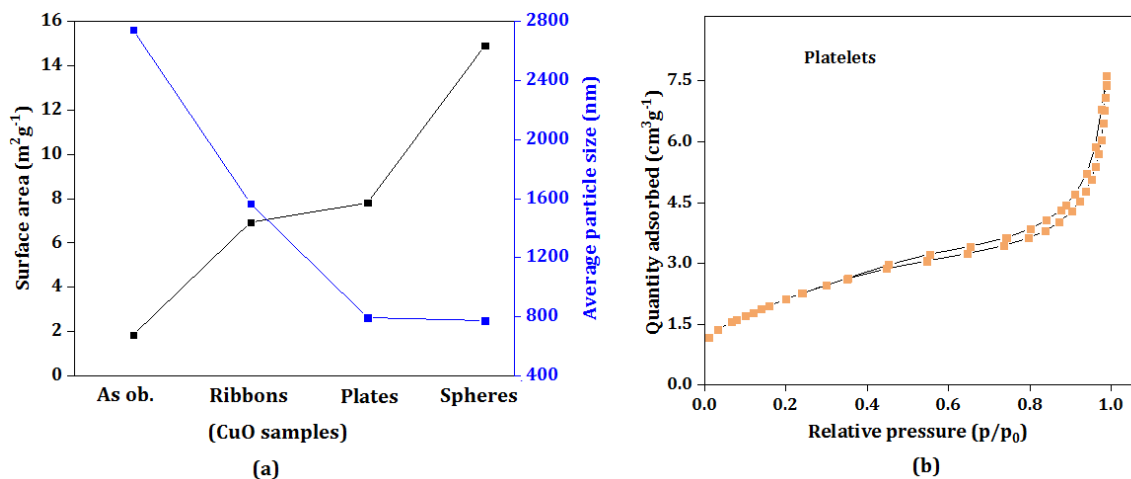


Figure 20. (a) Trend of BET (in black, left y-axis) and particle size (in blue, right y-axis) for the different CuO samples. (b) Representative BET adsorption-desorption curve of the CuO_{platelets} sample.

Porosity analysis was performed by the BET technique using liquid N₂ gas for studying the adsorption and desorption properties. The surface area values for each of the samples are shown in figure 20(a) in with black trend lines and are on the left y-axis. The as obtained CuO samples show relatively less surface area (1.8537 m²g⁻¹). The ribbons show a significantly higher surface area of 6.93 m²g⁻¹, indicating a considerable increase in porosity. The platelets demonstrate a slightly higher surface area of 7.81 m²g⁻¹ demonstrating a likewise incremental porosity increase than the platelet sample. The spheres exhibit a considerably elevated surface area of 14.89 m²g⁻¹ which indicates that the fabrication technique has been able to form significant porosity in the sample. These results indicate how different precursor materials, during the fabrication technique, lead to formation of morphologies with varying surface areas and consequently varying degrees of porosity. Also seen in the figure in the y-axis to the right (in blue trend lines and axes) are the average particle sizes. It shows a corresponding reduction in particle size with increasing surface area. The as obtained samples have relatively large sizes (≈ 2740 nm) whereas the spheres demonstrate relatively smaller sizes of approximately 775 nm. Therefore, it is observed that the overall surface area increases by a factor of 8.03 from as obtained to spheres. Concurrently, the average particle size drops by a factor of 3.53 from the as obtained to the spherical samples. These results match well with the images seen in the SEM. Figure 20(b) is the BET adsorption-desorption curve for the CuO_platelets sample, provided as a sample representative.

4.5 Cell assembly

The electrodes (both the P.B. cathode and the various CuO anodes) are prepared by suspending them in isopropanol and stirring to prepare a uniform solution, followed by

drop casting on a carbon paper substrate. A Whitman glass fiber separator is used and the electrolyte used is 2 M Na₂SO₄. CR 2032 coin cells are used for the purpose of electrochemical measurements. Current rates used are usually 1 C unless otherwise mentioned and the voltage window for galvanostatic charging and discharging is 0 V – 1.6 V. The cell voltages mentioned for the cycling are with respect to the full cell.

4.6 Electrochemical analysis

The results of the electrochemical analysis are as discussed below.

4.6.1 Cell cycling and stability

The first cycle discharge capacities and the stability plots are provided in the figure below.

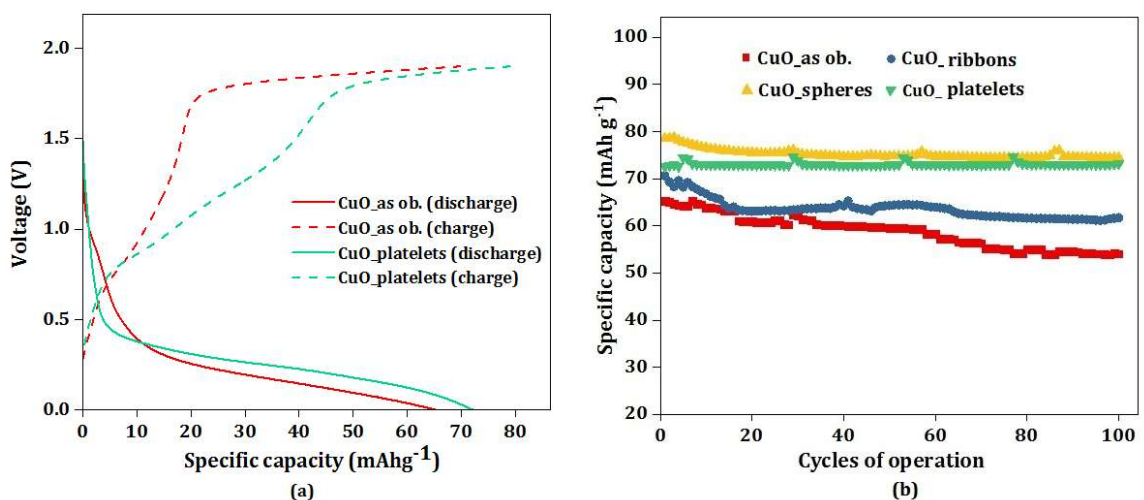


Figure 21. (a) Illustrates the first cycle discharge capacities of the different CuO microstructures and (b) represents the stability plots of the four different CuO anodes.

First cycle charge and discharge curves (in dashed and solid lines respectively) of the CuO platelets and as obtained samples are seen in figure 21(a). Predictably, the platelet sample provides a higher initial discharge capacity of 72.55 mAh g⁻¹ than the as obtained samples which provide 65.20 mAh g⁻¹. The results are in accordance with surface area of

the samples indicating a higher surface area has a direct role in providing higher initial capacities. Larger surface area increases the number of reaction sites available, thereby improving kinetics and the initial discharge capacities obtained. From the figure, the majority of the capacity is obtained in the region around 0.4 V – 0 V, which has been reported by other groups as well¹¹⁷.

From the stability plots in figure 21(b), it is seen that the spheres provide higher starting discharge capacity (78.61 mAh g^{-1}) than the platelets, which again, is in the order of their surface areas. It is also observed that there is an increase in initial discharge capacity of about 20.56 % which corresponds to the ≈ 8 times enhancement in surface area. Also it can be seen that the platelets have the best retention performance as it suffers from practically no specific capacity loss. This is a testimony to the physical toughness of the platelet structures as they are able to withstand the rigors of the cycling process without presumably undergoing much loss in their structure or morphology. The spheres provide higher starting capacity as pointed out in the earlier section, however they suffer slightly more capacity fading ($\approx 5.31 \%$) than the platelets. Therefore the higher surface area of the spheres tends to help in providing more specific capacity, and the spheres too demonstrate reasonable resistance to degradation. The ribbons start off with comparable discharge capacities (70.61 mAh g^{-1}) as the platelets; however they undergo steadier capacity loss and lose about 12.60 % after 100 cycles. The presence of impurities in the ribbon samples render them slightly weaker in terms of stability and this is manifested in its stability performance. The as obtained CuO sample loses about 17.08 % of its starting capacity during the cycling process. Therefore it is observed that the variation in

morphology plays an important role in determining the stability as well as delivering optimum discharge capacity.

4.6.2 C rate analysis

C rate analysis essentially studies the capacity performance of the cell to varying rates of discharge. It provides important information about how the cell performs at fast as well as slow discharge rates and if they are reversible, especially at high rates. C rate analysis was performed to further study the kinetics of the various CuO morphologies. The results are as plotted in the figure below.

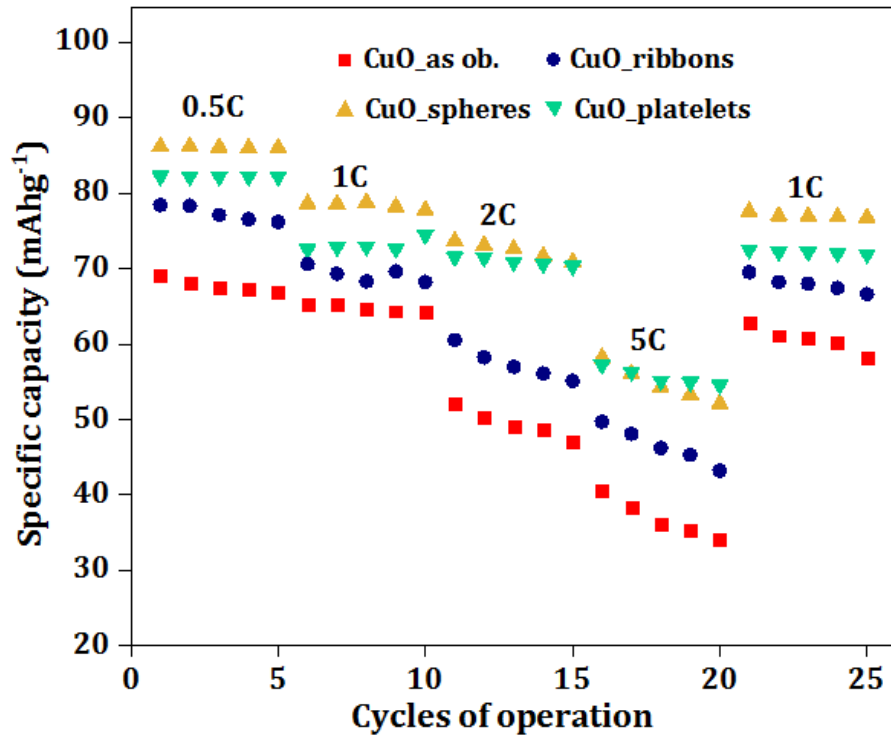


Figure 22. C rate analysis of the various CuO samples.

C rate results indicate a similar trend as seen in the stability results. The CuO_sphere samples maintain their rate superiority for slower C rates viz. for 0.5 C and 1 C. At about 2 C discharge rates, even though the starting discharge capacity is higher, there is very

little to distinguish to CuO_spheres and the CuO_platelets sample. It can be seen that at considerably higher C rates i.e. 5 C it is the CuO_platelets sample that perform better, especially in terms of stability. Therefore it can be concluded that even though the CuO spheres sample have larger surface area and superior kinetics especially at lower C rates, at higher C rates it is the CuO_platelets sample that performs better. Its toughness and resistance to degradation confers it this ability, whereas very high kinetics can be one reason why the CuO_spheres sample degrades faster as it undergoes very vigorous reactions on its surface. The CuO_ribbons and the as obtained sample consistently perform worse than the other two samples, which is also consistent with results in figure 13(b).

4.6.3 Impedance spectra

Impedance spectra analysis was performed as one of the techniques to probe the kinetics of the system. The results are as provided below.

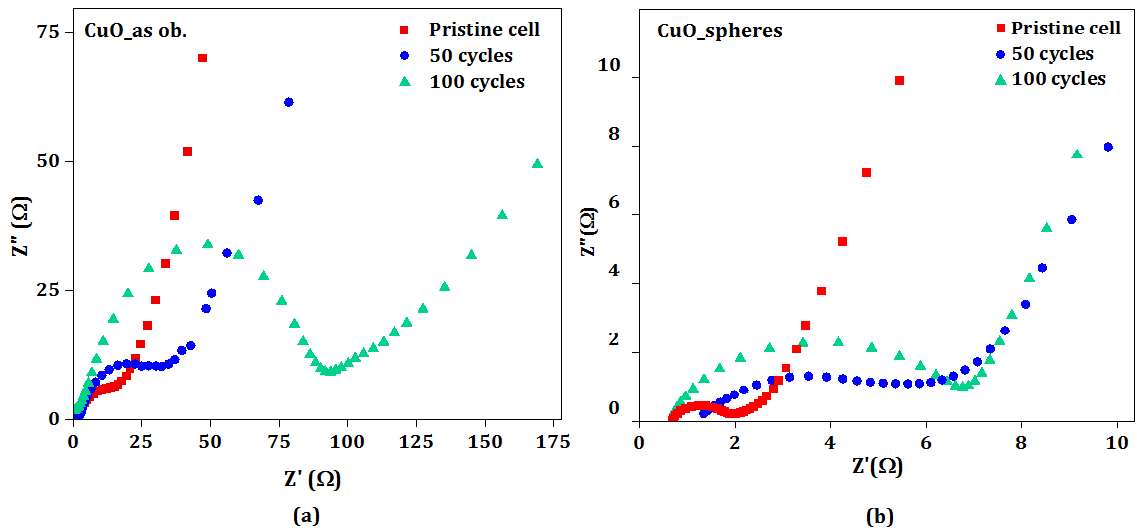


Figure 23. (a) Impedance spectra of CuO_as obtained samples for the pristine, 50th and 100th cycle of operation (b) Impedance spectra of the CuO_spheres for the pristine, 50th and 100th cycles.

The impedance spectra analysis of the CuO_as ob. and the CuO_spheres are shown in figure 15. The impedance spectra have been recorded for the pristine cell, after 50 cycles of operation and after the completion of the 100th cycle respectively. Significant observations can be drawn from figures (a) and (b). It is noticed that the characteristic impedance spectra can be resolved into two distinct regions; an inverted semicircular region and a linear region. It is this inverted semicircular region that corresponds to charge transfer across the electrode-electrolyte interface, which is a direct measure of the electrochemical kinetics. As can be seen from the figure, the radius of the semicircles increase in a much more exaggerated manner for the CuO_as obtained sample than the CuO_spheres. This indicates a much lower electrochemical impedance value for the CuO_spheres at each stage of cycling with respect to the as obtained sample. Therefore, this can be correlated to the larger surface area of the CuO_spheres sample which in turn provides for its superior electrochemical kinetic behavior.

The impedance spectra comparison of the pristine and post cycled cells of the sphere and platelet samples is shown in the figure below.

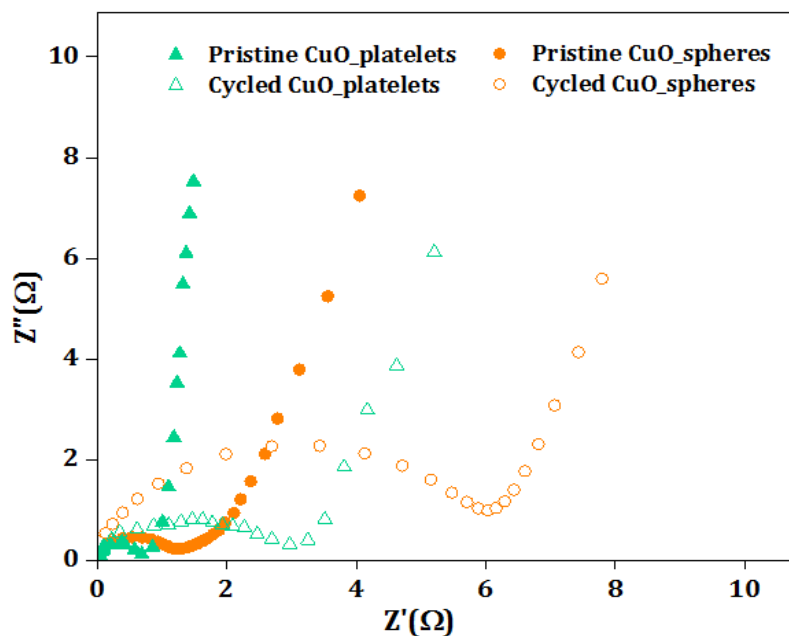


Figure 24. Comparative impedance spectra of pristine and post cycled CuO_spheres and CuO_platelets.

From this figure it is seen that the interfacial impedances of the platelet samples under both conditions (pristine and post cycled) are lower than those of the spherical samples. It can be inferred from here that the sphere samples lose their electrochemical activity in this high frequency region (which can be considered to be a close approximation of the high C rate regime) at a faster rate than the platelet samples, which consequently contribute to their poor performance at high discharge rates.

4.6.4 Post cycled XRD analysis of mechanism of electrode degradation

Post cycled XRD was performed to study the degradation of the electrode materials, especially to study the comparison between the sphere and the platelet samples. The post cycled XRD results (with normalized peak intensities) for the pristine and post cycled

platelets and sphere samples are shown in the figure below. The results have been taken when the cells have been cycled at 5 C rate.

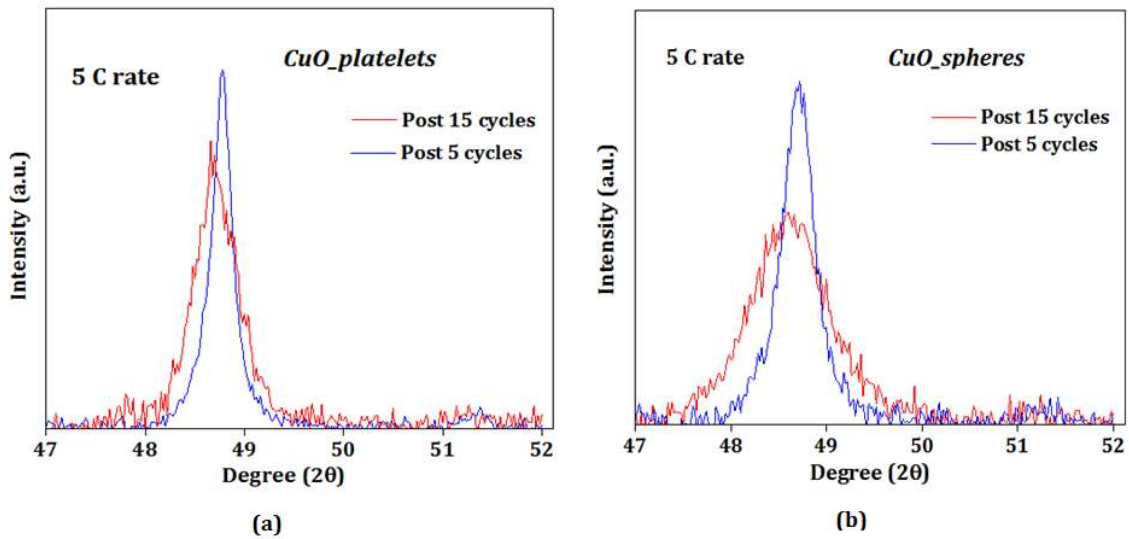


Figure 25. Comparative post cycled XRD graphs of (a) platelet and (b) spherical samples.

It is observed from figures (a) and (b) that there is considerable peak shift and broadening in the case of the spherical sample than the platelet sample, between the 5th and 15th cycles. This indicates a greater degree of loss of crystallinity and structural degradation of the spherical samples than the platelets. As a result, the platelet sample is able to retain its structure better than the spherical sample which explains its improved capacity retention, especially at higher discharge rates. High surface area indicating higher porosity can be attributed to the relative structural weakness of the spherical samples.

4.7 Conclusion

An analysis has been performed in this project to study the effect of morphology on electrochemical kinetics. Results indicate the surface area plays a direct role in determining the kinetics at both low and high C rates. An almost two-fold enhancement in surface area (spheres over platelets) does provide a higher initial capacity, especially at low rates (0.5 C, 1 C), however the effect of this enhancement in surface area is not realized at higher C rates where its stability is markedly poor. Therefore, an important outcome of this project is that the morphology with the best performing kinetics doesn't not necessarily provide the best stability. As has been demonstrated in the previous sections, the CuO_spheres samples perform better when it comes to kinetics and initial discharge capacity, but it is the platelet sample which suffers almost no appreciable capacity loss. Thus it can be concluded that the development of an optimal microstructure is an interplay between several important parameters and a particular morphology should be chosen to fit the particular application in question.

CHAPTER 5

THE Fe₂O₃ - PRUSSIAN BLUE SYSTEM

5.1. Background of Fe₂O₃ anodes

There has been considerable interest recently in the use of iron oxide, especially hematite (α -Fe₂O₃), for a variety of materials science applications. The relative abundance (Fe being the fourth most abundant element in the earth's crust) of iron makes it relatively inexpensive to mine and use¹²¹. Hematite crystallizes in the rhombohedral corundum structure and has found applications as magnetic materials, gas sensors, field emitters and as anodes in Li-ion and Na-ion batteries¹²²⁻¹²⁵.

In electrochemistry, α -Fe₂O₃ has been mostly studied as an anode in Li-ion batteries. Pioneering work to understand the functioning of α -Fe₂O₃ anodes was done by Larcher et al. who have conclusively proven that fine nanosized particles behaved distinctly different from their micron sized counterparts and this affected the structural stability as well as the kinetics¹²⁶. Different Fe₂O₃ morphologies have also been tried in Li-ion battery applications, especially in organic environments. α -Fe₂O₃ nanorods as anodes in Li-ion batteries has been studied by Li et al¹²⁷. They used a hydrothermal technique to fabricate the hematite particles and a maximum discharge capacity of 908 mAh g⁻¹ was reported at a 0.2 C discharge rate¹²⁷. Hollow spheres of Fe₂O₃ coupled with polyaniline (Fe₂O₃@polyaniline) were fabricated by Jeong and coworkers for applications as anodes in Li-ion batteries¹²⁸. The fabrication followed a 2-step process involving sonication and polymerization of the precursors. A maximum discharge capacity of 950 mAh g⁻¹ was

obtained at 0.2 C rate with good capacity retention¹²⁸. A novel composite of bubbles and nanorods were fabricated by Cho et al as anodes in Li-ion batteries¹²⁹. The structure was basically an agglomeration of Fe₂O₃ spheres in a fibrous C matrix. Stable capacities of 812 mAh g⁻¹ after 300 cycles with capacity retentions of 84 % from the second cycle were obtained¹²⁹. Fe₂O₃ has also been used a composite anode, coupled with Co₃O₄ by Wu et al. The composite anodes have been prepared by a simple hydrothermal process¹³⁰. The overall nanowire morphology was used to enhance the reaction surface area and improve kinetics. Initial discharge capacities as high as approximately 1600 mAh g⁻¹ were obtained with this novel morphology¹³⁰. Composite anodes consisting of Fe₂O₃ nanodisks coupled with reduced graphene oxide layers were fabricated by a hydrothermal technique by Qu et al as anodes in Li-ion battery applications. These composite electrodes provided very good capacity retention and provide a capacity of 931 mAh g⁻¹ even after 50 cycles of operation. The authors attribute the significantly enhanced performance of the composite anode to nature of the composite anode, arguing that reduced graphene oxide has improved electrical conductivity as well as prevented the large volume expansion that usually occurs in the Fe₂O₃ system with intercalation. Fe₂O₃ thin films have been studied by Jiang et al⁸⁹. They have demonstrated a specific capacity of 385 mAh g⁻¹ after 200 cycles, retention in this case was 73 %⁸⁹. A sol-gel technique to fabricate Fe₂O₃ thin films were further studied by Brezesinski et al. The thin films provided high porosities and surface areas (190 m²cm⁻³) up to 600 °C. A maximum first cycle discharge capacity of 185 mAh g⁻¹ were obtained at 1 C discharge capacities with an intercalation voltage plateau at 1.8 V. Jian et al. used Fe₂O₃ nanocrystals anchored on

graphene nanosheets as anode materials and have obtained specific capacities as high as 400 mAh g⁻¹ and no fading over 200 cycles of operation¹³¹.

α -Fe₂O₃ nanoplatelets and nanoneedles have been studied as anodes in aqueous media and they have provided significantly high maximum discharge capacities of 330 mAh g⁻¹ and 468 mAh g⁻¹ respectively. The authors have pointed out that the discharge capacities are based on their high surface areas and hydrolysis was the mainly responsible for capacity fading¹³². Zhang et al. has studied α -Fe₂O₃/graphene nanocomposites, fabricated by solvothermal technique as aqueous supercapacitor anodes and very high capacitances of about 615 F g⁻¹ at current densities of 100 mA g⁻¹ have been obtained¹³³. The high capacitances have been attributed to their large surface areas (215.3 m²g⁻¹)¹³³.

However, drawbacks of Fe₂O₃ are several; structural degradation due to significant volume change and consequent low capacity retention especially for Na-ion batteries, poor kinetics and insufficient electrical conductivity. Also an exhaustive study of Fe₂O₃ anode systems for in aqueous environment is sparse⁹¹. Consequently, it is imperative that detailed analysis of the hematite system be performed so as to understand its reaction mechanism and improve its performance as an aqueous Na-ion battery anode.

5.2. Project rationale and outline

It is to be kept in mind that structural stability of the anode is just as important as enhanced electrochemical kinetics for the smooth performance of the cell. Improved structural stability is essential in providing longevity which is imperative. This project focuses on analyzing the effect of modifying the crystal structure of α -Fe₂O₃ (named Fe₂O₃ from here on) and understanding the structure-property relationship and the effect it has on electrochemical performance overall. Modification of the crystal structure can

be achieved by several techniques, the method used here is to dope the hematite structure with a different metal atoms. Analysis of improvement of structural stability and of the Fe_2O_3 crystal structure due to doping of foreign atoms will be the central scope of this research.

The Fe_2O_3 crystal is doped with two different types of atoms in this case: the large sized transition metal ion Zn^{2+} and the smaller sized isovalent Al^{3+} . Progressively increasing doping concentrations are used corresponding to the empirical formula $\text{Fe}_{2-x}\text{Zn}_x\text{O}_3$ and $\text{Fe}_{2-x}\text{Al}_x\text{O}_3$ ($x = 0.02, 0.04, 0.08$ and 0.12). Detailed structural and electrochemical characterization is then performed to study the effect of the doping on the structural characteristics of the modified Fe_2O_3 and its cycling performance and durability.

5.3 Anode fabrication

The two sets of Fe_2O_3 based anodes; $\text{Fe}_{2-x}\text{Zn}_x\text{O}_3$ and $\text{Fe}_{2-x}\text{Al}_x\text{O}_3$ are both prepared by solid state reactions from their precursors. For the Zn doped sample, the precursor used was ZnO whereas for the Al doped sample, aluminum acetate (and also aluminum nitrate for comparison) was used. Stoichiometric quantities of the precursors and Fe_2O_3 were thoroughly ground together and then heated in a muffle furnace at $800\text{ }^\circ\text{C}$ for 8 hours in a muffle furnace.

5.4 Structural characterization

Complete structural analysis results of the two different anode systems are provided below.

5.4.1 XRD spectra analysis

XRD spectra analysis of the $\text{Fe}_{2-x}\text{Zn}_x\text{O}_3$ and the $\text{Fe}_{2-x}\text{Al}_x\text{O}_3$ samples were done by the Bruker D8TM diffractometer. The spectral stack of the $\text{Fe}_{2-x}\text{Zn}_x\text{O}_3$ samples are provided in figure 26.

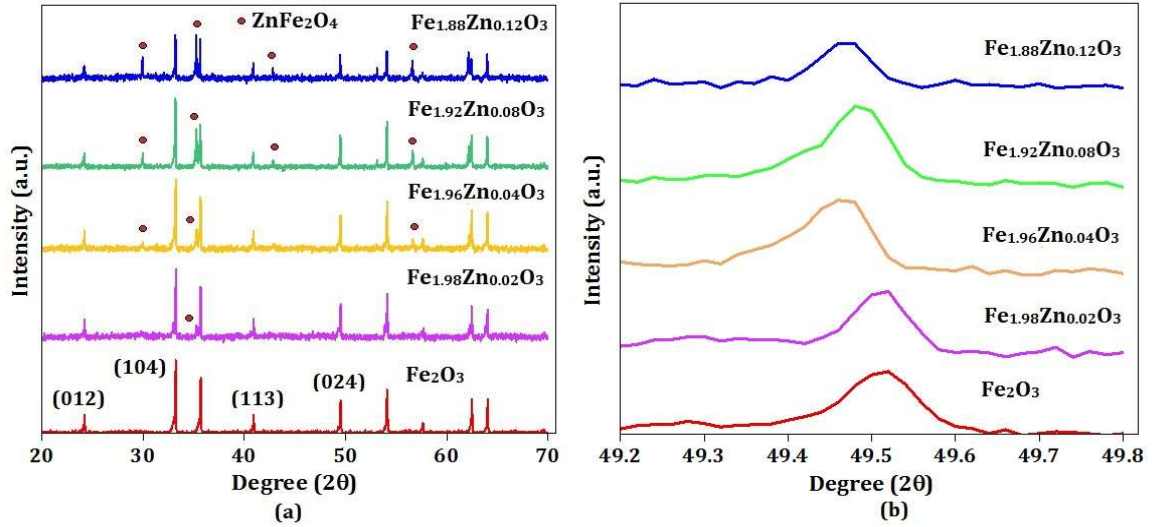


Figure 26. XRD spectra stack of pure Fe_2O_3 along with all the Zn doped samples. (a) demonstrates the entire spectra and (b) a more detailed look at the (024) peak.

In figure 26(a), the XRD spectra at the base of the stack is of the as obtained Fe_2O_3 sample and the ones on the top are the samples with progressively more Zn doped as labeled. Some important representative peaks viz. (012), (104), (113) and the (024) peaks have been labeled from the ICDD database (01-0076-4579 and 00-003-0800). The peaks match well with the database and also the existing literature¹³⁴. However, increasing Zn content in the as-obtained Fe_2O_3 samples also indicate the gradual appearance of other peaks (marked with red dots) which have been indexed to the spinel cubic ZnFe_2O_4 phase (PDF cards 00-001-1108 and 00-022-1012). The amount of the spinel phase gradually

increase with increasing Zn content as is noticed in the greater number of ZnFe₂O₄ peaks in the Fe_{1.88}Zn_{0.12}O₃ sample than the Fe_{1.98}Zn_{0.02}O₃ sample. However, no other impurity peaks, such as ZnO are noticed in the XRD spectra. A similar result has been reported by Nikolic et al¹³⁵.

Figure 26 (b) demonstrates the (024) peak in greater detail. As can be observed from the figure, there is a slight leftward shift in the peak from 49.52 degrees in the pure Fe₂O₃ sample (in red at the bottom) to 49.48 degrees for the Fe_{1.88}Zn_{0.12}O₃ sample (in blue at the top) indicating accommodating the Zn²⁺ ion causes a lattice expansion, albeit slightly.

Table 2 below gives an indication of the lattice structure variation (increase) with progressive Zn²⁺ doping.

Table 2

Comparison of lattice parameters and volumes of the Fe_{2-x}Zn_xO₃ systems

Sample	Parent Fe ₂ O ₃ structure		Lattice volume (Å ³)	ZnFe ₂ O ₄ lattice parameter (a=b=c) (Å)
	a (Å)	c (Å)		
Fe ₂ O ₃	5.0249	13.7211	300.02	
Fe _{1.98} Zn _{0.02} O ₃	5.0281	13.7023	299.99	
Fe _{1.96} Zn _{0.04} O ₃	5.0281	13.7194	300.37	
Fe _{1.92} Zn _{0.08} O ₃	5.0299	13.7257	300.71	
Fe _{1.88} Zn _{0.12} O ₃	5.0327	13.7334	301.22	8.4290

As noted, the increase in lattice parameters are very small (0.15 % for ‘a’ dimension and 0.08 % in ‘c’ dimension and a ~0.4% lattice volume increase) and therefore it can be argued that there is relatively low lattice strain in accommodating the Zn^{2+} ion in the Fe_2O_3 lattice. Also these results match up well with existing ICDD database values (PDF cards 00-006-0502 and 00-001-1108). It can be subsequently inferred that these results indicate that the doping of Zn has a two-fold effect on the hematite structure; reasonably good incorporation in to the rhombohedral Fe_2O_3 crystal lattice as well as the formation of a distinct new phase i.e. the spinel cubic $ZnFe_2O_4$.

XRD spectra stack of the $Fe_{2-x}Al_xO_3$ samples are provided in figure 27 below. The color coding used here is similar to the Zn doped samples for similar dopant concentrations.

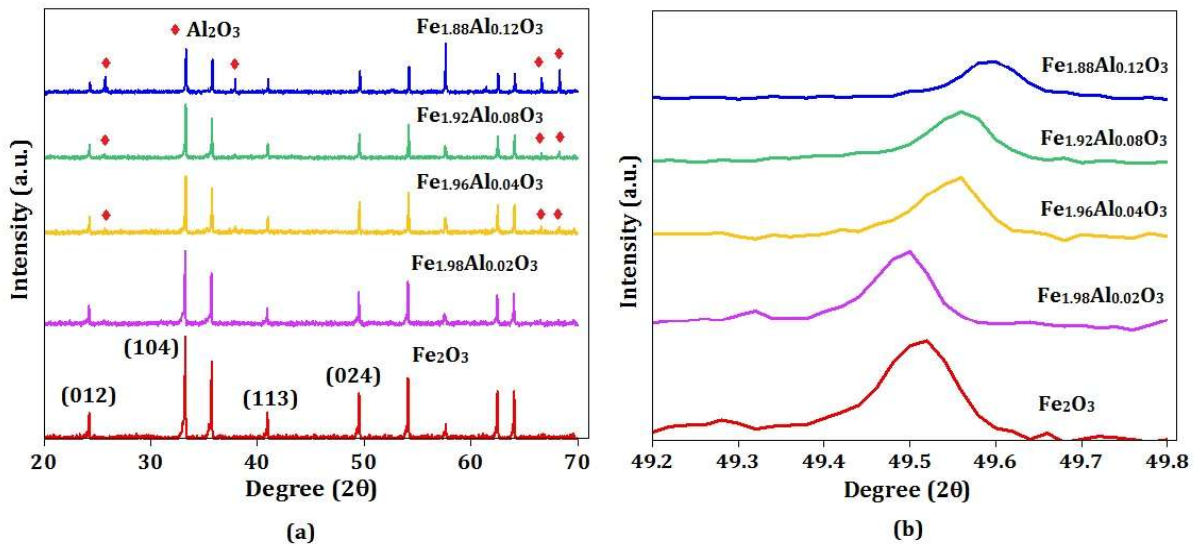


Figure 27. XRD spectra stack of pure Fe_2O_3 along with all the Al doped samples. (a) demonstrates the entire spectra and (b) a more detailed look at the (024) peak.

The XRD spectra, shown in figure 27(a) demonstrates that the overall peak positions are maintained for the Fe_2O_3 sample with doping indicating incorporation of Al^{3+} ions in the

hematite lattice. However, certain other distinctly important observations can be drawn. Firstly, as can be seen from the peaks marked with a red star, there is the increasing appearance of Al_2O_3 peaks with increasing Al^{3+} doping. The Al_2O_3 peaks have been indexed from the ICDD database (PDF card 00-013-0915). Unlike in the Zn doped case previously, no spinel formation is noticed here. Figure 27(b) indicates the (024) peak in greater detail. It is noticed that there is a noticeable peak shift towards higher angles indicating a contraction in the hematite lattice due to incorporation of the comparatively smaller Al^{3+} ion in the hematite structure. A similar reduction in lattice parameter due to Al ion incorporation has been reported by Kleiman-Shwarsstein and Schwertmann^{136,137}. Also, as can be seen from the figure, the peaks undergo some broadening and reduction in intensity, indicating loss of crystallinity and increasing lattice stress with progressive Al incorporation, which can be due to shorter Al-O bond lengths ($\approx 1.97 \text{ \AA}$) than the normal Fe-O bond lengths ($\approx 2.09 \text{ \AA}$). Lattice parameter variation of the $\text{Fe}_{2-x}\text{Al}_x\text{O}_3$ samples are provided in the table below.

Table 3

Comparison of lattice parameters of the $\text{Fe}_{2-x}\text{Al}_x\text{O}_3$ systems.

Sample	Parent Fe_2O_3 structure		Volume (\AA^3)
	a (\AA)	c (\AA)	
Fe_2O_3	5.0249	13.7211	300.02
$\text{Fe}_{1.98}\text{Al}_{0.02}\text{O}_3$	5.0281	13.7287	300.57
$\text{Fe}_{1.96}\text{Al}_{0.04}\text{O}_3$	5.0191	13.6920	298.70
$\text{Fe}_{1.92}\text{Al}_{0.08}\text{O}_3$	5.0191	13.7044	298.97
$\text{Fe}_{1.88}\text{Al}_{0.12}\text{O}_3$	5.0136	13.6882	297.96

The table indicates a net reduction in the ‘a’ and ‘c’ parameters by 0.22 % and 0.23 % respectively and a net lattice volume decrease by ~0.68 %. Consequently, as discussed above, the net effect of the isovalent Al^{3+} ion doping in the Fe_2O_3 lattice is to produce a small lattice volume shrinkage, induce stress and crystallinity loss and formation of impurity Al_2O_3 phase.

5.4.2 XPS analysis

XPS analysis was performed to further confirm the chemical signature of pure as well as the Zn and Al doped hematite samples ($\text{Fe}_{1.92}\text{Zn}_{0.08}\text{O}_3$ and $\text{Fe}_{1.92}\text{Al}_{0.08}\text{O}_3$ are chosen as representatives in each case). The full spectra XPS analysis of the three samples is provided in the figure 28.

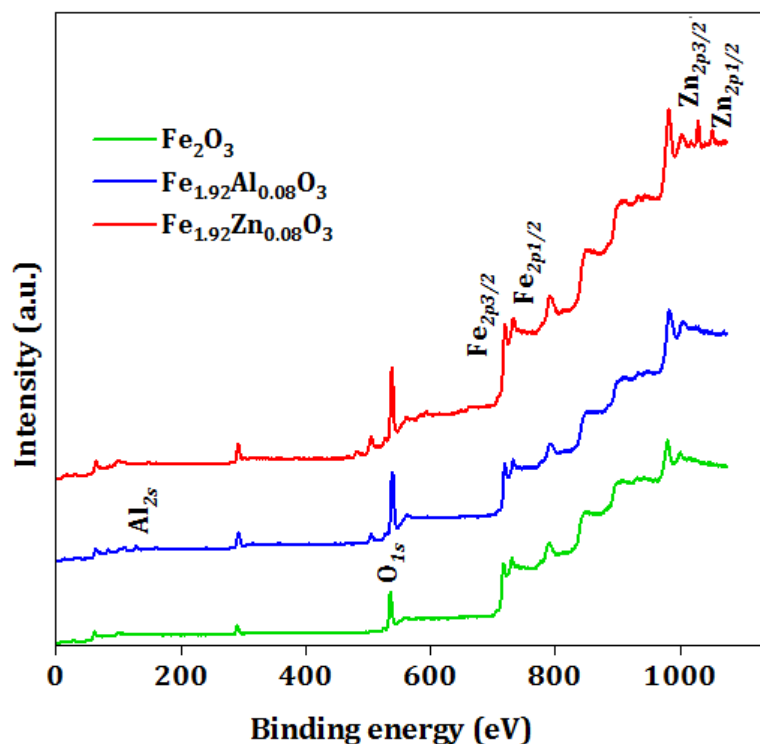


Figure 28. “Full survey” XPS spectra of the Fe_2O_3 (in green), $\text{Fe}_{1.92}\text{Al}_{0.08}\text{O}_3$ (in blue) and $\text{Fe}_{1.92}\text{Zn}_{0.08}\text{O}_3$ (in red).

The XPS spectra of the doped samples also match overall with the pure Fe_2O_3 samples. From this “full survey spectra”, the O_{1s} , $\text{Fe}_{2p_{1/2}}$ and $\text{Fe}_{2p_{3/2}}$, $\text{Zn}_{2p_{3/2}}$ and $\text{Zn}_{2p_{1/2}}$ and Al 2s peaks can be noticed as labeled. For greater clarity, the individual peaks have been isolated and provided in the figure below for greater clarity.

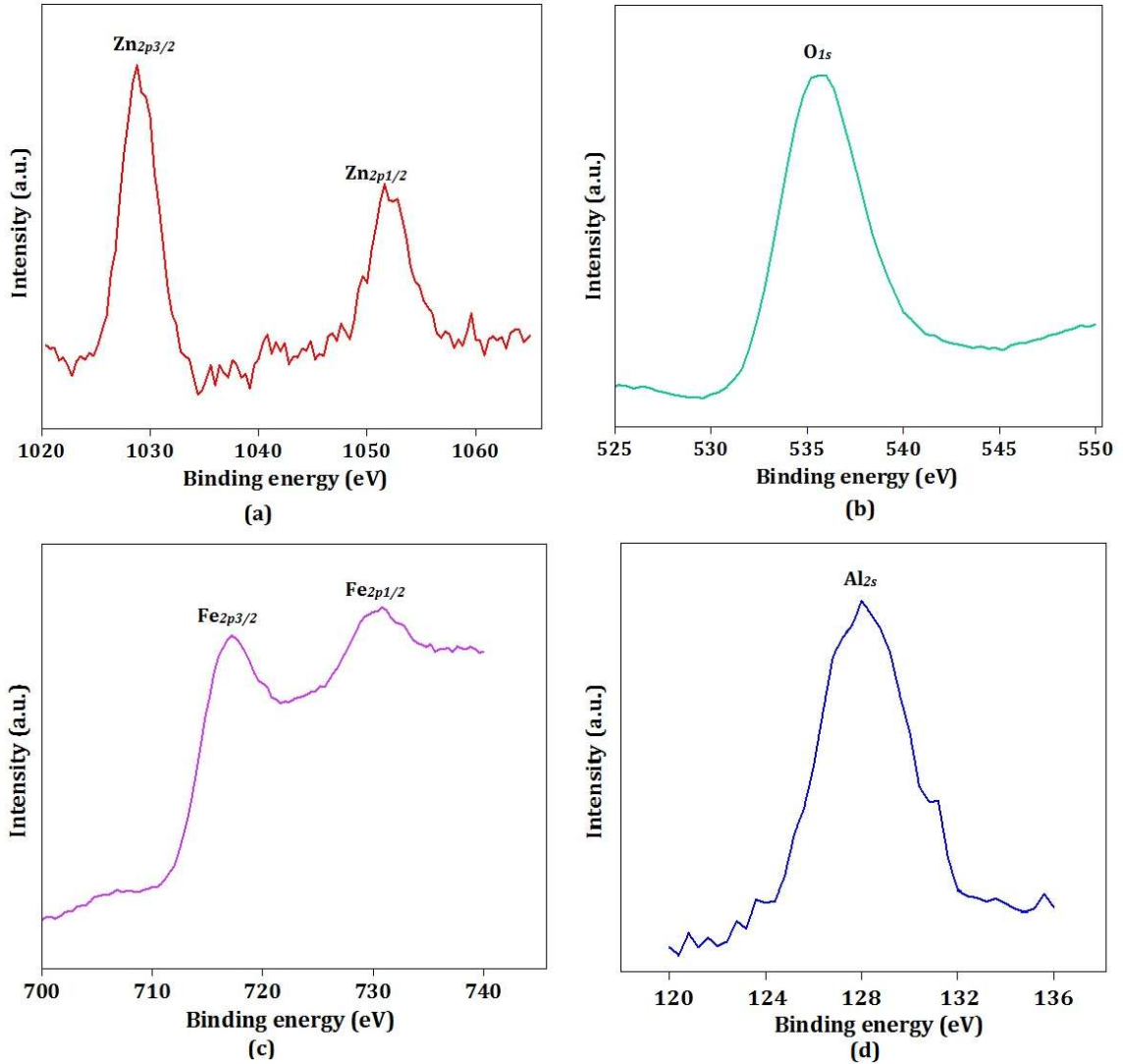


Figure 29. (a), (b), (c) and (d) represent the individual XPS peaks demonstrating the Zn, O, Fe and Al characteristic signatures.

From figure 29(a), for the Zn doped sample, the $Zn_{2p_{3/2}}$ and $Zn_{2p_{1/2}}$ peaks are noticed at 1029.6 eV and 1052.8 eV. These Zn peaks correspond well with the bonding states for Zn^{2+} in the $ZnFe_2O_4$ spinel. Similarly in the Al doped sample in figure 19(b), the presence of the Al_{2s} peak at 128.4 eV corresponds to the state of the Al^{3+} ion in Al_2O_3 . Apart from this, the characteristic O_{1s} peak is found at 535.2 eV and the $Fe_{2p_{1/2}}$ and

$Fe_{2p_{3/2}}$ peaks are located at 731.2 eV and 718 eV as seen in figures 19(c) and 19(d). All these results match up well with the existing literature^{138,139}. Therefore the XPS results provide information regarding the bonding states of the various atoms and also serve to conclusively confirm the findings of the XRD.

5.4.3 Raman spectra analysis

Raman spectroscopy was performed by an InVia Renishaw Raman microscope using a red HeNe laser of wavelength 632.8 nm. The Raman spectra data for the $Fe_{2-x}Zn_xO_3$ and the $Fe_{2-x}Al_xO_3$ systems are given below in figures 30(a) and (b).

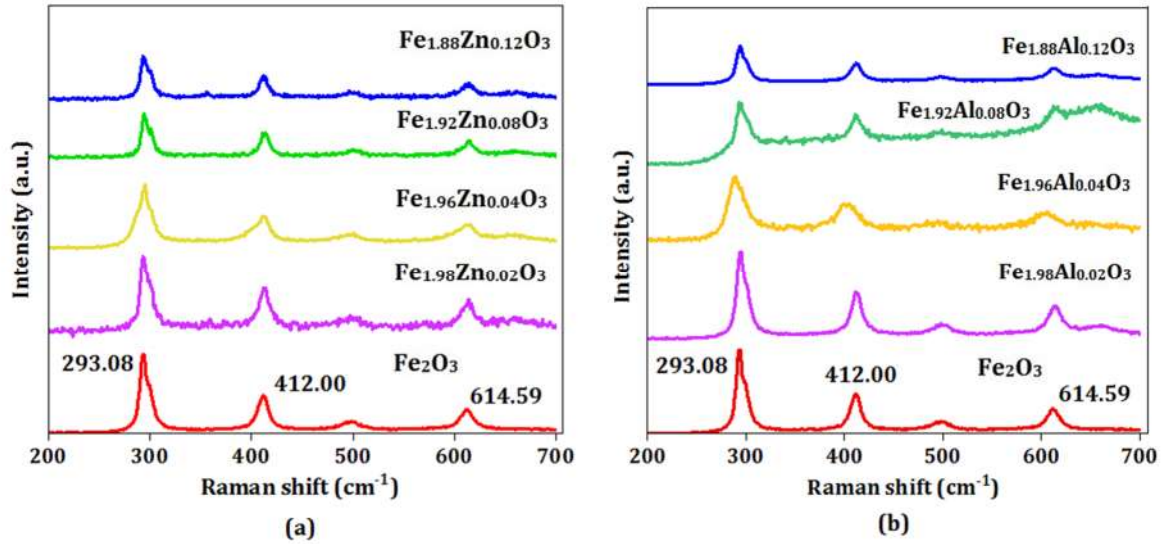


Figure 30. Raman spectra stack of pure Fe_2O_3 along with all the Zn and Al doped samples. (a) demonstrates the Raman spectra of $F_{2-x}Zn_xO_3$ samples and (b) Raman spectra of the $Fe_{2-x}Al_xO_3$ samples.

The Raman spectra peaks of the Fe_2O_3 correspond to characteristic phonon mode vibrations. The prominent Raman shift peaks labeled i.e. 293.08 cm^{-1} , 412.00 cm^{-1} and the 614.59 cm^{-1} in both figures correspond to the $E_g(2)$, $E_g(4)$ and A_{1g} phonon vibration

modes respectively¹⁴⁰. It is also seen that some peak broadening and shift does take place, indicating lattice stress due to accommodating the dopant atoms. These effects are more pronounced in the case of the Al doped samples than the Zn doped ones corroborating to the evidence already obtained from the XRD data.

5.4.4 SEM imaging

SEM imaging of the pure, Zn doped and Al doped samples was performed by a TESCAN™ SEM. The SEM images of the pure Fe₂O₃ samples are provided in figure 31 below.

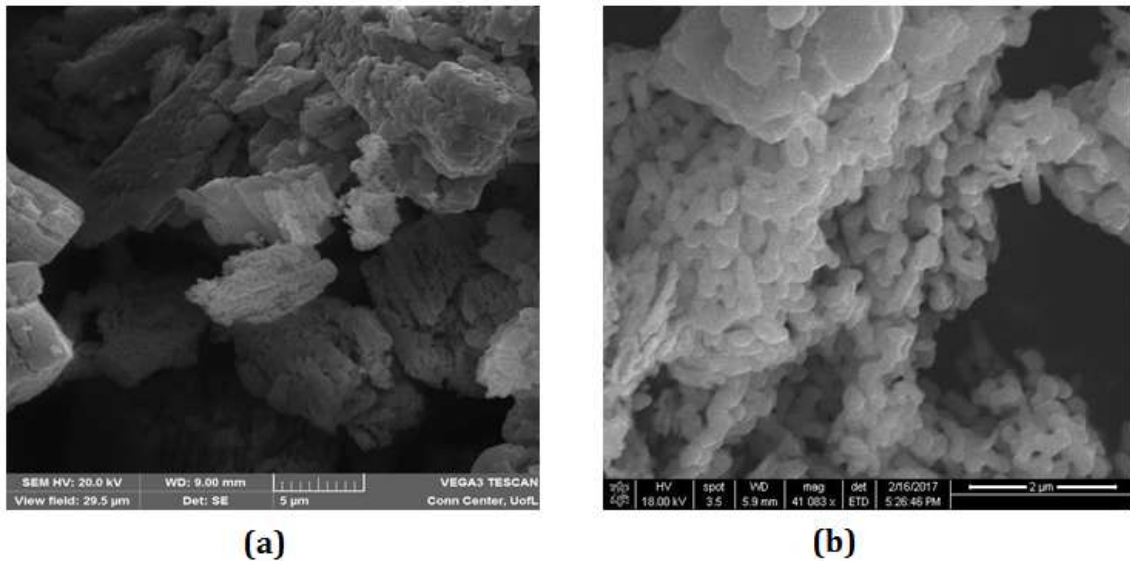


Figure 31. SEM images of the pure Fe₂O₃ sample at (a) 5 μm and (b) 2 μm resolution.

The images show the non-doped Fe₂O₃ particles exist as rather large sized chunks superficially. On closer inspection (at 2 μm), it is seen that these clumps are actually made up of much smaller sized particles. The particles represent a beadlike microstructure and particle sizes seem to be well below 1 μm.

SEM images of the $\text{Fe}_{1.98}\text{Zn}_{0.02}\text{O}_3$, $\text{Fe}_{1.96}\text{Zn}_{0.04}\text{O}_3$, $\text{Fe}_{1.92}\text{Zn}_{0.08}\text{O}_3$, $\text{Fe}_{1.88}\text{Zn}_{0.12}\text{O}_3$ samples are shown below in the figures 32(a) – (d) respectively.

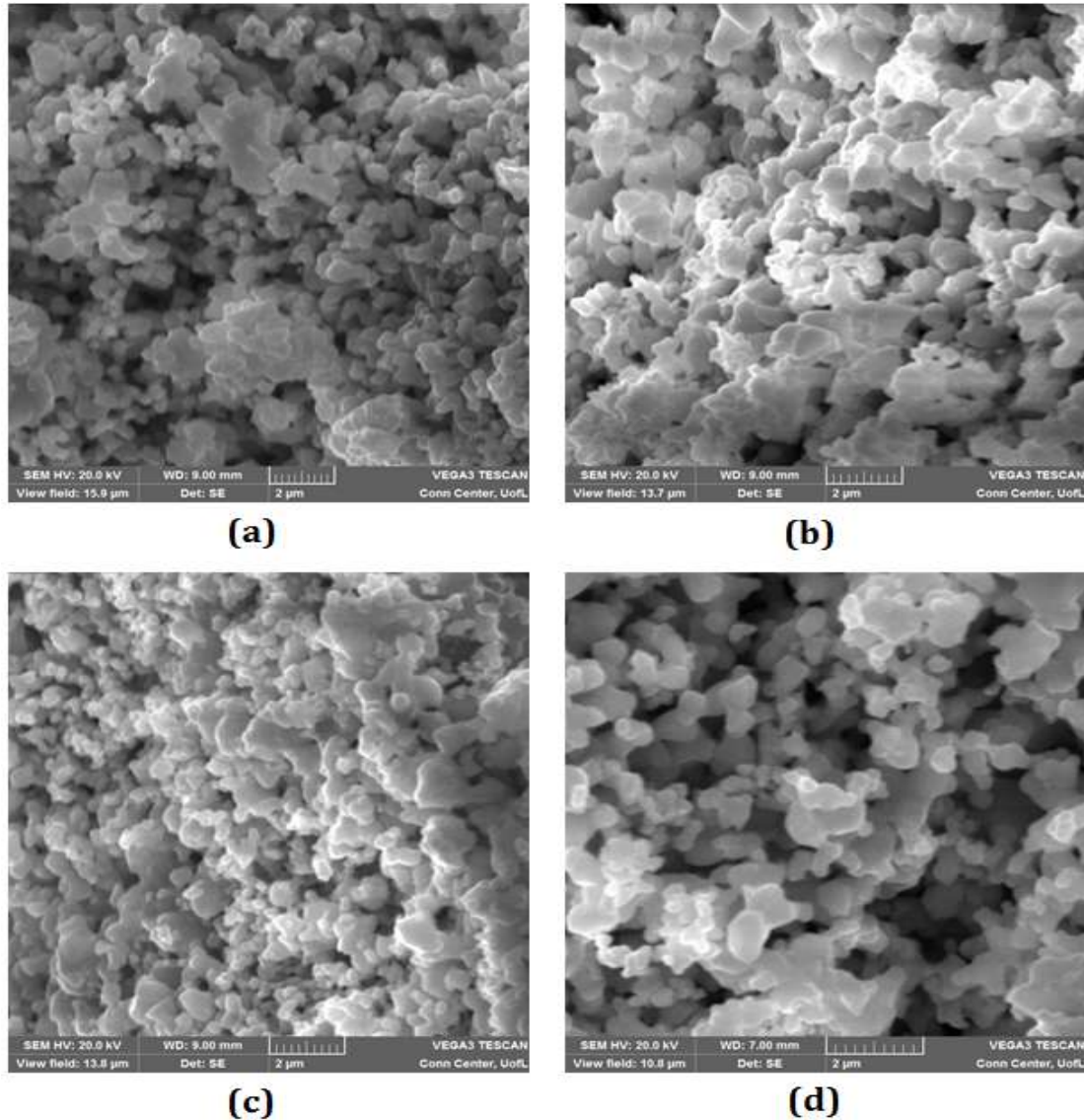


Figure 32. SEM images of (a) $\text{Fe}_{1.98}\text{Zn}_{0.02}\text{O}_3$ (b) $\text{Fe}_{1.96}\text{Zn}_{0.04}\text{O}_3$ (c) $\text{Fe}_{1.92}\text{Zn}_{0.08}\text{O}_3$ and (d) $\text{Fe}_{1.88}\text{Zn}_{0.12}\text{O}_3$ samples.

The images indicate that the same bead like morphology has been maintained and exists uniformly throughout the microstructure. However, as it is apparent, there is an increase

in the size of the particles. This size increase can be attributed to the sintering/solid state reaction process.

Likewise, SEM images of the $\text{Fe}_{1.98}\text{Zn}_{0.02}\text{O}_3$, $\text{Fe}_{1.96}\text{Al}_{0.04}\text{O}_3$, $\text{Fe}_{1.92}\text{Al}_{0.08}\text{O}_3$, $\text{Fe}_{1.88}\text{Al}_{0.12}\text{O}_3$ samples are provided in figure 33.

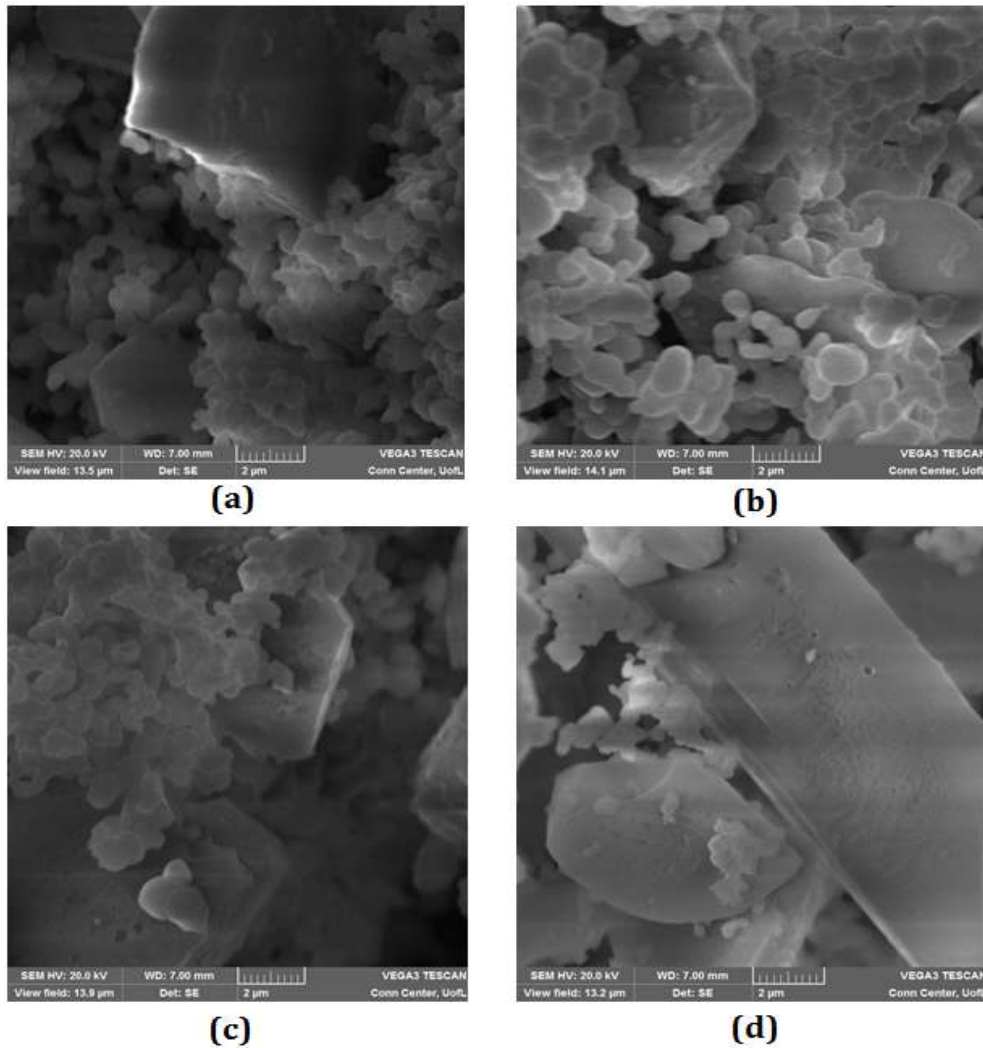


Figure 33. SEM images of (a) $\text{Fe}_{1.98}\text{Al}_{0.02}\text{O}_3$ (b) $\text{Fe}_{1.96}\text{Al}_{0.04}\text{O}_3$ (c) $\text{Fe}_{1.92}\text{Al}_{0.08}\text{O}_3$ and (d) $\text{Fe}_{1.88}\text{Al}_{0.12}\text{O}_3$ samples.

SEM images in this case also demonstrate the usual bead like microstructure of the Al doped Fe_2O_3 particles. Like the Zn doped case, there is similar size increase of the bead

like morphology, again which can be attributed to the sintering process. However, also clearly discernible, are rather large sized irregular particles. These particles can be considered to be the Al_2O_3 particles, which have been characterized in the XRD spectra as well. Therefore the SEM images provide important information related to the similarity and distinct differences between the Zn and Al doped particles.

5.4.5 Particle size and BET analysis

Particle size and BET surface area analysis results are as provided in the figure below.

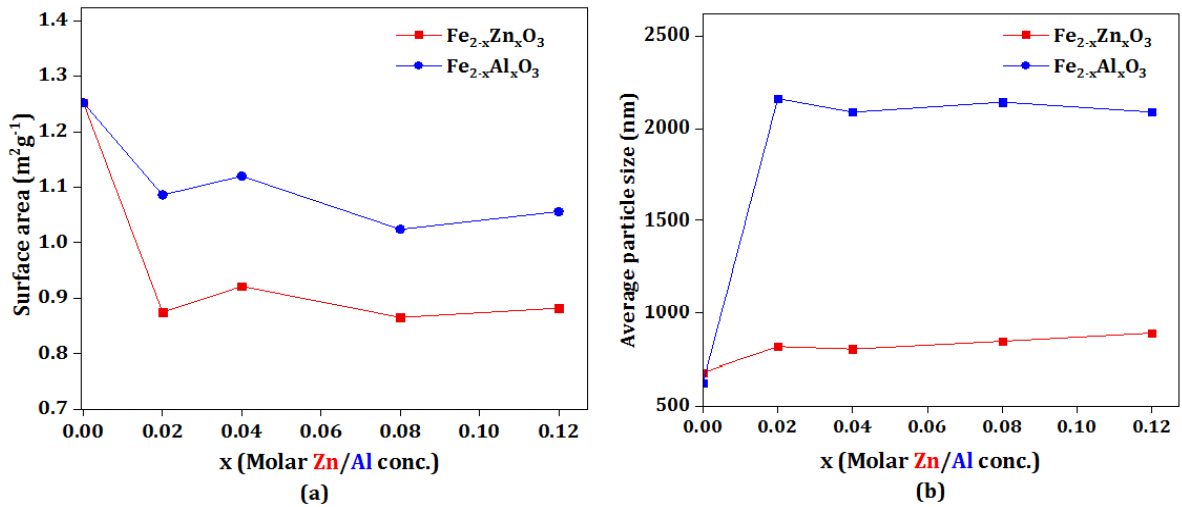


Figure 34. (a) BET surface area trends of the Zn and Al doped samples. (b) Average particle size trends of the Zn and Al doped samples.

As can be seen from the figure 34(a), the BET results show that the Zn doped samples exhibit higher surface area than the Al doped sample, but only slightly. This discrepancy may be due to the large sized Al_2O_3 particles which lower the overall surface area for the Al doped samples.

Particle size results indicate that the $\text{Fe}_{2-x}\text{Al}_x\text{O}_3$ samples exhibit far larger average particle size than their Zn doped counterparts. These results seem to be in good agreement with

the SEM images. Presence of the large sized Al_2O_3 particles seem to skew the particle size higher for the Al doped samples.

5.5. Cell assembly

Both the anode systems (Zn and Al doped) as well as the pure Fe_2O_3 are suspended in isopropanol and then drop casted on a carbon paper substrate. A Whitman glass fiber separator is used and the electrolyte used is 2 M Na_2SO_4 . CR 2032 coin cells are used for the purpose of electrochemical measurements. Current rates used are usually 1 C unless otherwise mentioned and the voltage window for charging and discharging is 0 V – 2 V and the voltages are for the full cell.

5.6. Electrochemical analysis

5.6.1 Cell cycling and stability

First discharge cycles for the Fe_2O_3 and two representative Zn doped ($\text{Fe}_{1.96}\text{Zn}_{0.04}\text{O}_3$ and $\text{Fe}_{1.88}\text{Zn}_{0.04}\text{O}_3$) samples and the stability graphs of the pure as well as all the Zn doped samples are provided in the figure below.

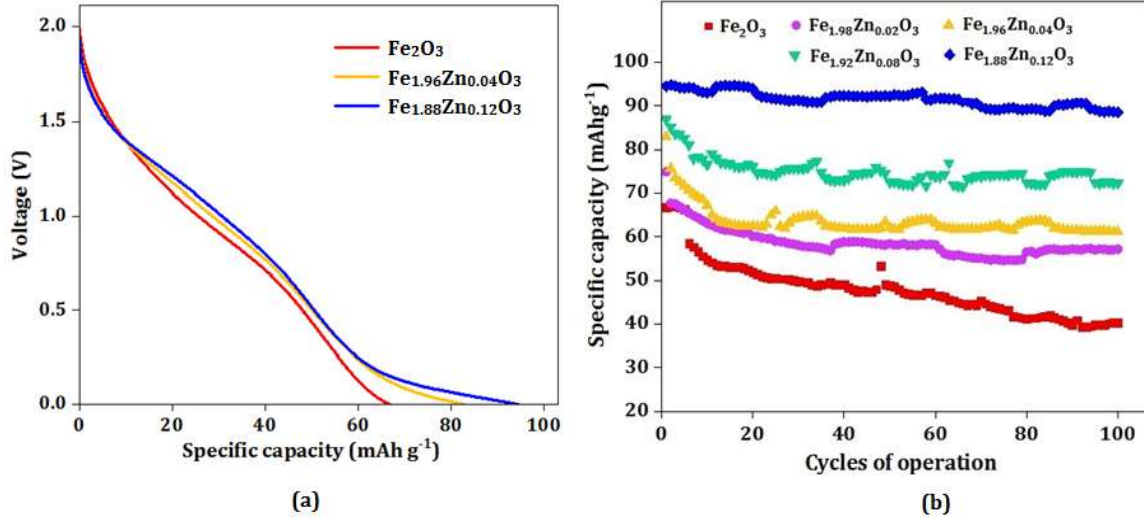


Figure 35. (a) Representation of the first cycle discharge curves for the Fe₂O₃ (in red), Fe_{1.96}Zn_{0.04}O₃ (in orange), Fe_{1.88}Zn_{0.12}O₃ (in blue) and (b) are the specific capacity retention plots of all the Zn doped samples.

As can be seen from figure 35(a), the discharge curves follow a similar trajectory. The maximum first cycle discharge capacity is provided by the Fe_{1.88}Zn_{0.12}O₃ sample, which is 94.41 mAh g⁻¹ and it shows a significant improvement (41.29 %) from the non-doped/pure Fe₂O₃ sample which demonstrates a maximum first cycle specific discharge capacity of 66.82 mAh g⁻¹. Also the 12 % Zn doped sample exhibits a noticeable plateau region especially at low voltages of ≈ 0.25 V, which is practically non-existent in the non-doped sample indicating the non-doped sample acts basically as a supercapacitor. The first cycle specific discharge capacity values also as seen from the cycling stability graphs indicate a steady increase with progressive Zn doping. The stability graphs, as plotted in figure 35(b) tell a similar story. An increase in discharge capacities along with a similar incremental and progressive increase in the capacity retention is noticed as well. Pure Fe₂O₃ demonstrates capacity retention of about 60.33 %, that of the Fe_{1.96}Zn_{0.04}O₃ is

76.35 % and finally the $\text{Fe}_{1.88}\text{Zn}_{0.12}\text{O}_3$ sample has specific capacity retention as high as 93.81 %. It can be inferred that the addition of Zn has had a positive influence on the Fe_2O_3 structure, as it has helped to improve starting capacities as well as enhance capacity retention. Presence of ZnFe_2O_4 , can also be considered to be beneficial as it has a high theoretical capacity and the system can be thought to behave as a “composite anode” where both improve the net result in conjunction.

Similarly the first cycle discharge curves for the pure Fe_2O_3 sample along with two corresponding representative Al doped samples ($\text{Fe}_{1.96}\text{Al}_{0.04}\text{O}_3$ and $\text{Fe}_{1.88}\text{Al}_{0.12}\text{O}_3$), have been provided in figure 36 below.

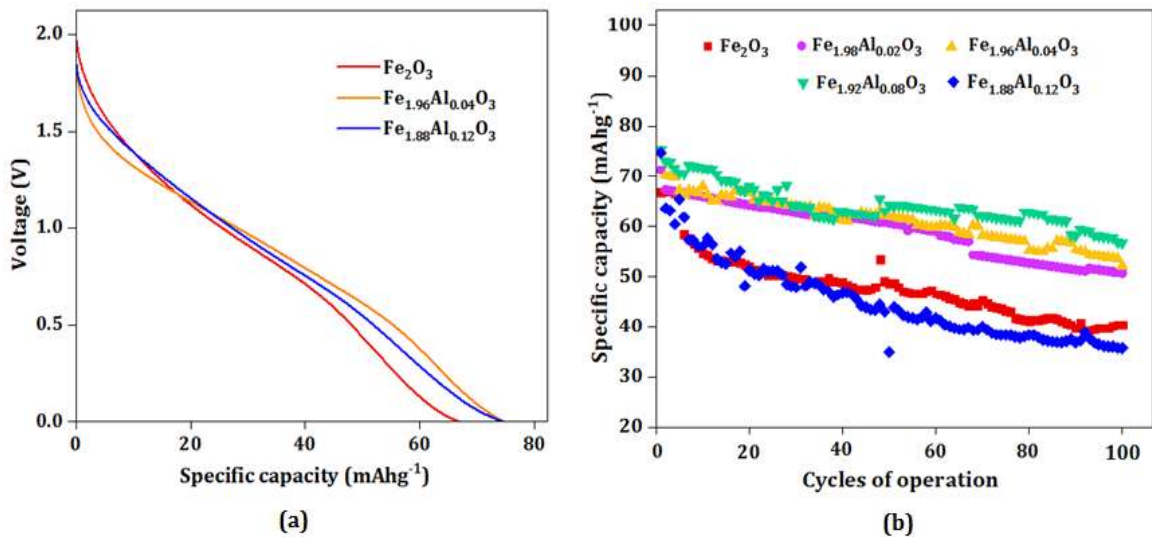


Figure 36. (a) Representation of the first cycle discharge curves for the Fe_2O_3 (in red), $\text{Fe}_{1.96}\text{Al}_{0.04}\text{O}_3$ (in orange), $\text{Fe}_{1.88}\text{Al}_{0.12}\text{O}_3$ (in blue) samples and (b) are the specific capacity retention plots of all the Al doped samples.

Here too, it is observed that the discharge curves have a similar trajectory to that of the Zn doped sample, even though the discharge plateaus are not as sharp. There is a small increase in first cycle discharge capacities (an 11 % increase from pure Fe_2O_3 to

$\text{Fe}_{1.88}\text{Al}_{0.12}\text{O}_3$). The capacity retention plots also demonstrate slightly improved values from the pure Fe_2O_3 sample (71.26 % retention for the $\text{Fe}_{1.98}\text{Al}_{0.02}\text{O}_3$ sample), indicating the positive effect of Al^{3+} is significantly less than the Zn^{2+} addition. However, the $\text{Fe}_{1.88}\text{Al}_{0.12}\text{O}_3$ sample actually suffers a rather drastic capacity drop, and is only able to retain 47.91 % of its initial discharge capacity. Therefore, the advantages derived by doping the Fe_2O_3 structure with Al^{3+} ions (a small improvement in initial capacities) is rapidly overshadowed (noticed as steep drops in capacity retention with increasing Al doping) due to formation of Al_2O_3 impurities and an already stressed lattice, both of which serve to rather weaken the parent hematite structure.

5.6.2. Capacity loss analysis

The analysis of the capacity loss and electrode degradation is performed analytically to understand the mechanism of electrode degradation as well as the stages of the reaction at which they take place. The results for these analysis are shown in the figure 37 below.

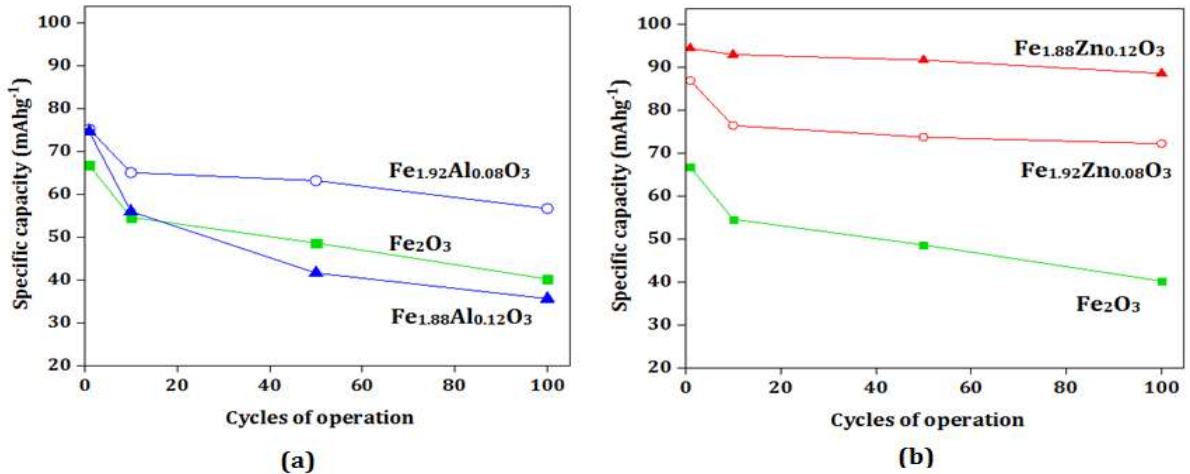


Figure 37. Indicating the capacity loss trend in greater detail for the (a) non-doped and the 8 % and 12 % Al doped samples respectively and (b) for the non-doped and the 8 % and 12 % doped Zn samples respectively.

Figure 37(a) indicates the capacity degradation of the Al doped systems considering the 8 % and 12 % doped systems (in blue sphere and triangle respectively) with the non-doped hematite (in green). The non-doped sample undergoes an initial capacity drop (18.16 % in the first 10 cycles) due to significant degradation of the Fe_2O_3 crystal lattice initially. It then drops further by 26.28 % over the next 90 (final drop) cycles. The 8 % Al doped sample shows a small improvement in retention properties (initial drop of 13.44 % followed by a final drop of 12.82 %). However, on addition of further Al^{3+} i.e. for the 12 % Al doped system, it is seen that the initial capacity drop (in the first 10 cycles) is relatively large, especially (24.87 % drop) followed by another 36.22 % drop over the next 90 cycles. This indicates addition of large quantities of Al^{3+} ions (12 %) is actually detrimental to the Fe_2O_3 lattice. On the other hand, for the 12 % doped Zn^{2+} sample, it is noticed that the initial drop is about only 1.53 % followed by a 4.73 % drop for the remaining 90 cycles. Therefore, the addition of Zn^{2+} and the consequent formation of ZnFe_2O_4 have successfully arrested the capacity drop, thereby indirectly indicating it has had a stabilizing effect on the Fe_2O_3 structure to a large extent.

5.7 Post cycling analysis

5.7.1 XRD spectra analysis

Post cycled XRD was performed on the 12 % doped Zn and Al samples to understand the nature of the anodic degradation. The results are provided in the figure below.

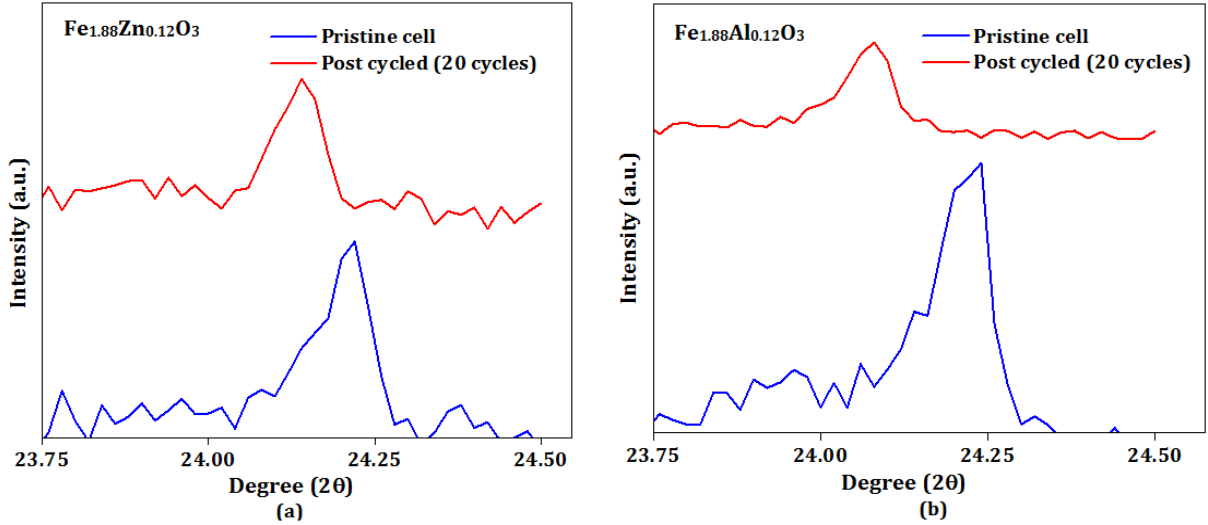


Figure 38. Pristine and post cycled XRD comparison of the (012) peak for the (a) 12 % Zn doped sample and (b) 12 % Al doped sample.

The comparison between the pristine and the post cycled 12 % Zn doped electrode, as seen in figure 38(a) shows a small peak shift to the left, which can be attributed as a result of interacting with Na^+ ions. Small amounts of peak broadening and reduction in intensity is also noticed indicating a slight loss in crystallinity. On the other hand, for the 12 % Al doped sample, a rather prominent peak broadening and reduction in peak intensity w.r.t to the pristine electrode is noticed. This can be attributed to the inherently larger stress induced in the Al doped samples itself as is evident from figure 27, larger volume expansion for the Al doped sample than the Zn doped one suffered during the cycling process and unequal expansion of the non-uniform Al_2O_3 particles which weaken the overall sample.. Therefore Zn doping has been able to improve the durability of the sample, however, large quantities of Al doping (12 % in this case) has resulted in a weakening of the lattice, which suffers significantly more degradation.

5.7.2 Impedance analysis

Impedance analysis for the pristine and the post cycled cells of the non-doped and 12 % Al and Zn doped samples respectively and the results are as provided below.

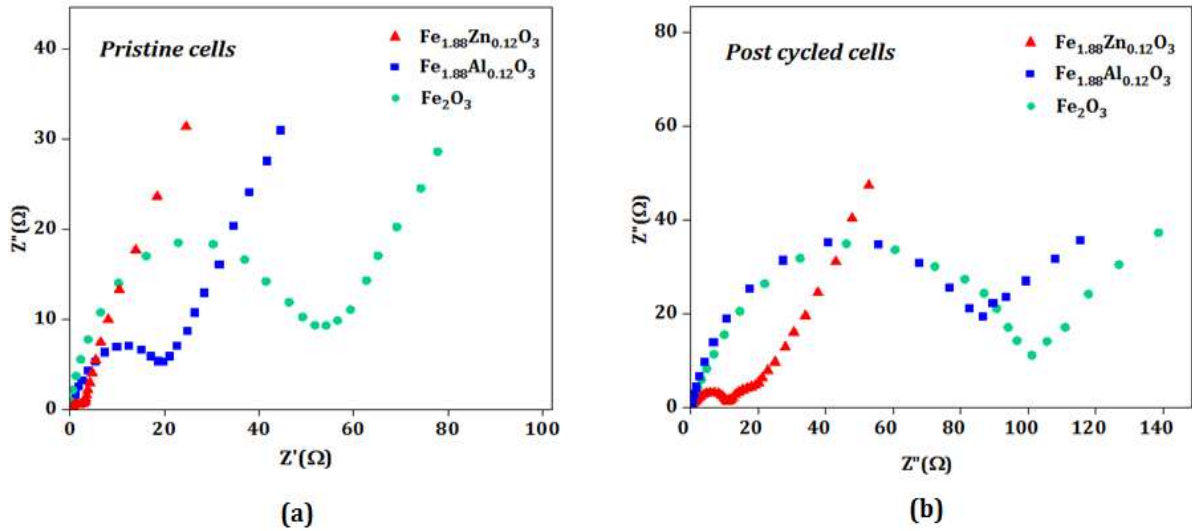


Figure 39. Pristine and post cycled impedance spectra of non-doped and 12 % Al and Zn doped samples respectively.

As can be seen from both figures 39(a) and (b), there is a significant increase in the radii of the semicircles of all the samples, post cell cycling indicating an increase in the electrode-electrolyte resistance. However, this increase is rather large for the non-doped sample which signifies that sample undergoes significant activity loss due to structural degradation associated with large volume change (capacity retention of only 60.33 %). On the other hand, the 12 % Zn doped sample provides the least increase thereby indicating that Zn doping has been beneficial and it has lost the least electrochemical activity (93.81 % capacity retention). However, for the 12 % Al doped hematite sample, it is observed that the impedance increase is almost as large as the non-doped sample

indicating it suffers considerable loss of active electrochemical sites (47.91 % capacity retention).

5.7.3. Cyclic voltammetry analysis

CV analysis was performed on the pristine (in blue) and the post cycled (in red) cells at a scan rate of 1 mV s^{-1} between the cut off voltages of 0 – 2 V and the results of the $\text{Fe}_{1.88}\text{Zn}_{0.12}\text{O}_3$ and the $\text{Fe}_{1.88}\text{Al}_{0.12}\text{O}_3$ cells are shown in the figures below as representative.

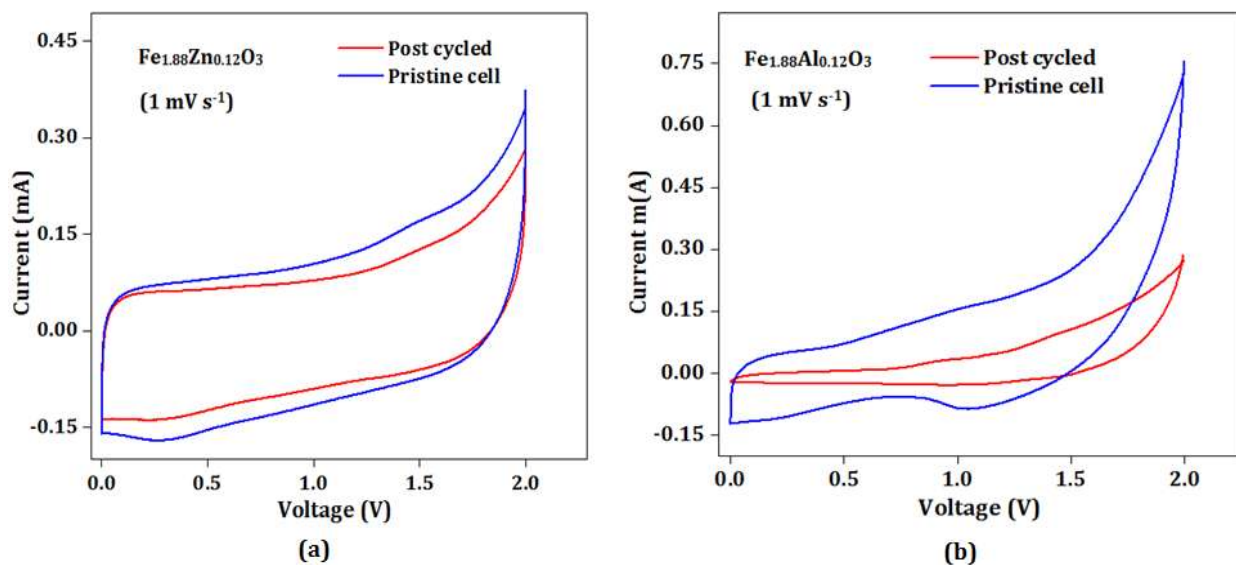


Figure 40. CV analysis of (a) pristine and post cycled cell for the 12 % Zn doped sample and (b) pristine and post cycled cell for the 12 % Al doped sample respectively.

Figure (a) shows the CV curves of the pristine and post cycled $\text{Fe}_{1.88}\text{Zn}_{0.12}\text{O}_3$ cell. As can be noticed, there is very little change in the shape of the post cycled curve and it almost matches up well with the pristine CV curve. However, from figure (b) it is noticed that the curvature of the CV graph of the post cycled $\text{Fe}_{1.88}\text{Al}_{0.12}\text{O}_3$ cell undergoes significant reduction in area. These results, therefore, indicate that Al doped sample undergoes considerably more loss in electrochemical activity and electrode degradation than the Zn

doped sample. Phase separation of large sized Al_2O_3 particles towards the grain boundaries and preventing an easy route for electrons can also be another reason for the poor electrical properties of the Al doped samples¹⁴¹. These results confirm those obtained from the post cycled XRD analysis and impedance spectra obtained previously, indicating that addition of Al more than 8 % results in greater structural degradation and consequently weakened electrochemical performance with progressive cell cycling.

5.8 Conclusion

The project was a study on structural stability of hematite anodes and the role that dopant atoms have played in that. Tailoring the lattice and analyzing the structure-property relation and how they affect the electrochemical performance have been studied in considerable detail. Results indicate a positive and negative effect of two different types of atoms; Zn and Al respectively. While the Zn atom goes on to improve the overall properties of the Fe_2O_3 system (resulting in improving the capacity and enhancing retention), Al doping does provide a small improvement in initial capacity. However large quantities of Al doping ultimately leads to weakening of the Fe_2O_3 structure. Post cycled cell analysis provides insights to the mechanism of structural failure that predominates in each of the different cases. This project also establishes the important role crystallographic structure plays in providing efficient electrochemical performance.

CHAPTER 6

THE TiO₂ - PRUSSIAN BLUE SYSTEM

6.1 Background of TiO₂ anode systems

TiO₂ systems have been studied as anodes, especially in Li-ion batteries because of their large theoretical capacity and fast diffusion kinetics. Li et al have studied mesoporous anatase TiO₂ coupled with graphene sheets and have obtained a first cycle discharge capacity of 332 mAh g⁻¹ and have attributed their enhanced kinetics to improvement in surface area as a result of graphene sheet addition¹⁴². Mesoporous TiO₂ nanospheres coated with carbon have also been studied by Cao et al¹⁴³. The authors demonstrate very good cycling performance and a specific capacity of 96 mAh g⁻¹ at a very high rate of 100 C. The enhanced properties of the nanospheres are due to the electrochemical and structural stability of the spheres, as suggested by the authors¹⁴³. Carbon coated TiO₂ microspheres have been fabricated by Oh and coworkers as anode materials in Na-ion batteries by a hydrothermal technique¹⁴⁴. At 1 C rate, a maximum discharge capacity of 149 mAh g⁻¹ was obtained and also demonstrated 100 capacity retention up to 50 cycles of operation¹⁴⁴. Nb doped TiO₂ has been used as an anode in Na-ion batteries by Usui et al¹⁴⁵. They fabricated the doped rutile samples by using a sol-gel process using hydrochloric acid and titanium tetraisopropoxide. The best performance was obtained from the Ti_{0.94}Nb_{0.06}O₂ sample, providing a capacity of 150 mAh g⁻¹ in the 50th cycle of operation¹⁴⁵.

6.2 Rationale and objectives

This is a brief which is project is devoted to the study and analysis of TiO_2 and mixed titanate ($\text{Na}_2\text{Ti}_3\text{O}_7$) as anodes for Na-ion batteries. Both TiO_2 and $\text{Na}_2\text{Ti}_3\text{O}_7$ have demonstrated considerable advantages as anodes for Na-ion batteries^{146,147}. Therefore, this project is aimed at studying the behavior of both anode materials in aqueous and organic electrolyte environments versus a Prussian blue cathode. A significant study of these anodes in aqueous media has previously not been presented; this project aims to fill the gap.

*The entire research presented in this project (Chapter 6) has been published by the author of this dissertation in **Journal of Power Sources** 286 (2015) pp. 276 – 289.*

6.3 Materials

The materials in use and their fabrication techniques can be elaborated as follows:

6.3.1. Anode

Four different types of anode materials were selected for analysis as follows:

- (i) *Amorphous TiO_2* (rutile phase), used as-obtained from Sigma Aldrich.
- (ii) *Crystalline TiO_2* (anatase phase), also used as obtained from Sigma Aldrich (99% metals basis) and called as “pristine TiO_2 ”.
- (iii) *TiO_2 -HT (heat treated)*, obtained by heat treating the pristine TiO_2 at a temperature of 150 °C for 12 hours.
- (iv) *Sodium titanate ($\text{Na}_2\text{Ti}_3\text{O}_7$)*, the precursors for its fabrication were TiO_2 and NaOH pellets. Stoichiometric quantities of the precursors were intimately hand-ground and then ball-milled in a SPEX© milling machine for about 5 hours to obtain the mixture. Then this as-milled mixture was heated in a muffle furnace at 750 °C for 20 hours to obtain the $\text{Na}_2\text{Ti}_3\text{O}_7$ phase.

6.4. Structural Characterization

The characterization results are discussed as follows.

6.4.1. XRD

XRD of the different *uncycled, pristine* TiO₂ based anode samples and the *uncycled* Na₂Ti₃O₇ sample is as shown in figure 41(a). In this stack of XRD data, the pristine TiO₂ is yellow, TiO₂-HT is red, and Na₂Ti₃O₇ is green. The ICDD database (PDF-002-0387, PDF-001-0562 and PDF-014-0085) is used for indexing the peaks and the peaks match well with the tetragonal TiO₂ phase and the Na₂Ti₃O₇ phase. There is no impurity peaks present indicating phase purity. Figure 41(b) shows the pristine TiO₂ and the TiO₂-HT sample together, demonstrating a small drop in peak intensity for the heat treated sample, which is due to a degree of loss of crystallinity due to heat treatment.

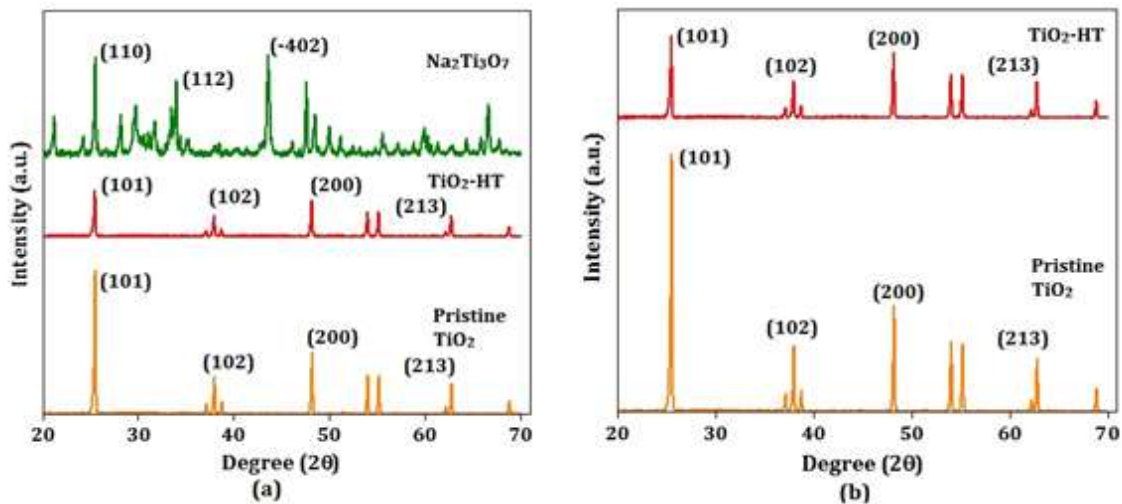


Figure 41. Different XRD data are represented in this figure. (a) XRD spectra of the pristine TiO₂, TiO₂-HT and Na₂Ti₃O₇. (b) XRD spectra stack of pristine and TiO₂-HT.

6.4.2. TEM analysis

TEM results are shown in Figure 42. In figure 42(a), the rod like morphology of the $\text{Na}_2\text{Ti}_3\text{O}_7$ is observed and figure 42(b) exhibits the HRTEM resolved lattice fringes, and it demonstrates the crystallinity of the sample. The SAED pattern of the sample is shown in figure 42(c) and (d). From figure 42(c), d-spacing values of 3.47 Å and 8.92 Å are obtained corresponding to the (110) and (001) planes of $\text{Na}_2\text{Ti}_3\text{O}_7$ (PDF card No. 000-014-0085), respectively. It should be mentioned here that the sample exhibited a high degree of sensitivity to the electron beam tilting to get a reasonable zone axis alignment was difficult. Hence the SAED patterns were taken in a way to reduce damage due to radiation.

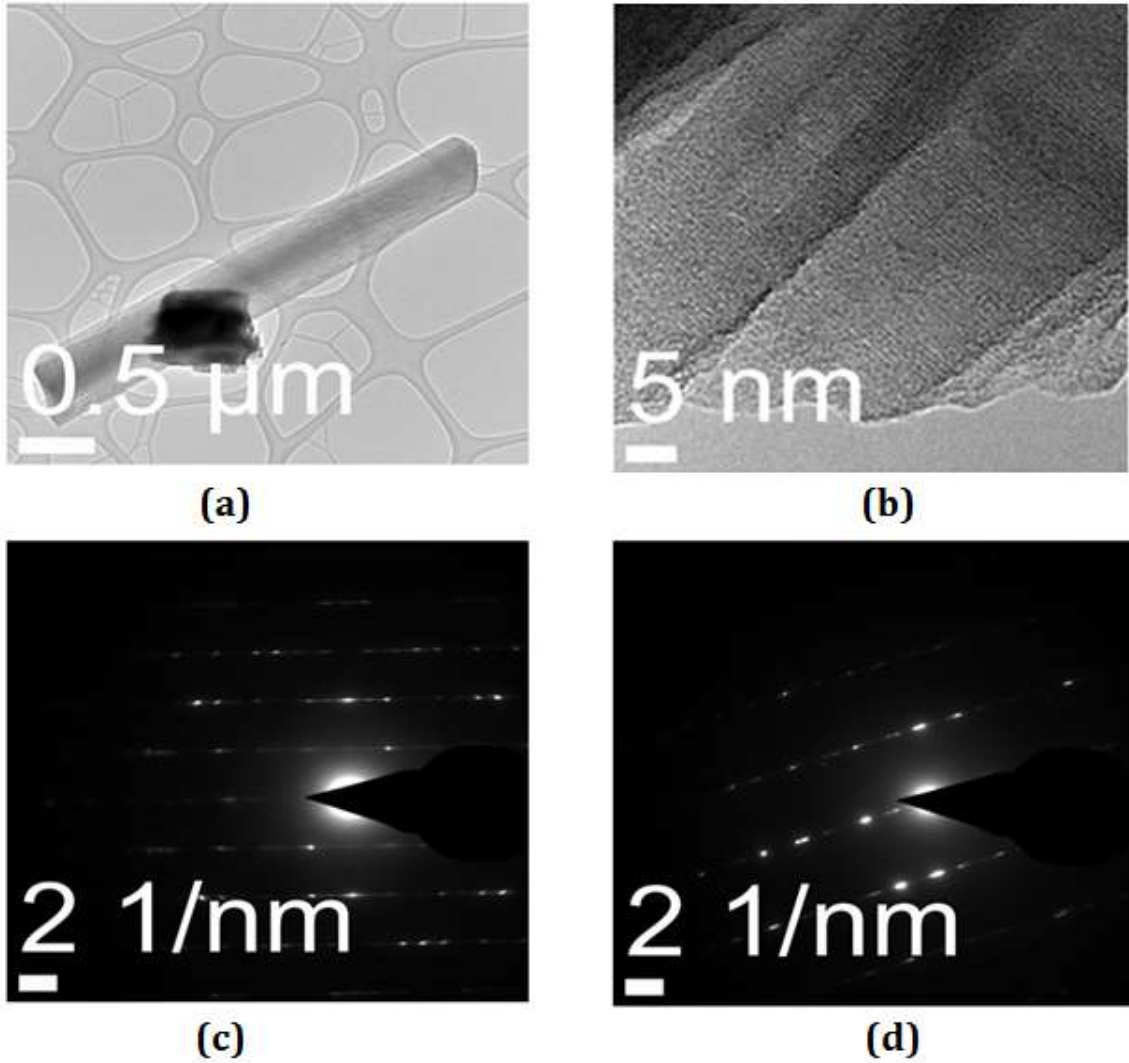


Figure 42. (a) TEM image of the 0.5 μm resolution showing rod like morphology. (b) HRTEM image taken at 5 nm. (c) SAED pattern demonstrating characteristic d-spacing values for the (110) and (001) planes (d) similar SAED pattern exhibiting the d-spacing values for the (013) and (101) planes.

6.4.3. SEM

SEM images for the different TiO_2 morphologies and $\text{Na}_2\text{Ti}_3\text{O}_7$ are provided in the figure below.

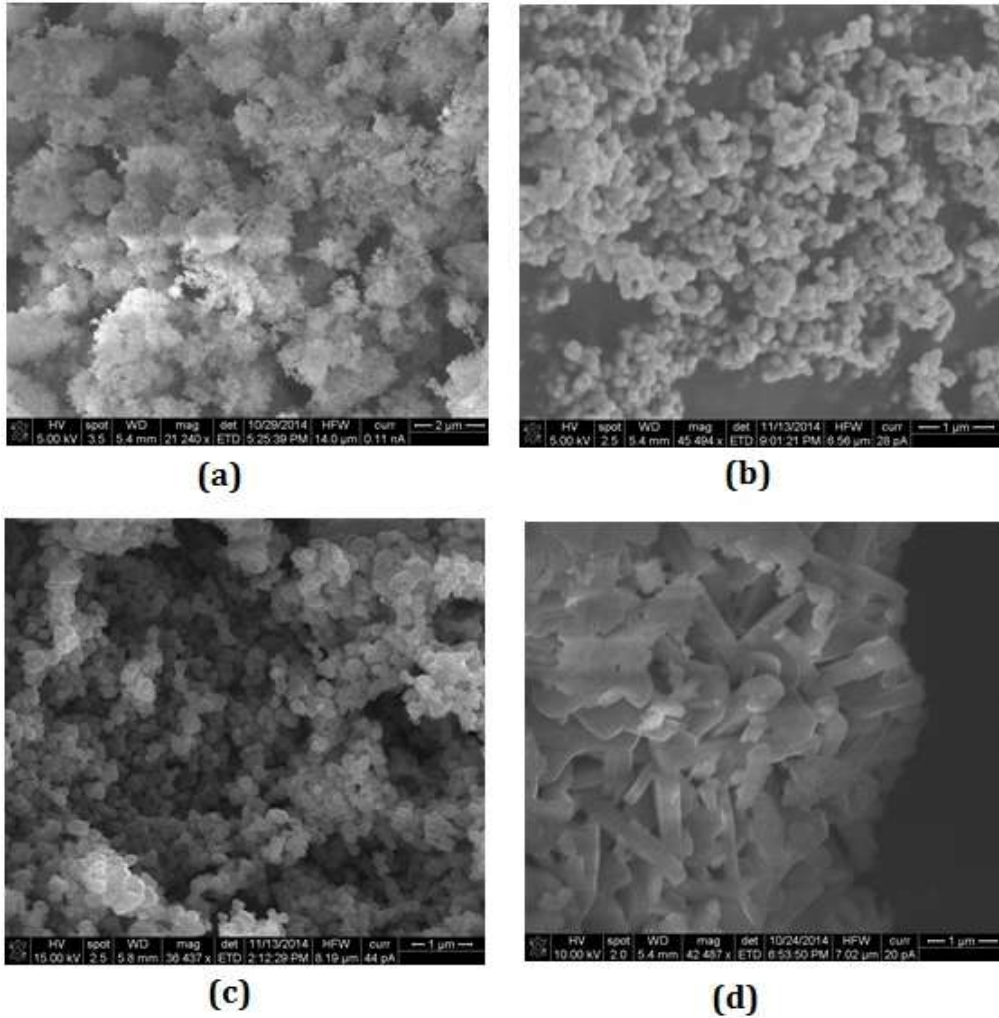


Figure 43. (a) is the images of the amorphous TiO₂ system (b) pristine TiO₂ (c) TiO₂-HT particles (d) Na₂Ti₃O₇.

Amorphous TiO₂ nanoparticles are observed in figure 43(a). A flower like surface morphology is observed. The pristine TiO₂ sample demonstrates a well-rounded spherical microstructure, so too do the TiO₂-HT sample as seen in figure 43(c). Figure 43(d) demonstrates the Na₂Ti₃O₇ articles which exhibit a rod like elongated morphology, also as observed in the TEM. The results conform with published literature¹⁴⁸.

6.4.4. Raman spectra

Figure 44(a) represents the Raman spectra data of the different anode systems.

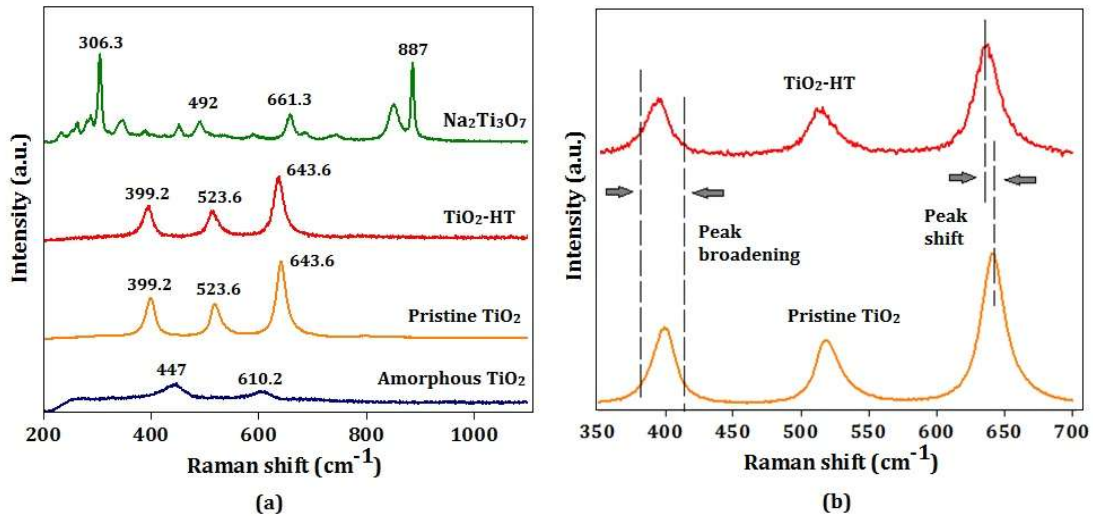


Figure 44. (a) Raman spectra of the different anode systems (b) Raman spectra peaks in greater detail to show peak broadening and shift.

The graph at the bottom of the stack (in blue) represents The amorphous TiO_2 sample exhibits two broad and diffuse peaks at 447.071 cm^{-1} and 610.242 cm^{-1} , which conform to the rutile phase. For the pristine (yellow) and $\text{TiO}_2\text{-HT}$ (red) samples, characteristic peaks are noticed at 401.33 cm^{-1} , 520 cm^{-1} , and 632.63 cm^{-1} and are confirmed by published literature¹⁴⁹. Figure 44(b) represents the Raman spectra of the pristine (and $\text{TiO}_2\text{-HT}$ samples in detail, and a small peak broadening and shift is observed in the HT sample due to the annealing process. The peaks of the $\text{Na}_2\text{Ti}_3\text{O}_7$ phase (in green) also conform well to published data¹⁵⁰. The position of the characteristic peaks indicate the layered titanate structure¹⁵¹.

6.5 Cell assembly

The electrodes were prepared by mixing with binder (in a 2:1 ratio) and then pasting on to current collector at a slightly elevated temperature (120° for 4 hours). For the aqueous measurements, open beaker type cells were used rather than coin cells. The electrolyte was 0.5 M Na₂SO₄. For organic measurements, the counter electrode used was a sodium metal foil and the electrolyte was 0.5 M NaPF₆ dissolved in a 1:1 ratio of EC:DMC. The voltages mentioned are for the full cell.

6.6 Battery performance analysis

The battery performance results can be sub-divided into two sections as follows.

6.6.1 Cell cycling and stability analysis

Figure 45(a) - (d) show the performance of the different anode systems in aqueous electrolyte conditions for the 1st and the 20th cycle.

The Na₂Ti₃O₇ system demonstrates the highest specific capacity of 76.5223 mAh g⁻¹, followed by the TiO₂-HT system (58.5047 mAh g⁻¹), the pristine TiO₂ system (52.2486 mAh g⁻¹) The amorphous TiO₂ system shows poor values of specific capacity (maximum of 28.1855 mAh g⁻¹), due to its inability to host sufficient Na⁺ atoms in the lattice because of the lack of crystallinity in its structure.

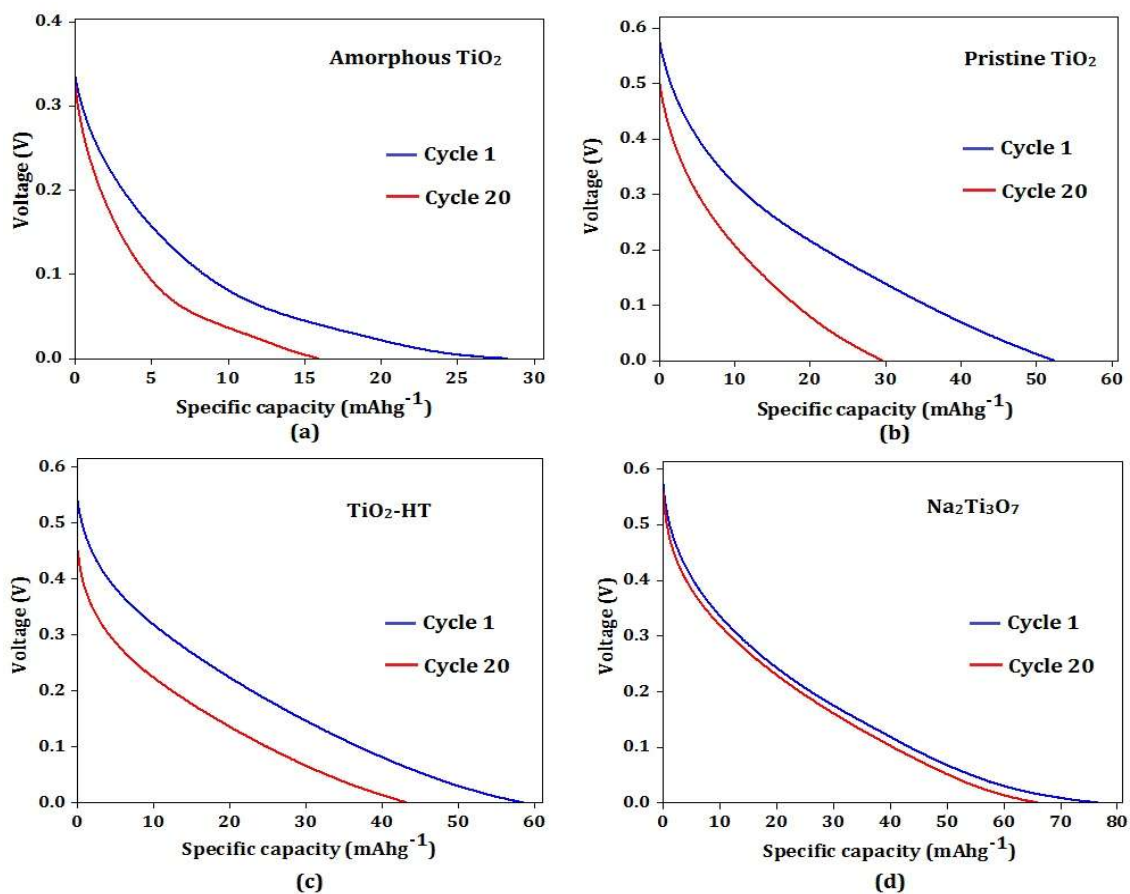


Figure 45. 1st and 20th cycle discharge capacities for (a) amorphous TiO₂ sample (b) Pristine TiO₂ sample (c) TiO₂-HT sample and (d) Na₂Ti₃O₇ sample in aqueous media.

The performance of all these anode systems shows that the Na₂Ti₃O₇ system can retain the capacity better than the other systems during the course of cycling.

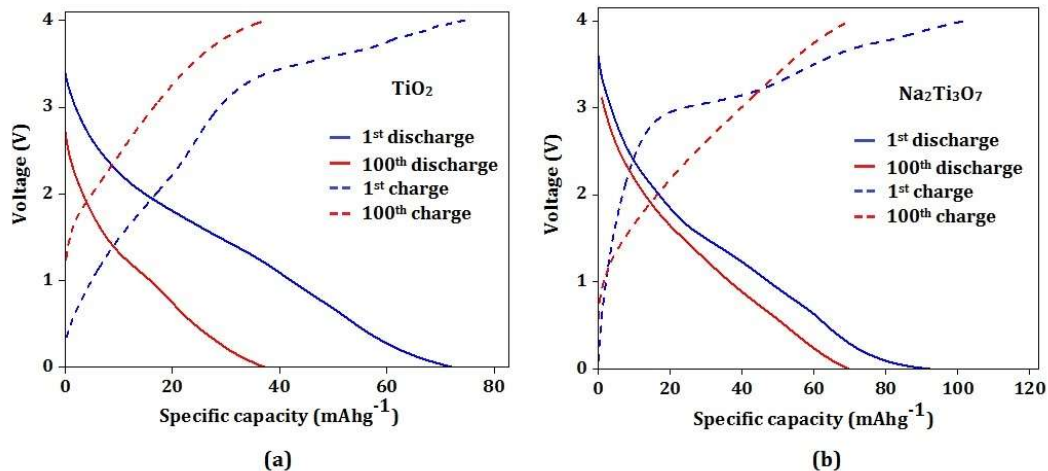


Figure 46. Charge (dashed lines) and discharge (solid lines) curves of the 1st and 100th cycle for (a) TiO₂ sample and (b) Na₂Ti₃O₇ sample in organic media.

Figure 46 (a) and (b) show the performance of the pristine TiO₂ and Na₂Ti₃O₇ anodes in organic environment. Na₂Ti₃O₇, once again provides the maximum specific capacity of 92.1811 mAh g⁻¹. The TiO₂ system provides a maximum first cycle specific capacity of 71.93 mAh g⁻¹ is obtained which drops to 37.16 mAhg⁻¹ after 100 cycles. This corresponds to the fact that the TiO₂ anode undergoes a more rapid degradation than the Na₂Ti₃O₇ system, even when the electrolyte is in the organic environment.

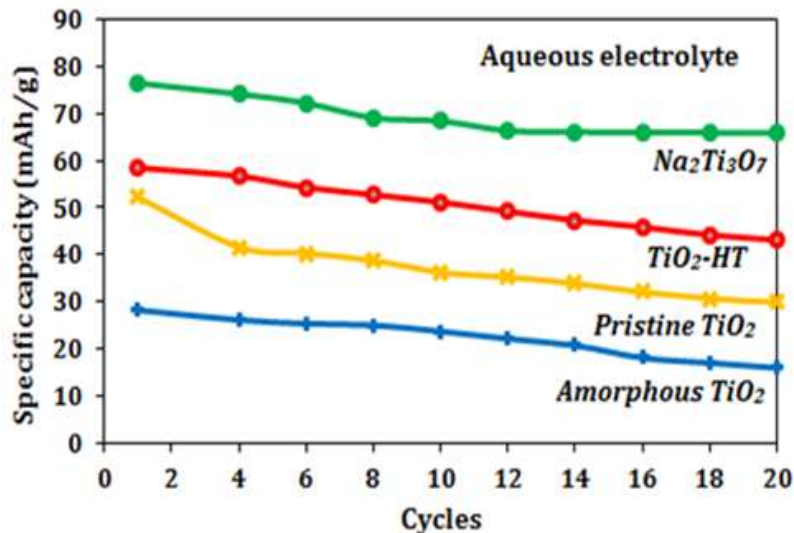


Figure 47. Stability analysis of the various anode systems in aqueous media.

Figure 47 show the stability analysis of the various anode systems. $\text{Na}_2\text{Ti}_3\text{O}_7$ system exhibits better stability (86.2% after 20 cycles) than the other anode systems. Pristine TiO_2 system's specific capacity drops steadily in the initial cycles and then levels off, which is due to initial deformation of TiO_2 lattice to accommodate large Na^+ ion (55 % retention). $\text{TiO}_2\text{-HT}$ does better than pristine TiO_2 in terms of stability (73.75 % capacity retention over 57.16 % after 20 cycles).

6.7 Thermal imaging analysis:

Thermal imaging was performed by an infrared camera to look for any heat generated. The imaging was done while the cell was being run in an open beaker format and the thermal image profiles are shown in figure 48(a) – (d) below.

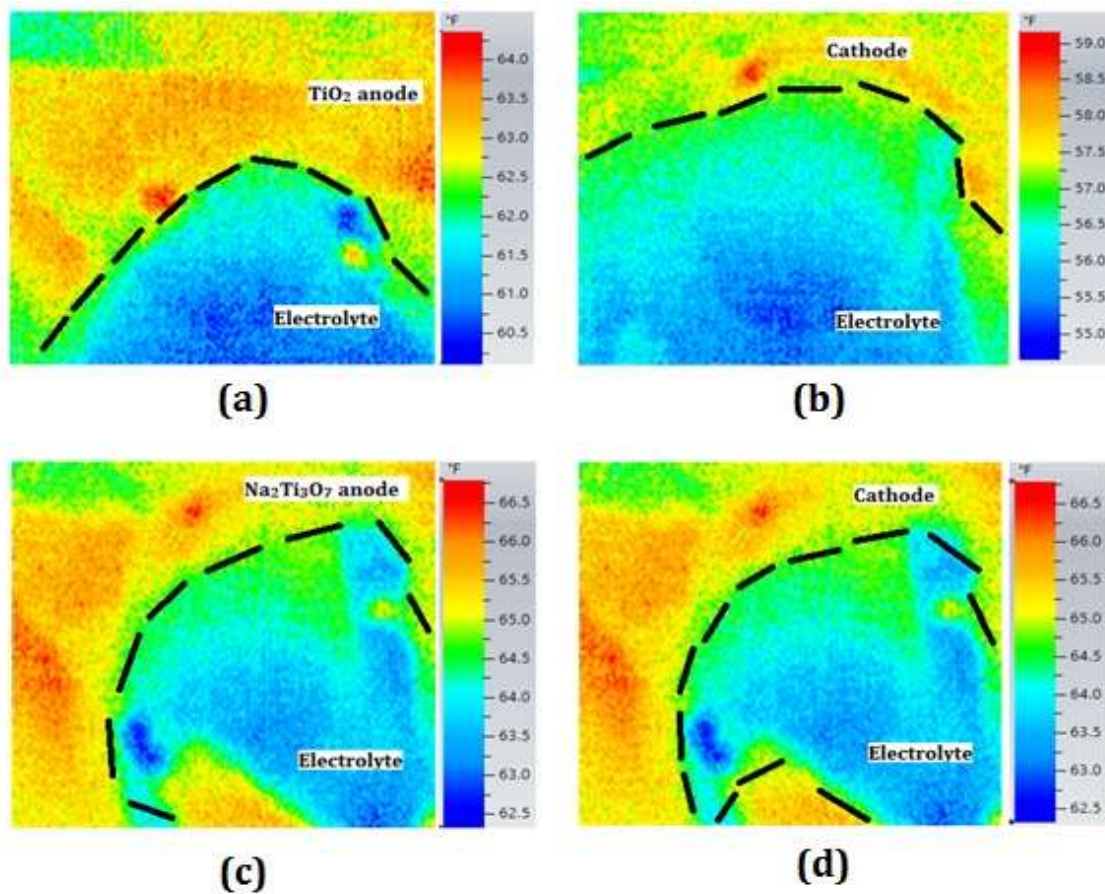


Figure 48. Figures (a) and (b) represent the thermal image profiles for the TiO₂ anodes and P.B cathode during the cell cycling. Similarly (c) and (d) are the thermal image profiles for the Na₂Ti₃O₇ anode and P.B. cathodes during cycling.

The electrode-electrolyte interface has been demarcated by black dashed lines. Figures 48(a) is the thermal image for the TiO₂ sample and 48(c) is for the Na₂Ti₃O₇ sample. Figures 48(b) and 48(d) show the P.B. cathodes. It can be clearly seen that there is a significant difference of temperature on the electrode side. Even though no thermal modeling has been performed, it is understood that the reaction taking place at the electrodes, and the consequent interfacial impedance results in the heat being produced.

Therefore, this heat profile can be an indirect indicator of the degradation occurring in the electrodes.

6.8 Conclusion:

Different types of sodium deficient and sodium rich titania based layered anode structures have been studied with a Na rich Prussian blue cathode system. The $\text{Na}_2\text{Ti}_3\text{O}_7$ anode system performs better than the other in both aqueous and organic media. This can be attributed to its larger enhanced interlayer spacing which help to easily intercalate/deintercalate Na^+ ions. TiO_2 anode systems however tend to degrade quicker due to the greater lattice stress occurring as a consequence of hosting large Na^+ ions. The HT sample performs slightly better than the pristine sample, which may be due to slightly larger interstitial spaces generated. Therefore this brief project demonstrates the superiority of layered structures and how it can be used to effectively enhance the performance of Na-ion batteries, in both aqueous and organic media, as the case may be.

CHAPTER 7

CONCLUSION

The dissertation has been dedicated to the study of TMOs in aqueous Na-ion batteries. A variety of observations are obtained and suitable inferences have been drawn based on those. Three different types of anode materials have been tried: CuO, Fe₂O₃ and TiO₂ with each having their own characteristic properties.

Detailed studies on multiple CuO morphologies indicate that surface area greatly influences the kinetics. Intuitively, a higher surface area as exhibited by the spheres indicates improved reaction kinetics and thereby higher initial capacity. However, the platelet like samples demonstrate marginally better stability. This, therefore, means the “perfect” microstructure necessarily does not mean the one with the one with the highest surface area or maximum stability but lies somewhere in between.

Results of doping in Fe₂O₃ lattice demonstrate that optimum addition of a foreign atom has a very important role to play in determining the electrochemical properties/performance of an anode. Incorporation of the larger Zn²⁺ ion results in the formation of a composite anode system which has a net positive effect, on the other hand the incorporation of a rather smaller but isovalent Al³⁺ ion has a net detrimental effect due to shrinkage of the lattice as well formation of a Al₂O₃ which is basically an impurity phase and plays a role exactly opposite to that of a composite. Therefore the underlying outcome from this research is that the role of doping improves or degrades the

performance of anode depending upon the type of dopant atom used and the amount of doping.

The TiO_2 anode based project re-establishes further the results obtained from the previous two projects, especially the Fe_2O_3 based project. The difference here lies in the fact that the “doping”, or in this case addition of Na^+ ions alters the entire crystal from TiO_2 to $\text{Na}_2\text{Ti}_3\text{O}_7$, thereby forming a different structure altogether. Here too, results indicate $\text{Na}_2\text{Ti}_3\text{O}_7$ performs better, by virtue of its microstructure and larger lattice volume which provides it the ability to intercalate the Na^+ ions better.

Empirically, this dissertation demonstrates the role structural as well as morphological modification can play in determining particular electrochemical parameters. Successful tailoring of each provides optimal performances. The effect of introducing changes and defects in the morphology as well as lattice structure also helps to analyze and prevent structural degradation in some cases e.g. with doping Zn^{2+} in Fe_2O_3 . Various experimental techniques have been utilized to study the electrochemical effects and it is expected that the results will help to improve the understanding of structural and kinetics effects in aqueous Na-ion batteries and facilitate their application.

REFERENCES

- 1 Hoffert, M. I. *et al.* Advanced Technology Paths to Global Climate Stability: Energy for a Greenhouse Planet. *Science* **298**, 981-987 (2002).
- 2 Dresselhaus, M. S. & Thomas, I. L. Alternative energy technologies. *Nature* **414**, 332-337 (2001).
- 3 Swackhamer, G. Cognitive Resources for Understanding Energy. 1-42 (Arizona State University, 2005).
- 4 Hilgevoord, J. The uncertainty principle for energy and time. *American Journal of Physics* **64**, 1451-1456 (1996).
- 5 Mayer, J. R. Bemerkungen über die Kräfte der unbelebten Natur. *Annalen der Chemie und Pharmacie* **42**, 233-240 (1842).
- 6 Radovic, L. R. & Schobert, H. H. in *Energy and fuels in society* (McGraw-Hill, 1992).
- 7 Boyle, G. *Renewable energy: power for a sustainable future*. (Oxford University Press, 1997).
- 8 Nag, P. K. *Engineering Thermodynamics*. (Tata McGraw-Hill, 2005).
- 9 Bowman, D. M., Balch, J. K. & Artaxo, P. Fire in the Earth System. *Science* **324**, 481-484 (2009).
- 10 Heinberg, R. *The end of growth: Adapting to our new economic reality*. (New Society Publishers, 2011).
- 11 Fouquet, R. in *International handbook on the economics of energy* 1-19 (Edward Elgar Publishing, 2011).
- 12 McNeill, J. R. *Something new under the sun: An environmental history of the twentieth-century world.*, (WW Norton and Company, 2000).
- 13 Georgescu-Roegen, N. Feasible recipes versus viable technologies. *Journal of World History* **12**, 21-31 (1984).
- 14 Jevons, W. S. The coal question: An inquiry concerning the progress of the nation, and the probable exhaustion of our coal miners. (1865).
- 15 Morrow, W. R., Gallagher, K. S., Collantes, G. & Lee, H. Analysis of policies to reduce oil consumption and greenhouse gas emissions from the US transportation sector. *Energy Policy* **38**, 1305-1320 (2010).
- 16 Payne, J. E. & Taylor, J. P. Nuclear Energy Consumption and Economic Growth in the U.S.: An Empirical Note. *Energy Sources Part B: Economics, Planning and Policy* **5**, 301-307 (2010).
- 17 Balassa, B. Exports, policy choices and economic growth in developing countries after the 1973 oil shock. *Journal of Development Economics* **18**, 23-35 (1985).
- 18 Apergis, N. & Payne, J. E. Renewable energy consumption and economic growth: Evidence from a panel of OECD countries. *Energy Policy* **38**, 656-660 (2010).
- 19 Malanima, P. *Energy In History*. (Institute of Studies on mediterranean Societies, Naples, Italy, 2014).
- 20 Gillingham, K., Newell, R. G. & Palmer, K. Energy Efficiency Economics and Policy *Annual Review of resource Economics* **1**, 597-619 (2009).

- 21 Timmons, D., Harris, J. M. & Roach, B. The Economics of Renewable Energy. (Tufts University, Boston, Massachusetts, 2014).
- 22 Agency, I. E. Projected Costs of Generating Electricity. (International Energy Agency, Paris, France, 2010).
- 23 Turner, J. A. A Realizable Renewable Energy Future. *Science* **285**, 687-689 (1999).
- 24 Uchaker, E. *Impact of Structure and Defect Modification On Vanadium Oxide Fo Alkali-Ion Battery Electrodes* Doctor of Philosophy thesis, University of Washington, (2015).
- 25 Energy, U. S. D. o. Grid Energy Storage. (U.S. Department of Energy, 2013).
- 26 Hamilton, K. in *Energy Information Administration Energy Conference*.
- 27 Yang, Z. *et al.* Electrochemical Energy Storage for Green Grid. *Chemical Reviews* **111**, 3577-3613 (2011).
- 28 Agency, I. E. World Energy Outlook. (International Energy Agency, Paris, 2010).
- 29 Powell, C. A. & Morreale, B. D. Materials Challenges in Advanced Coal Conversion Technologies. *MRS Bulletin* **33**, 309-315 (2008).
- 30 Arunachalam, V. S. & Fleischer, E. L. The Global Energy Landscape and Materials Innovation. *MRS Bulletin* **33**, 265-275 (2008).
- 31 DOE, E. a. U. EPRI-DOE handbook of energy storage for transmission and distribution applications. (2003).
- 32 Paravasthu, R. *Synthesis And Characterization of Lithium-Ion Cathode Materials In The System $(1-x-y)\text{LiNi}_{1/3}\text{Mn}_{1/3}\text{Co}_{1/3}\text{O}_2.x\text{Li}_2\text{MnO}_3.y\text{LiCoO}_2$* Master of Science thesis, Colorado State University, (2012).
- 33 Bradbury, K. Energy Storage Technology Review. (2010).
- 34 ECOFYS. Energy Storage Opportunities and Challenges. (2014).
- 35 Vechy, S. L. Advanced Electrochemical Energy Storage Technologies For Stationary Power Applications. (EnerSys, Reading, PA).
- 36 Pool, R. Dead and Buried. *Power Engineer* **21**, 16-21 (2007).
- 37 Shukla, A. K. & Kumar, T. P. Electrochemical Energy Storage Devices. *Proceedings of the Indian National Science Academy* **81**, 891-902 (2015).
- 38 Larminie, J. & Dicks, A. *Fuel Cell Systems Explained*. (John Wiley & Sons Ltd., 2003).
- 39 Guo, Y. G., Hu, Y. S., Sigle, W. & Maier, J. Superior Electrode Performance of Nanostructured Mesoporous TiO₂ (Anatase) through Efficient Hierarchical Mixed Conducting Networks. *Advanced Materials* **19**, 2087-2091 (2007).
- 40 Badwal, S. P. S., Giddey, S. S., Munnings, C., Bhatt, A. I. & Hollenkamp, A. F. Emerging electrochemical energy conversion and storage technologies. *Frontiers in Chemistry* **2**, 1-28 (2014).
- 41 Singamsetti, N. & Tosunoglu, S. in *The 8th International Symposium on management, Engineering and Informatics*.
- 42 Patey, T. J. *Oxide Nanoparticles for Electrodes in Lithium-Ion Batteries* PhD thesis, ETH Zurich, (2009).
- 43 Nishi, Y. Lithium ion secondary batteries; past 10 years and the future. *Journal of Power Sources* **100**, 101-106 (2001).
- 44 Skyllas-Kazacos, M., Chakrabarti, M. H., Hajimolana, S. A., Mjalli, F. S. & Saleem, M. Progress in Flow Battery Research and Development. *Journal of the Electrochemical Society* **158**, R55-R79 (2011).
- 45 Yoshino, A. The Birth of the Lithium-Ion Battery. *Angewandte Chemie* **51**, 5798-5800 (2012).
- 46 Bates, A. *et al.* Modeling and simulation of 2D lithium-ion solid state battery. *International Journal of Energy Research* **39**, 1505-1518 (2015).

- 47 Guyomard, D. & Tarascon, J.-M. Rocking-chair or lithium-ion rechargeable lithium batteries. *Advanced Materials* **6**, 408-412 (1994).
- 48 Megahed, S. & Scrosati, B. Lithium-ion rechargeable batteries. *Journal of Power Sources* **51**, 79-104 (1994).
- 49 Hamann, C. H., Hamnett, A. & Vielstich, W. *Electrochemistry*. Vol. Second (Wiley, 2007).
- 50 Firth, D. C. *Elementary Chemical Thermodynamics*. (Oxford University Press, 1969).
- 51 Bagotsky, V. S. *Fundamentals of Electrochemistry*. (Wiley, 2006).
- 52 Burgess, J. *Ions In Solution*. (Horwood Publishing, 1999).
- 53 Koryta, J. *Ions, Electrodes and Membranes*. (John Wiley and Sons, 1982).
- 54 Parsons, R. The relation between the capacity of the electrode double layer and the adsorption of surface-active material. *Transactions of the Faraday Society* **55**, 999-1006 (1959).
- 55 Broussely, M. & Pistoia, G. *Industrial applications of batteries: from cars to aerospace and energy storage*. (Elsevier, 2010).
- 56 Scrosati, B. & Garche, J. Lithium batteries: Status, prospects and future. *Journal of Power Sources* **195**, 2419-2430 (2010).
- 57 Whittingham, M. S. Lithium Batteries and Cathode Materials. *Chemical Reviews* **104**, 4271-4302 (2004).
- 58 Etacheri, V., Marom, R., Elazari, R., Salitra, G. & Aurbach, D. Challenges in the development of advanced Li-ion batteries: a review. *Energy & Environmental Science* **4**, 3243-3262 (2011).
- 59 Tang, Y., Yang, L., Qiu, Z. & Huang, J. template-free synthesis of mesoporous spinel lithium titanate microspheres and their application in high-rate lithium ion batteries. *Journal of Materials Chemistry* **19**, 5890-5894 (2009).
- 60 Delacourt, C. *et al.* Toward Understanding of Electrical Limitations (Electronic, Ionic) in LiPO₄ (M = Fe, Mn) Electrode Materials. *Journal of the Electrochemical Society* **152**, A913-A921 (2005).
- 61 Tarascon, J. M. & Armand, M. Issues and challenges facing rechargeable lithium batteries. *Nature* **414**, 359-367 (2001).
- 62 Winter, M. & Bessenhard, J. O. Electrochemical lithiation of tin and tin-based intermetallics and composites. *Electrochimica Acta* **45**, 31-50 (1999).
- 63 Doyle, C. Lithium and Rare Earth Elements: The Dirty Business of Clean Energy. (California Western School of Law, California, 2015).
- 64 Ellis, B. L. & Nazar, L. F. Sodium and sodium-ion energy storage batteries. *Current Opinion in Solid State and Materials Science* **16**, 168-177 (2012).
- 65 Palomares, V. *et al.* Na-ion batteries, recent advances and present challenges to become low cost energy storage. *Energy and Environmental Science* **5**, 5884-5901 (2012).
- 66 Kim, S.-W., Seo, D.-H., Ma, X., Ceder, G. & Kang, K. Electrode Materials for Rechargeable Sodium-Ion Batteries: Potential Alternatives to Current Lithium-Ion Batteries. *Advanced Energy Materials* **2**, 710-721 (2012).
- 67 Slater, M. D., Kim, D., Lee, E. & Johnson, C. S. Sodium-Ion Batteries. *Advanced Functional Materials* **23**, 947-958 (2013).
- 68 Whittingham, M. S. Chemistry of intercalation compounds: Metal guests in chalcogenide hosts. *Progress in Solid State Chemistry* **12**, 41-99 (1978).
- 69 Yabuuchi, N., Yoshida, H. & Komaba, S. Crystal Structures and Electrode performance of Alpha-NaFeO₂ for Rechargeable Sodium Batteries. *Electrochemistry* **80**, 716-719 (2012).
- 70 Jian, Z. *et al.* Carbon coated Na₃V₂(PO₄)₃ as novel electrode material for sodium ion batteries. *Electrochemistry Communications* **14**, 86-89 (2012).

- 71 Jian, Z. *et al.* Superior Electrochemical Performance and Storage Mechanism of Na₃V₂(PO₄)₃ Cathode for Room-Temperature Sodium-Ion Batteries. *Advanced Energy Materials* **3**, 156-160 (2012).
- 72 Pan, H., Hu, Y.-S. & Chen, L. Room-temperature stationary sodium-ion batteries for large-scale electric energy storage. *Energy and Environmental Science* **6**, 2338-2359 (2013).
- 73 Didier, C. *et al.* Electrochemical Na-Deinsertion from NaVO₂. *Electrochemical and Solid-State Letters* **14**, A75-A78 (2011).
- 74 Sauvage, F., Laffont, L., Tarascon, J. M. & Baudrin, E. Study of the Insertion/Deinsertion mechanism of Sodium into Na_{0.44}MnO₂. *Inorganic chemistry* **46**, 3289-3294 (2007).
- 75 Berthelot, R., Carlier, D. & Delmas, C. Electrochemical investigation of the P2-Na_xCoO₂ phase diagram. *Nature Materials* **10**, 74-80 (2011).
- 76 Nagelberg, A. S. & Worrell, W. L. A thermodynamic study of sodium-intercalated TaS₂ and TiS₂. *Journal of Solid State Chemistry* **29**, 345-354 (1979).
- 77 Morales, J., Santos, J. & Tirado, J. L. Electrochemical studies of lithium and sodium intercalation in MoSe₂. *Solid State Ionics* **83**, 57-64 (1996).
- 78 Buser, H. J., Schwarzenbach, D., Petter, W. & Ludi, A. The Crystal Structure of Prussian Blue: Fe₄[Fe(CN)₆]₃·xH₂O. *Inorganic chemistry* **16**, 2704-2709 (1977).
- 79 Moritomo, Y., Goto, K. & Shibata, T. Glucose-treated of Manganese Hexacyanoferrate for Sodium-ion Secondary Battery. *Energies*, 1-8 (2015).
- 80 Keggin, J. F. & Miles, F. D. Structures and formulae of the prussian Blues and Related Compounds. *Nature* **137**, 577-578 (1936).
- 81 Wessells, C. D., Peddada, S. V., Huggins, R. A. & Cui, Y. Nickel Hexacyanoferrate Nanoparticle Electrodes For Aqueous Sodium and Potassium Ion Batteries. *Nano Letters* **11**, 5421-5425 (2011).
- 82 Jia, Z. & Sun, G. Preparation of prussian blue nanoparticles with single precursor. *Colloids and Surfaces A* **302**, 326-329 (2007).
- 83 Okubo, M., Li, C. H. & Talham, D. R. High rate sodium ion insertion into core-shell nanoparticles of prussian blue analogues. *Chemical Communications* **50**, 1353-1355 (2014).
- 84 Lee, H., Kim, Y.-I., Park, J.-K. & Choi, J. W. Sodium zinc hexacyanoferrate with a well-defined open framework as a positive electrode for sodium ion batteries. *Chemical Communications* **48**, 8416-8418 (2012).
- 85 Wu, X., Cao, Y., Ai, X., Qian, J. & Yang, H. A low-cost and environmentally benign aqueous rechargeable sodium-ion battery based on NaTi₂(PO₄)-Na₂NiFe(CN)₆ intercalation chemistry. *Electrochemistry Communications* **31**, 145-148 (2013).
- 86 Stevens, D. A. & Dahn, J. R. The Mechanism of Lithium and Sodium Insertion in Carbon Materials. *Journal of the Electrochemical Society* **148**, A803-A811 (2001).
- 87 Xiao, L. *et al.* High capacity, reversible alloying reactions in SnSb/C. *Chemical Communications* **48**, 3321-3323 (2012).
- 88 Li, Z., Ravnsbaek, D. B., Xiang, K. & Chiang, Y.-M. Na₃Ti₂(PO₄)₃ as a sodium-bearing anode for rechargeable aqueous sodium-ion batteries. *Electrochemistry Communications* **44**, 12-15 (2014).
- 89 Jiang, Y. *et al.* Transition metal oxides for high performance sodium ion battery anodes. *Nano Energy* **5**, 60-66 (2014).
- 90 Hasa, I., Buchholz, D., Passerini, S. & Hassoun, J. A comparative study of layered transition metal oxide cathodes for application in sodium-ion battery. *ACS Applied Materials and Interfaces* **7**, 5206-5212 (2015).

- 91 Yang, P. *et al.* Low-Cost High-Performance Solid-State Asymmetric Supercapacitors Based on MnO₂ Nanowires and Fe₂O₃ Nanotubes. *Nano Letters* **14**, 731-736 (2014).
- 92 Hariharan, S., Saravanan, K., Ramara, V. & Balaya, P. A rationally designed dual role anode material for lithium-ion and sodium-ion batteries: case study of eco-friendly Fe₃O₄. *Physical Chemistry Chemical Physics* **15**, 2945-2953 (2013).
- 93 Valvo, M., Lindgren, F., Lafont, U., Björefors, F. & Edström, K. Towards more sustainable negative electrodes in Na-ion batteries via nanostructured iron oxide. *Journal of Power Sources* **245**, 967-978 (2014).
- 94 Hariharan, S., Saravanan, K. & Balaya, P. α-MoO₃: A high performance anode material for sodium ion batteries. *Electrochemistry Communications* **31**, 5-9 (2013).
- 95 Deng, C., Zhang, S., Dong, Z. & Shang, Y. 1D nanostructured sodium vanadium oxide as a novel anode material for aqueous sodium ion batteries. *Nano Energy* **4**, 49-55 (2014).
- 96 Wu, X., Wu, W., Wang, K., Chen, W. & He, D. Synthesis and electrochemical performance of flower-like MnCO₂O₄ as an anode material for sodium ion batteries. *Materials Letters* **147**, 85-87 (2015).
- 97 Hammond, C. *The basics of crystallography and diffraction*. (Oxford University Press, 1997).
- 98 Bumbrah, G. S. & Sharma, R. M. Raman spectroscopy - Basic principle, instrumentation and selected applications for the characterization of drugs of abuse. *Egyptian Journal of Forensic Sciences* **6**, 209-215 (2016).
- 99 Nixon, W. C. A Discussion on New Developments in Electron Microscopy with Special Emphasis on their Application in Biology. *Philosophical Transactions of the Royal Society of London. Series B, Biological Sciences* **261**, 45-50 (1971).
- 100 Williams, D. B. & Carter, C. B. *Transmission Electron Microscopy: Diffraction, Imaging and Spectrometry*. (Springer US, 1996).
- 101 Heide, P. v. d. *X-Ray Photoelectron Spectroscopy: An Introduction to Principles and Practices*. (John Wiley and Sons, 2011).
- 102 Fagerlund, G. Determination of the specific surface by the BET method. *Materiaux et Construction* **6**, 239-245 (1973).
- 103 Heinze, J. Cyclic Voltammetry—"Electrochemical Spectroscopy". *New Analytical Methods* (25). *Angewandte Chemie* **23**, 831-847 (1984).
- 104 Retter, U. & Lohse, H. *Electroanalytical Methods*. (Springer, 2005).
- 105 Zhang, W. X. *et al.* Hierarchical self-assembly of microscale cog-like superstructures for enhanced performance in lithium-ion batteries. *Advanced Functional Materials* **21**, 3516-3523 (2011).
- 106 Zheng, S. F. *et al.* Introducing dual functional CNT networks into CuO nanomicrospheres toward superior electrode materials for lithium-ion batteries. *Chemistry of Materials* **20**, 3617-3622 (2008).
- 107 Wang, C. *et al.* Controlled synthesis of micro/nanostructured CuO anodes for lithium-ion batteries. *Nano Energy* **9**, 334-344 (2014).
- 108 Mai, Y. J. *et al.* CuO/graphene composite as anode materials for lithium-ion batteries. *Electrochimica Acta* **56**, 2306-2311 (2011).
- 109 Xu, Y., Jian, G., Zachariah, M. R. & Wang, C. Nano-structured carbon-coated CuO hollow spheres as stable and high rate anodes for lithium-ion batteries. *Journal of Materials Chemistry A* **1**, 15486-15490 (2013).
- 110 Ko, S., Lee, J.-I., Yang, H. S., Park, S. & Jeong, U. Mesoporous CuO Particles Threaded with CNTs for High-Performance Lithium-Ion Battery Anodes. *Advanced Materials* **24**, 4451-4456 (2012).

- 111 Wang, B., Wu, X.-L., Chun-Ying-Shu, Guo, Y.-G. & Wang, C.-R. Synthesis of CuO/graphene nanocomposite as a high-performance anode material for lithium-ion batteries. *Journal of Materials Chemistry* **20**, 10661-10664 (2010).
- 112 Wang, Z., Su, F., Madhavi, S. & Lou, X. W. CuO nanostructures supported on Cu substrate as integrated electrodes for highly reversible lithium storage. *Nanoscale* **3**, 1618-1623 (2011).
- 113 Lu, L. Q. & Wang, Y. Sheet-like and fusiform CuO nanostructures grown on graphene by rapid microwave heating for high Li-ion storage capacities. *Journal of Materials Chemistry* **21**, 17916-17921 (2011).
- 114 Wu, R. *et al.* MOF-templated formation of porous CuO hollow octahedra for lithium-ion battery anode materials. *Journal of Materials Chemistry A* **1**, 11126-11129 (2013).
- 115 Hasa, I., Verrelli, R. & Hassoun, J. Transition metal oxide-carbon composites as conversion anodes for sodium-ion battery. *Electrochimica Acta* **173**, 613-618 (2015).
- 116 Wang, L. *et al.* Porous CuO nanowires as the anode of rechargeable Na-ion batteries. *Nano Research* **7**, 199-208 (2014).
- 117 Yuan, S. *et al.* Engraving Copper Foil to Give Large-Scale Binder-Free Porous CuO Arrays for High-Performance Sodium-Ion Battery Anode. *Advanced Materials* **26**, 2273-2279 (2014).
- 118 Lu, Y., Zhang, N., Zhao, Q., Liang, J. & Chen, J. Micro-nanostructured CuO/C spheres as high-performance anode materials for Na-ion batteries. *Nanoscale* **7**, 2770-2776 (2015).
- 119 Qin, Y. *et al.* Hierarchically Porous CuO Hollow Spheres Fabricated via a One-Pot Template-Free Method for High-Performance Gas Sensors. *The Journal of Physical Chemistry C* **116**, 11994-12000 (2012).
- 120 You, Y., Wu, X. L., Yin, Y. X. & Guo, Y. G. High-quality Prussian blue crystals as superior cathode materials for room-temperature sodium-ion batteries. *Energy and Environmental Science* **7**, 1643-1647 (2014).
- 121 Hsu, P. H. & Wang, M. K. Crystallization of Goethite and Hematite at 70°C. *Soil Science Society of America* **44**, 143-149 (1979).
- 122 Cannas, C., Gatteschi, D., Musinu, A., Piccaluga, G. & Sangregorio, C. Structural and magnetic Properties of Fe₂O₃ Nanoparticles Dispersed over a Silica Matrix. *The Journal of Physical Chemistry B* **102**, 7721-7726 (1998).
- 123 Xu, X., Cao, R., Jeong, S. & Cho, J. Spindle-like Mesoporous α -Fe₂O₃ Anode Material Prepared from MOF Template for High-Rate Lithium Batteries. *Nano Letters* **12**, 4988-4991 (2012).
- 124 Liu, X. *et al.* Fe₂O₃-reduced graphene oxide composites synthesized via microwave-assisted method for sodium ion batteries. *Electrochimica Acta* **166**, 12-16 (2015).
- 125 Sun, B. *et al.* Synthesis of Mesoporous α -Fe₂O₃ Nanostructures for Highly Sensitive Gas Sensors and High Capacity Anode Materials in Lithium Ion Batteries. *The Journal of Physical Chemistry C* **114**, 18753-18761 (2010).
- 126 Larcher, D. *et al.* Combined XRD, EXAFS, and Mossbauer Studies of the Reduction by Lithium of α Fe₂O₃ with Various Particle Sizes. *Journal of the Electrochemical Society* **150**, A1643-A1650 (2003).
- 127 Lin, Y.-M., Abel, P. R., Heller, A. & Mullins, C. B. α -Fe₂O₃ Nanorods as Anode Material for Lithium Ion Batteries. *The Journal of Physical Chemistry Letters* **2**, 2885-2891 (2011).
- 128 Jeong, J.-M. *et al.* Hierarchical Hollow Spheres of Fe₂O₃@Polyaniline for Lithium Ion Battery Anodes. *Advanced Materials* **25**, 6250-6255 (2013).

- 129 Cho, J. S., Hong, Y. J. & Kang, Y. C. Design and Synthesis of Bubble-Nanorod-Structured Fe₂O₃-Carbon Nanofibers as Advanced Anode Material for Li-ion Batteries. *ACS Nano* **9**, 4026-4035 (2015).
- 130 Wu, H., Xu, M., Wang, Y. & Zheng, G. Branched Co₃O₄/Fe₂O₃ nanowires as high capacity lithium-ion battery anodes. *Nano Research* **6**, 167-173 (2013).
- 131 Jian, Z. *et al.* Fe₂O₃ nanocrystals anchored onto graphene nanosheets as the anode material for low-cost sodium-ion batteries. *Chem Comm* **50**, 1215-1217 (2014).
- 132 Huo, G., Lu, X., Huang, Y., Li, W. & Liang, G. Electrochemical Performance of α -Fe₂O₃ Particles as Anode Material for Aqueous Rechargeable Batteries. *Journal of the Electrochemical Society* **161**, A1144-A1148 (2014).
- 133 Zhang, H. *et al.* Solvothermally induced α -Fe₂O₃/graphene nanocomposites with ultrahigh capacitance and excellent rate capability for supercapacitors. *Journal of Materials Chemistry A* **3**, 22005-22011 (2015).
- 134 Wu, M. *et al.* Facile Synthesis of Fe₂O₃ Nanobelts/CNTs Composites as High-Performance Anode for Lithium-ion Battery. *Electrochimica Acta* **132**, 533-537 (2014).
- 135 Nikolic, M. V. *et al.* Study of Dielectric Behavior and Electrical Properties of Hematite α -Fe₂O₃ Doped with Zn. *Science of Sintering* **44** (2012).
- 136 Kleiman-Shwarsstein, A. *et al.* Electrodeposited Aluminum-Doped α -Fe₂O₃ Photoelectrodes: Experiment and Theory. *Chemistry of Materials* **22**, 510-517 (2010).
- 137 Schwertmann, U., Friedl, J., Stanjek, H. & Schulze, D. G. The Effect of Al on Fe Oxides XIX. Formation of Al-Substituted Hematite From Ferrihydrite at 25 C and pH 4 to 7. *Clays and Clay Minerals* **48**, 159-172 (2000).
- 138 Xing, Z., Ju, Z., Yang, J., Xu, H. & Qian, Y. One-step Hydrothermal Synthesis of ZnFe₂O₄ Nano-Octahedrons as a High Capacity Anode Material for Li-ion Batteries. *Nano Res.* **5**, 477-485 (2012).
- 139 Fu, Q., Wagner, T. & Ruhle, M. Hydroxylated α -Al₂O₃ (0001) surfaces and metal/ α -Al₂O₃ (0001) interfaces. *Surface Science* **600**, 4870-4877 (2006).
- 140 Zoppi, A., Lofrumento, C., Castellucci, E. M. & Sciau, P. Al-for-Fe substitution in hematite: The effect of low Al concentrations in the Raman spectrum of Fe₂O₃. *Journal of Raman Spectroscopy* **39**, 40-46 (2008).
- 141 Huda, M. N., Walsh, A., Stucky, G. & Hu, Y.-S. Electrodeposited Aluminum-Doped α -Fe₂O₃: Photoelectrodes: Experiment and Theory. *Chemistry of Materials* **22**, 510-517 (2010).
- 142 Li, N. *et al.* Battery Performance and Photocatalytic Activity of Mesoporous Anatase TiO₂ Nanospheres/Graphene Composites by Template-Free Self-Assembly *Advanced Functional Materials* **21**, 1717-1722 (2011).
- 143 Cao, F.-F., Wu, X.-L., Xin, S., Guo, Y.-G. & Wan, L.-J. Facile Synthesis of Mesoporous TiO₂-C Nanosphere as an Improved Anode Material for Superior High Rate 1.5 V Rechargeable Li Ion Batteries Containing LiFePO₄-C Cathode. *Journal of Physical Chemistry C* **114**, 10308-10313 (2010).
- 144 Oh, S.-M. *et al.* High Electrochemical Performances of Microsphere C-TiO₂ Anode for Sodium-Ion Battery. *Applied Materials and Interfaces* **6**, 11295-11301 (2014).
- 145 Usui, H., Yoshioka, S., Wasada, K., Shimizu, M. & Sakaguchi, H. Nb-Doped Rutile TiO₂: a Potential Anode Material for Na-Ion Battery. *Applied Materials and Interfaces* **6**, 6567-6573 (2015).
- 146 Senguttuvan, P., Rousse, G., Seznec, V., Tarascon, J.-M. & Palacín, M. R. Na₂Ti₃O₇: Lowest Voltage Ever Reported Oxide Insertion Electrode for Sodium Ion Batteries. *Chemistry of Materials* **23**, 4109-4111 (2011).

- 147 Kim, K.-T. *et al.* Anatase Titania Nanorods as an Intercalation Anode Material for Rechargeable Sodium Batteries. *Nano Letters* **14**, 416-422 (2014).
- 148 Rudola, A., Saravanan, K., Mason, C. W. & Balaya, P. Na₂Ti₃O₇: an intercalation based anode for sodium-ion battery applications. *Journal of Materials Chemistry A* **1**, 2653-2662 (2013).
- 149 Ohsaka, T., Izumi, F. & Fujiki, Y. Raman spectrum of anatase, TiO₂. *Journal of Raman Spectroscopy* **7**, 321-324 (1978).
- 150 Liu, H. *et al.* A Raman spectroscopic and TEM study on the structural evolution of Na₂Ti₃O₇ during the transition to Na₂Ti₆O₁₃. *Journal of Raman Spectroscopy* **41**, 1331-1337 (2010).
- 151 Liu, H. *et al.* A Raman spectroscopic and TEM study on the structural evolution of Na₂Ti₃O₇ during the transition to Na₂Ti₆O₁₃. *Journal of Raman Spectroscopy* **41**, 1331-1337 (2010).

CURRICULUM VITAE

NAME: Santanu Mukherjee

ADDRESS: 1704 S 2nd Street
Apartment 3
Louisville, KY 40208

DOB: February 8, 1984

EDUCATION

& TRAINING: B.E., Mechanical Engineering
Bangalore Institute of Technology, India
2002 – ‘06

M.S., Mechanical and Materials Engineering
University of Nebraska, Lincoln
2010 – ‘12

PhD, Mechanical Engineering
University of Louisville
2012 – ‘17

AWARDS: Departmental Fellowship at University of Louisville
2012 – ‘14

First position at ASME Spring 2015 meeting, Louisville chapter

PUBLICATIONS: S. Mukherjee, N. D. Schuppert, A. Bates, J. Jasinski, J. E. Hong, M. J. Choi and S. Park, “*Novel solvoplasma based tin oxide based nanowires as anode materials for sodium ion batteries*”, Journal of Power Sources, Volume 347 (2017), pp. 201 – 209.

S. Mukherjee, J. Kim, B. Son, N. D. Schuppert, A. Bates, O. Kwon, M. J. Choi, H. Y. Chung and Sam Park, “*A review of lithium and non-lithium based solid state batteries*”, Journal of Power Sources, Volume 282 (2015), pp. 299-322.

S. Mukherjee, A. Bates, N. D. Schuppert, B. Son, J. Kim, J. S. Choi, M. J. Choi, D. H. Lee, O. Kwon, J. Jasinski and Sam Park, “*A study of a novel Na ion battery and its anodic degradation using sodium doped Prussian blue cathode coupled with sodium deficient and rich transition metal oxide anode*”, *Journal of Power Sources*, Volume 286 (2015), pp. 276 – 289.

S. Mukherjee, A. Bates, S.C. Lee, D.H Lee and S. Park, “*A review of application of carbon nanotubes in PEM fuel cells,*” *International Journal of Green Energy*, Volume 12 (2015), pp. 787-809.

S. Mukherjee, N. D. Schuppert, A. Bates, S. C. Lee and S. Park, “*Mesoporous microspheres of Al and Ni doped lithium manganese oxide (LMO) based spinels and their performance as cathodes in secondary lithium ion batteries*”, accepted in *International Journal of Green Energy*.

PRESENTATIONS:

S. Mukherjee, N. D. Schuppert, A. Bates, J. Jasinski, J. E. Hong, M. J. Choi and S. Park, “*Novel SnO₂ Nanowires as Sodium Ion Battery Anodes*”, *ECS Meeting Abstracts* (2016), pp. 65.

S. Mukherjee, A. Bates, N. D. Schuppert, B. Son, J. Kim, J. S. Choi, M. J. Choi, D. H. Lee, O. Kwon, J. Jasinski and S. Park, “*A Study of a Sodium Doped Prussian Blue Cathode Coupled with Sodium Rich and Deficient Transition Metal Oxide Anode*”, *ECS Meeting Abstracts* (2015), pp. 23.